

Spring 5-2021

## Thruster Communication for Subsurface Environments; Turning Waste Noise into Useful Data

Stephen Cronin  
*Embry-Riddle Aeronautical University*

Follow this and additional works at: <https://commons.erau.edu/edt>



Part of the [Data Science Commons](#), and the [Electrical and Computer Engineering Commons](#)

---

### Scholarly Commons Citation

Cronin, Stephen, "Thruster Communication for Subsurface Environments; Turning Waste Noise into Useful Data" (2021). *Doctoral Dissertations and Master's Theses*. 573.  
<https://commons.erau.edu/edt/573>

This Dissertation - Open Access is brought to you for free and open access by Scholarly Commons. It has been accepted for inclusion in Doctoral Dissertations and Master's Theses by an authorized administrator of Scholarly Commons. For more information, please contact [commons@erau.edu](mailto:commons@erau.edu).

**THRUSTER COMMUNICATION FOR SUBSURFACE  
ENVIRONMENTS; TURNING WASTE NOISE INTO USEFUL  
DATA**

by

Stephen Cronin

A dissertation submitted to the Faculty of Embry-Riddle Aeronautical University  
in partial fulfillment of the requirements for the degree of  
Doctor of Philosophy in Electrical Engineering and Computer Science

Embry-Riddle Aeronautical University

Daytona Beach, Florida

May 2021


Thruster Communication for Subsurface Environments; Turning Waste  
Noise into Useful Data


by Stephen Cronin


This dissertation was prepared under the direction of the candidate's Dissertation Committee Chair, Dr. Brian Butka, and has been approved by the members of the dissertation committee. It was submitted to the College of Engineering and accepted in partial fulfillment of the requirements for the Degree of Doctor of Philosophy in Electrical Engineering and Computer Science.


  
\_\_\_\_\_  
Brian Butka, Ph.D.  
Committee Chair

  
\_\_\_\_\_  
Timothy Wilson, Sc.D.  
Committee Member


  
\_\_\_\_\_  
Eduardo Rojas, Ph.D.  
Committee Member

  
\_\_\_\_\_  
Radu Babiceanu, Ph.D.  
Committee Member


  
\_\_\_\_\_  
Patrick Currier, Ph.D.  
Committee Member

  
\_\_\_\_\_  
Timothy A. Wilson, Sc.D.  
Chair, Electrical Engineering and Computer Science

04/26/21  
Date

  
\_\_\_\_\_  
Maj Mirmirani, Ph.D.  
Dean, College of Engineering

04/27/2021  
Date

  
\_\_\_\_\_  
Lon Moller, J.D.  
Senior Vice President for Academic Affairs and Provost

04/27/2021  
Date

## Acknowledgments

Finishing an effort such as this is a task that no one manages to complete on their own. It is the result of years of work and education to complete this dissertation. To all who helped me academically, professionally, and personally you have my sincerest thanks as the success of this project is as much in your hands as it is mine. To the academic community around this subject matter, thank you for listening to this work with the same openness you have to any other established individual in the field. Science and engineering can only progress by supporting and enabling those trying new ideas, and I will use all that I have learned from those who enabled this success to provide what I can moving forward.

A special thanks to the office of naval research for funding this work. This work was funded under Office of Naval Research grant N000141712492.

## Abstract

Acoustic communication serves as one of the primary means of wirelessly communicating underwater. Whereas much of the developments in the field of wireless communication have focused on radio frequency technology, water highly absorbs radio waves rendering the link not feasible for most all subsurface operations. While acoustic links have enabled new capabilities for systems operating in this challenging environment, it has yet to reach the commodity availability of radio systems, meaning that an entire class of small, low-cost systems have been unable to make use of these links. The systems in question are primarily autonomous underwater vehicles (AUVs), as they typically operate untethered as compared to remotely operated vehicles (ROVs). To address this gap in capability, a prototype system was constructed leveraging the ambient noise produced by brushless electric thrusters to transmit data.

This research aims to build on this work and answer some key questions about the technology. The primary research question is how the operation of a thruster as a propulsor impacts the transmission of data. A characterization of the system will be presented, isolating the behavior of the thruster. From this, it will be shown that a thruster behaves in a manner nearly identically to a purpose-built transducer solution. From this finding, an analysis into the optimization of the link is presented, analyzing protocol improvements, inter symbol interference, and approaches to leveraging signal harmonics of the data link to increase bandwidth. From this work, a transmitter implementation was demonstrated utilizing frequency shift keying to send data at a rate of 2000 bits per second. Beyond the specifics of this work, this transmission system was demonstrated on a low-cost, open-source motor controller, enabling a system to easily integrate or enable this capability. This demonstrates that most any system can leverage this technology to add additional operational capability.

## Table of Contents

Acknowledgments.....	3
Abstract.....	4
Table of Contents.....	5
Table of Figures.....	7
Table of Equations.....	9
Table of Tables.....	10
Chapter 1: Introduction.....	11
Motivations.....	11
Chapter Outline.....	12
Brushless Motor Overview.....	13
Modulation Analysis.....	18
Proposed Area of Work.....	20
Chapter 2: Literature Review.....	21
History.....	21
Acoustic Modem.....	21
Communication Reliability.....	21
Current Modem Technology.....	24
Current Modem Research.....	25
Modem Testing.....	27
Signal Propagation Effects.....	29
Attenuation and Scattering.....	29
Range Based Power Falloff.....	30
Multipath.....	32
Doppler.....	34
External Noise Sources.....	35
Fourier Transformation.....	37
Chapter 3: Communication System.....	38
ESC Hardware.....	38
Data Transmission.....	39
ESC Firmware.....	39
Thruster Hardware.....	42
Transmission Protocol.....	43
Receiver Hardware.....	44
Decoding.....	49
Chapter 4: System Characterization.....	54
Hardware Characterization.....	54
Receiver Characterization.....	54

Thruster Response .....	58
Frequency Domain Analysis .....	60
Thruster Characterization .....	65
Full System Response.....	67
Theoretical Transmission Rates .....	68
Chapter 5: Simulation .....	73
Image Method Simulation .....	73
Shallow Channel Model .....	74
Chapter 6: Experimental Testing.....	83
Test Site.....	83
Testing Utilities .....	84
Test Methodology .....	85
Motor Spin .....	86
Image Transmission .....	88
Raw Image Transmission .....	88
Harmonic Image Transmission.....	89
Video Transmission .....	90
Chapter 7: Optimization.....	92
Optimal Transmission Rate .....	92
Inter-Symbol Interference Analysis .....	98
Harmonic Optimizations .....	102
Harmonic Combination.....	103
Harmonic Transmission .....	104
Chapter 8: Conclusions .....	106
Research Outcomes .....	106
Future Work.....	107
References .....	109
Appendix .....	112
Experimental Testing Results.....	112

## Table of Figures

Figure 1: Brushless electric motor components (MotionControlGuide, 2021). .....	13
Figure 2: A three-phase BLDC motor and motor controller. The half-bridge inverter circuits and currents for each phase are color coded (Gamazo-Real, Vázquez-Sánchez, & Gómez-Gil, 2010).....	14
Figure 3: The motor voltages for a typical three-phase BLDC motor. Note the PWM pulses in each phase. (Gamazo-Real, Vázquez-Sánchez, & Gómez-Gil, 2010) .....	14
Figure 4: The measured acoustic noise versus frequency of a thruster driven by an Afro ESC. ....	16
Figure 5: The noise spectrum of a 6kW motor being driven by a 6kHz PWM frequency (Binojkumar, Saritha, & Narayann, 2015).....	16
Figure 6: Field oriented control algorithm diagram (Holtz, 2002).....	17
Figure 7: Modulation schemes visualized (Knowledge Amplifier, 2021).....	18
Figure 8: LFM Chirp .....	19
Figure 9: FSK modulation BER (Almashhadanai, 2017).....	22
Figure 10: Average PSNR under varying channel bit error rates (Naderi, Rabiee, Khansari, & Salehi, 2012). .....	23
Figure 11: Full-duplex acoustic modem circuit diagram for interference cancellation (Shen, Henson, & Mitchell, 2019). .....	26
Figure 12: Shallow channel test case (Galvin & Coates, 1995). .....	28
Figure 13: Attenuation throughout the frequency band (Stojanovic & Preisig, 2009).....	30
Figure 14: R squared power falloff (HyperPhysics, 2021).....	31
Figure 15: Multipath visualization (Grandmetric, 2021).....	32
Figure 16: Multipath intensity profile, time variation of the amplitude and the corresponding intensities of arrivals a,b,c,d (Stojanovic & Preisig, 2009).....	33
Figure 17: Seatrac USBL testing – concrete pool with a length of 50m (Neasham & Sharpouse, 2015). ..	34
Figure 18: Acoustic spectrum of ambient sources in a waterway (Basett, Thomson, & Polagye, 2010). ..	36
Figure 19: VESC 4 hardware (Flipsky, 2021).....	39
Figure 20: Communication System Architecture Overview .....	40
Figure 21: Code segment, setting PWM frequency .....	41
Figure 22: Frequency switching routine .....	41
Figure 23: Data buffer logic for data transmission .....	42
Figure 24: BlueRobotics T200 Thruster (T200 Thruster, 2021).....	43
Figure 25: Teledyne TC-4013 hydrophone (Teledyne Marine, 2021).....	44
Figure 26: SPARTON PHOD-1 hydrophone (SPARTON, 2021).....	45
Figure 27: Signal clipping .....	46
Figure 28: Signal clipping response analysis at half amplitude.....	46
Figure 29: Clipping percentage vs. peak frequency spike amplitude .....	47
Figure 30: Analog filter circuit.....	47
Figure 31: NI-9222 DAQ in an ethernet chassis (National Instruments, 2021).....	48
Figure 32: Single hydrophone received data - hardware filter applied .....	50
Figure 33: Response after decoder filter application .....	51
Figure 34: 5-Value representation of strongest symbol response .....	52
Figure 35: Decoder Correlator Output.....	52
Figure 36: Teledyne TC1026 frequency response (Teledyne Marine, 2021). .....	55



Figure 37: Teledyne TC4013 directivity response (left) and frequency response (right) (Teledyne Marine, 2021).	56
Figure 38: Hardware system characterization test setup	57
Figure 39: Hardware filter response throughout frequency spectrum	58
Figure 40: 1m range voltage test, Sparton PHOD-1	59
Figure 41: 1m range test, Teledyne TC-4013	59
Figure 42: Null symbol frequency response	61
Figure 43: Symbol response with transmission frequency applied	61
Figure 44: Symbol response of transmitted data bit	62
Figure 45: Frequency response of a complete message transmission	63
Figure 46: Frequency response with frequency component gaps aligned	63
Figure 47: Real-world band response	64
Figure 48: Initial frequency response estimation	66
Figure 49: Frequency response of viable frequency range	66
Figure 50: Full system identification - LFSR transmission	67
Figure 51: Comparison of trend behavior - full system and filter system	68
Figure 52: Maximum carrier rate as a function of filter spreading	70
Figure 53: Data rate at various bits per symbol – 1 bit per symbol and 3 bits per symbol occupy the same space	72
Figure 54: Image expansion of source (o) and receiver (x) (Allen & Berkley, 1979)	74
Figure 55: Shallow channel model transmission paths	75
Figure 56: Frequency band of the transmitted data – full transmission, not subset visualized	76
Figure 57: Transmitted data - transmission side	77
Figure 58: Transmitted Signal Symbol Representation	77
Figure 59: Transmitted data spectrogram	78
Figure 60: Phase of a signal with multipath present	79
Figure 61: Model received signal	80
Figure 62: Channel attenuation at 1m	81
Figure 63: Attenuation as a function as frequency (Stojanovic & Preisig, 2009).	82
Figure 64: Simulated Path Loss	82
Figure 65: Pool test environment overhead (Google, 2021).	83
Figure 66: VESC Interface tool	84
Figure 67: 16-Bit LFSR Visualization	85
Figure 68: Duty Cycle vs. Bit Error Rate	87
Figure 69: Raw frame transmission, original (left), received (right)	88
Figure 70: Raw image received frame difference	89
Figure 71: PNG compressed image transmitted on the third harmonic	90
Figure 72: Video transmission, original (left), received (right)	90
Figure 73: Symbol period visual	92
Figure 74: Symbol power response in frequency domain	93
Figure 75: Symbol allocation within a band	95
Figure 76: Number of symbols vs. baud rate	96
Figure 77: Symbol rate comparison between two protocols	98
Figure 78: Inter Symbol Interference visualization	99

Figure 79: SNR at various symbol numbers .....	101
Figure 80: BER as a function of number of symbols .....	102
Figure 81: Spectrum response of harmonics (The Pulsar, 2015).....	103
Figure 82: First Harmonic (Left), Third Harmonic (Right).....	105

## Table of Equations

Equation 1: Stokes law of sound attenuation.....	29
Equation 2: Amplitude reduction from Stoke's law.....	29
Equation 3: Range squared power falloff .....	31
Equation 4: Link budget equation.....	31
Equation 5: Doppler Shift.....	35
Equation 6: Mackenzie calculation for speed of sound in sea water .....	35
Equation 7: Fourier transform .....	37
Equation 8: Fourier transform of the pulse train.....	60
Equation 9: Maximum overlap of control loops .....	69
Equation 10: Maximum carrier rate relationship .....	69
Equation 11: Maximum carrier rate in terms of frequency update rate and filter spreading .....	69
Equation 12: Maximum carrier rate in quadratic form.....	69
Equation 13: Maximum carrier rate solution.....	70
Equation 14: Pressure wave a single frequency point.....	73
Equation 15: Overall path loss (Stojanovic & Preisig, 2009).....	80
Equation 16: LFSR Polynomial.....	85
Equation 17: BER equation .....	86
Equation 18: Symbol rate and symbol period relationship .....	92
Equation 19: Main lobe power allocation.....	93
Equation 20: Full symbol power allocation.....	94
Equation 21: Proportion of power in main lobe .....	94
Equation 22: Symbol bandwidth allocation .....	94
Equation 23: Symbol bandwidth for the experimental link.....	94
Equation 24: Baud rate computation.....	95
Equation 25: Protocol impact on symbols .....	95
Equation 26: Symbol rate relationship to bandwidth.....	96
Equation 27: Generalized baud rate for the protocol.....	96
Equation 28: Shannon-Hartley Theorem .....	99
Equation 29: Adjacent symbol power contribution.....	100
Equation 30: Third and fourth side lobe power contributions .....	100
Equation 31: Power of other symbol side lobes .....	100
Equation 32: Inter-symbol interference signal to noise ratio .....	100
Equation 33: BER for M-FSK communication (Proakis & Salehi, 2007). .....	101

## Table of Tables

Table 1: Comparison of commercial and research modems (Sendra, Lloret, Jimenez, & Parra, 2016). ....	25
Table 2: BlueRobotics T200 Specifications (T200 Thruster, 2021).....	43
Table 3: DAQ measurement data structure.....	49
Table 4: Maximum carrier rate parameters.....	69
Table 5: Baud rate at various symbol numbers .....	97
Table 6: 16-bit LFSR Testing Results.....	112

## Chapter 1: Introduction

The established technologies for communication underwater revolve around the use of discrete acoustic modems. These solutions are typically based around the need for data links over the ranges of hundreds or thousands of meters of open ocean using purpose-built transducers to transmit data. Although great at what they do, costs for these systems may exceed tens of thousands of dollars and can use tens of watts to be able to transmit. These solutions are a technologic achievement enabling many ocean exploration activities; however, this leaves a gap in capability for a class of systems. This gap is lacking in providing capabilities to short range communication of small subsurface systems either to each other or to the surface. Operations of these vehicles happens in a diverse number of environments, including shallow waters, littoral environments, and high risker environments where low-cost vehicles are preferable. Such systems have an approximate cost range of less than 5-10 thousand dollars. Operations in these environments typically are at ranges of hundreds of meters and depths of tens of meters.

In this research it will be shown that the acoustic noise produced by the electrical switching of brushless electric thrusters is independent of the operation of the thruster. This approach allows small vehicles in shallow environments to transmit data without a specialized acoustic transducer. Besides eliminating the cost of the transducer, using the naturally generated motor noise requires nearly zero additional power and no additional hardware to be integrated in a system. Noise traditionally thought of as undesirable is being leveraged to make any vehicle with brushless electric thrusters capable of data communication.

The primary contribution of this work is the characterization of how the thruster behaves as an acoustic transducer while still being used to propel the system. Behaviors of interest include the impact thruster rotation has on transmitted signals, limitations of transmission medium, and determining the theoretical performance limits. This work will serve as the basis for all other work to build upon, including optimization of the data communication link leveraging the capabilities of a thruster, as well as accounting for the limitations. The goal of this work is to enable a low-cost system for small vehicles. To minimize costs and development time, the transmission side of the link shall be implemented using open-source and low-cost hardware.

### Motivations

Embry-Riddle Aeronautical University has competed in the AUVSI Robot-X competition and numerous other maritime based competitions. These competitions often require the use of hydrophones to localize an underwater target or acoustic beacon. During hydrophone measurements it was observed that electrical noise from the thrusters was being received at frequencies that interfered with the localization process. This observation led to the question of whether the thruster noise could be harnessed to transmit data to nearby vehicles without the need of a specialized acoustic transmitter. After initial experiments proved that using thruster noise to transmit data was feasible, questions arose about assessing the theoretical performance

limits of the system and determining whether a reliable communication system can be demonstrated in practice. The research in this dissertation addresses these issues.

## Chapter Outline

This section serves to outline the sections of the paper presented in this work.

- Chapter 1 This section serves to introduce the reader to the problem space, alongside the motivations behind the work. A brief discussion on core technical aspects of the technology is presented, describing how a brushless electric motor functions, how data is modulated in wireless transmission and where this technology is intended to be applied.
- Chapter 2 This chapter reviews literature relevant to underwater acoustic communication. The review is focused in three primary areas, starting with the current state of the art and developments in acoustic communication. Next, an analysis on the considerations related to wireless communication is presented. Finally, a discussion of the Fourier transformation and the necessity of the frequency domain is provided.
- Chapter 3 This section discusses the component portions of a full communication system constructed around this technology. An overview of the communication system is presented alongside discussions of each component. Discussions include both hardware and software components for both the transmitter and the receiver that will be used for the testing of the system. Sample portions of the developed firmware are shown to explain the implemented communication algorithm.
- Chapter 4 This section serves to determine the behavior of the system through the characterization of all relevant portions of the communication system. This work focuses on determining any deviation in behavior from a purpose-built acoustic transmitter. The primary areas of analysis are focused on the impact that thruster rotation has on data transmission and the performance limits imposed by the speed controller hardware.
- Chapter 5 This section investigates factors that a communication link would experience in the field but cannot be easily separated. A simulation is constructed to demonstrate the considerations that arise from these effects. Multipath and attenuation along a shallow channel are modeled and demonstration of their impact is presented.
- Chapter 6 This section discusses the testing setup, methodology and results of the conducted field trials. This testing was conducted in an environment representative of the target operational environment. Characterizations of thruster behavior at speed were validated. Beyond this, image and video data were transmitted to demonstrate a realistic data stream from an operational system.

- Chapter 7 This section investigates the results of the system characterization to determine methodologies for improving the performance of the data link. Analysis on the transmission protocol and inter-symbol interference were conducted to determine means to improve the link performance. An approach leveraging the frequency harmonics was also presented, demonstrating a means to triple the transmission baud rate.
- Chapter 8 This section serves to summarize the work and present recommendations for future research.

### Brushless Motor Overview

Vehicles of small to medium size, approximately less than 55 kgs in mass and 1.5 meters in length, typically rely on brushless electric direct current (BLDC) motors as their means of propulsion. Electrically, this type of motor consists of three or more windings, with the power being driven by a discrete source. Figure 1 shows an internal view of this type of motor, where the windings on the coils that produce the magnetic field. The rotor is the portion of the motor that actually rotates to produce thrust and is driven by the field magnets in the middle of the motor. This power driving is done by an electronic speed controller (ESC). The specifics of this driving, shown in the circuit diagram in Figure 2, are based on half-bridge inverter stages. At an ESC level, these half-bridge stages allow for the power delivered to the motors to be in phase with the rotation of the rotor.

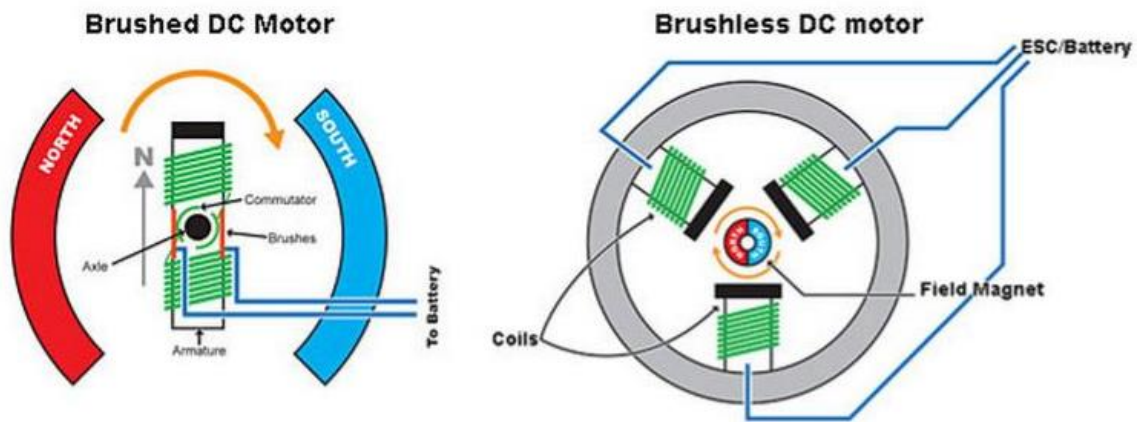


Figure 1: Brushless electric motor components (MotionControlGuide, 2021).

The specifics of how an ESC maintain this in phase power delivery can come in a variety of implementations. A common method for driving power to the motor windings is through a 6-step commutation, otherwise known as a 120-degree trapezoidal controller. In this control methodology, current is flowing between two of the three windings at any given time. When current flows through these windings, a magnetic field is produced. The permanent magnet on the rotor is driven to exist orthogonal to this field and maximizes the generated torque of the motor. To continuously drive the motor through full rotor rotation, a 6-step commutation sequency is used, shown in Figure 3. To manage the average current flowing through the

windings, pulse width modulation (PWM) is utilized, shown as the chopped signals. Winding A demonstrates this chopping at the beginning of commutation visualization for reference.

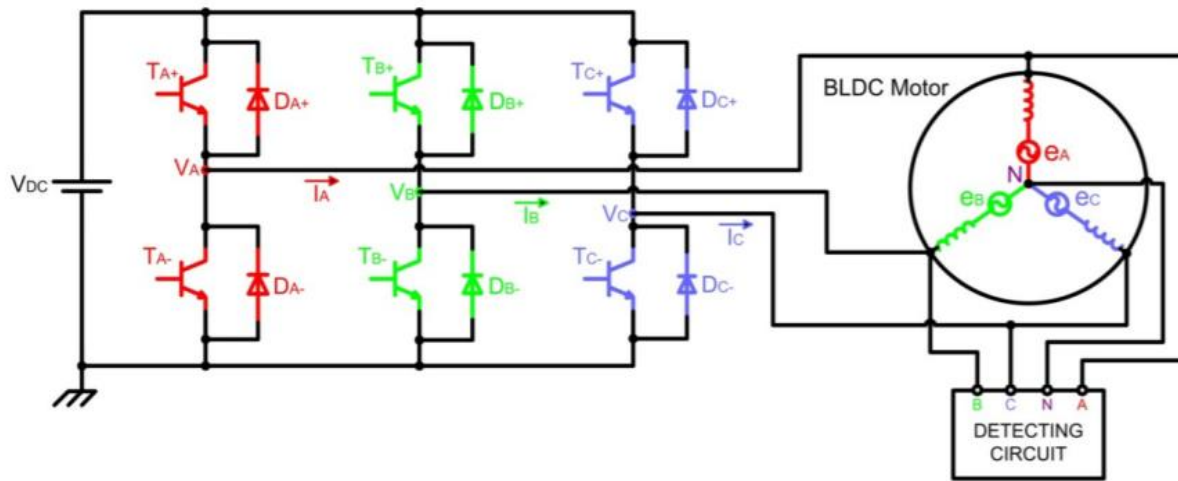


Figure 2: A three-phase BLDC motor and motor controller. The half-bridge inverter circuits and currents for each phase are color coded (Gamazo-Real, Vázquez-Sánchez, & Gómez-Gil, 2010).

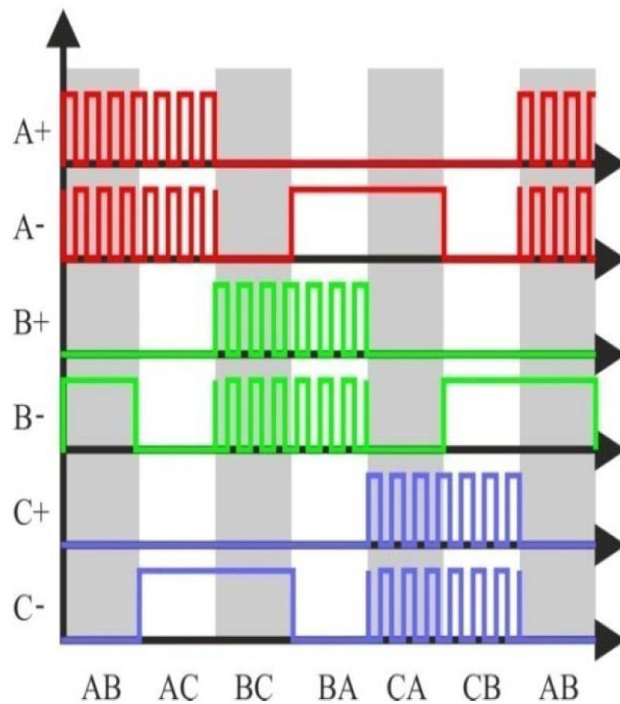


Figure 3: The motor voltages for a typical three-phase BLDC motor. Note the PWM pulses in each phase. (Gamazo-Real, Vázquez-Sánchez, & Gómez-Gil, 2010)

If the phasing of currents on the windings is correctly delivered, an emergent property around the relationship of torque and current arises. This is a simple proportionality relationship, in that more delivered current means more delivered motor torque, throughout the range of currents

that the motor can manage. Delivery of this current is accomplished through PWM. PWM ranges from 0%, or no current delivered, to 100%, or a solid signal without chopping. Modulation between these values is done at a switching frequency. As long as the PWM frequency is sufficiently larger than the mechanical response of the motor, the exact value of the frequency is arbitrary and does not affect motor operation. However, this PWM frequency does cause a corresponding acoustic emission at the same frequency and frequency harmonics.

When discussing noise produced by a thruster, the component of interest arises from the vibration of the laminations in the steel stator core and rotor. There are other components to the total thruster noise, including from propellor flex and any mechanical vibrations in the system. However, these frequencies are typically far lower frequency than what we are interested in controlling, on the order of tens of hertz as compared to thousands. This stator and rotor noise is caused by the magnetic forces generated by the currents driven. As discussed, the frequency of this power delivery determines the transmitted acoustic frequency.

This property of noise produced through the modulation frequency is not without application already. Often it can be the case that the general status of an ESC is desirable to know, however getting this information can prove difficult amongst a myriad of different usage applications for the controller, and equally many mounting locations for the ESC. To keep the cost of the controller down and allow for statuses to be sent on any system, acoustic messages produced from the attached motor, rather than diagnostic lights or buzzers are employed. These signals are produced by modulating the motor in at an audible frequency. Produced data commonly includes information such as the ESC being active, especially common in aerial vehicles, where exposed propellers can be hazardous if they begin to spin. Beyond this, loud beeps can be produced to help in locating lost vehicles such as quadrotors and fixed wing aircraft.

Although anecdotally we have evidence that the frequency can be changed for purposes of communicating information, internal validation of this principle on an ESC is needed. The ESC presented is the VESC 4 controller, an open-source project with the ability to control the parameters of the system. This controller powered a Blue Robotics T200 thruster, a popular thruster solution for small marine robots. For testing, a single tone of 21 kHz was to be sent by the thruster, demonstrating that an individual frequency could be targeted and accurately produced. The acoustic response of the thruster is shown in Figure 4 (T200 Thruster, 2021) (Flipsky, 2021). As can be seen, the target frequency is by far the dominant frequency response, rising above the noise floor visibly. This indicates that the conceptual understanding that it is the electrical switching of the motor producing the audible frequency, and that it can be configured.



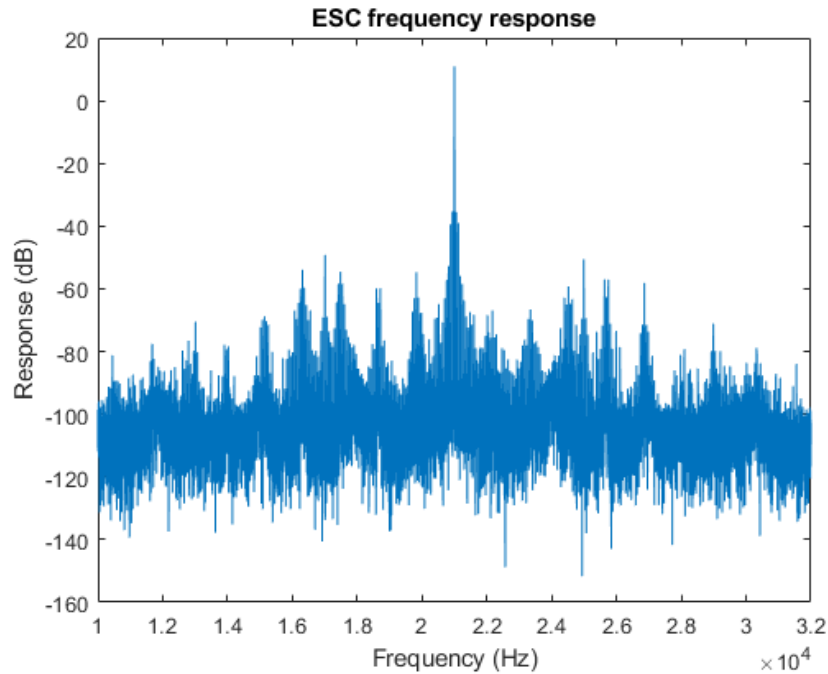


Figure 4: The measured acoustic noise versus frequency of a thruster driven by an Afro ESC.

Looking beyond hobbyist level ESCs and small motors, fundamentally nothing about the control of a large motor changes, with PWM still being employed. Looking at a far larger system, Figure 5 shows the acoustic noise spectrum of a 6kW motor being driven with a PWM frequency of 6 kHz. Since the PWM waveforms consist of 6 kHz pulses of varying duty-cycles, the expected behaviour of the system would be to see a spike at 6 kHz, as well as at the harmonics, in this case 12 and 18 kHz. From the plot, it can be seen that these responses are behaving as expected, with response spikes of over 20 dB over the noise.

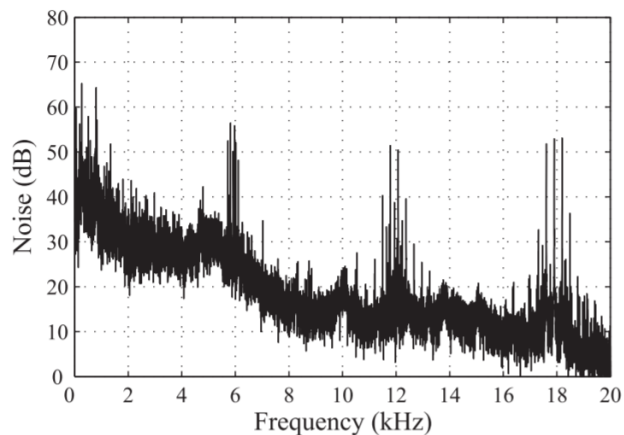


Figure 5: The noise spectrum of a 6kW motor being driven by a 6kHz PWM frequency (Binojkumar, Saritha, & Narayann, 2015).

As the property of producing the electrical switching frequency as ambient noise is a property of how a brushless electric motor controller functions, it is an effect seen across all control schemes. It is useful to take a deeper look into the control operation to see why this is the case. For this research, the widely used field-oriented control (FOC) algorithm was selected. Field-oriented control offers an efficient means of controlling a motor, making it a popular choice for battery powered systems like the target vehicles for this work. Of note in a sensorless motor, a direct measurement of the position of the motor in its rotation is not possible. An estimation algorithm must be used instead, with a phase-locked loop (PLL) estimator to track the position, and as such rotation rate, of the motor. A visualization of this control scheme is shown in Figure 6. In considering this diagram, most of the parameters shown are not relevant to the discussion. The important portion to consider is the 3-phase inverter delivering current to the motor. Of note, no frequency is present when discussing this power delivery, as it is a flexible parameter. The FOC algorithm provides a current control over the phases of the motor to control the angular velocity of the motor. Current delivery is not directly provided, but rather the signal is chopped, a result of the three-phase commutation. This chopping rate is the switching frequency of the controller. From this controller characteristic, the frequency of power delivery can be freely shifted without interfering with the delivered currents to the motor windings.

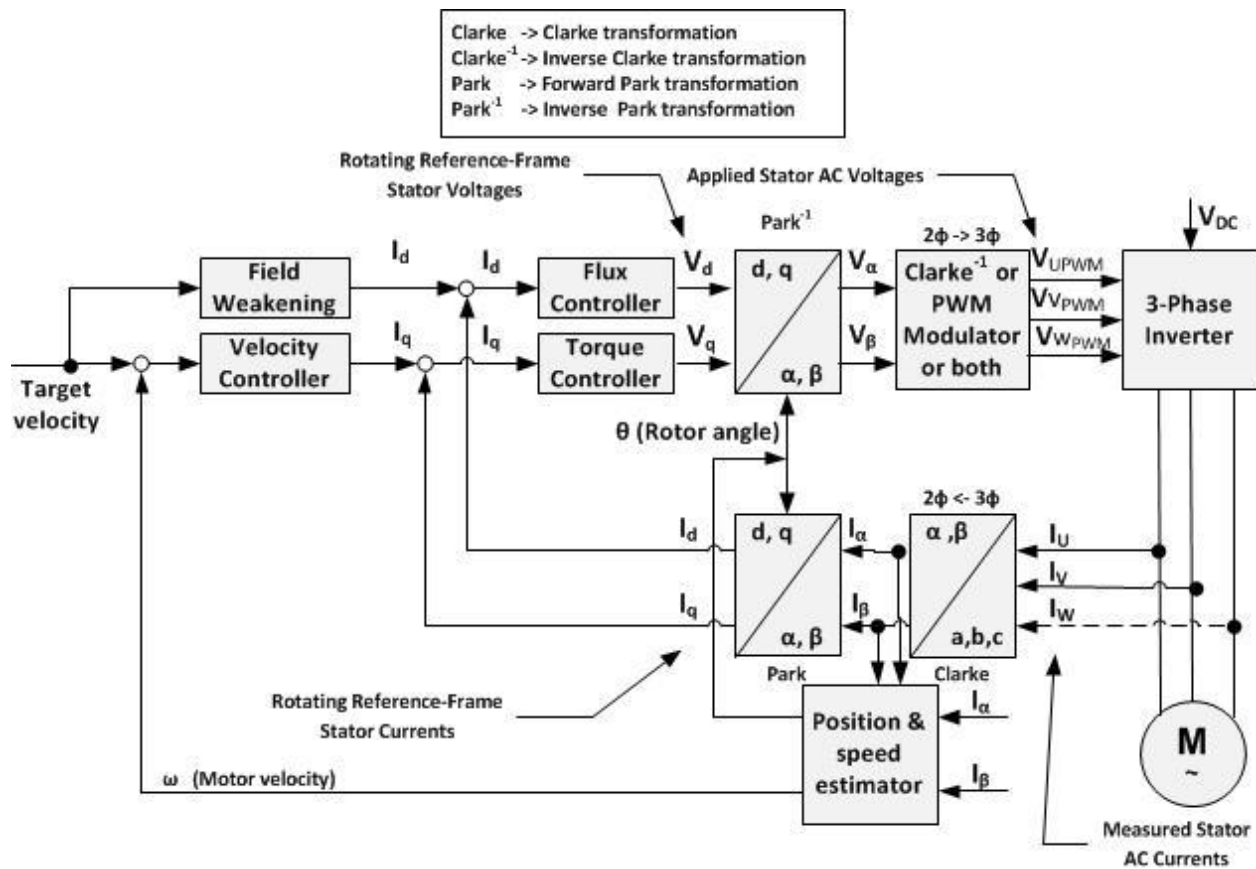


Figure 6: Field oriented control algorithm diagram (Holtz, 2002).

## Modulation Analysis

To determine the appropriate modulation scheme transmitting acoustic data from the motor, an analysis of all feasible modulation schemes was conducted. Schemes that were considered were as follows: Amplitude Modulation (AM), Phase Modulation (PM), Frequency Modulation (FM). Among these modulation schemes, combinatorial methods such as amplitude and phase, as well as M-Key versions where a symbol represented more than one bit were also included. Figure 7 shows a visualization of these schemes, in this case in a binary mode where each transmission period represents one bit.

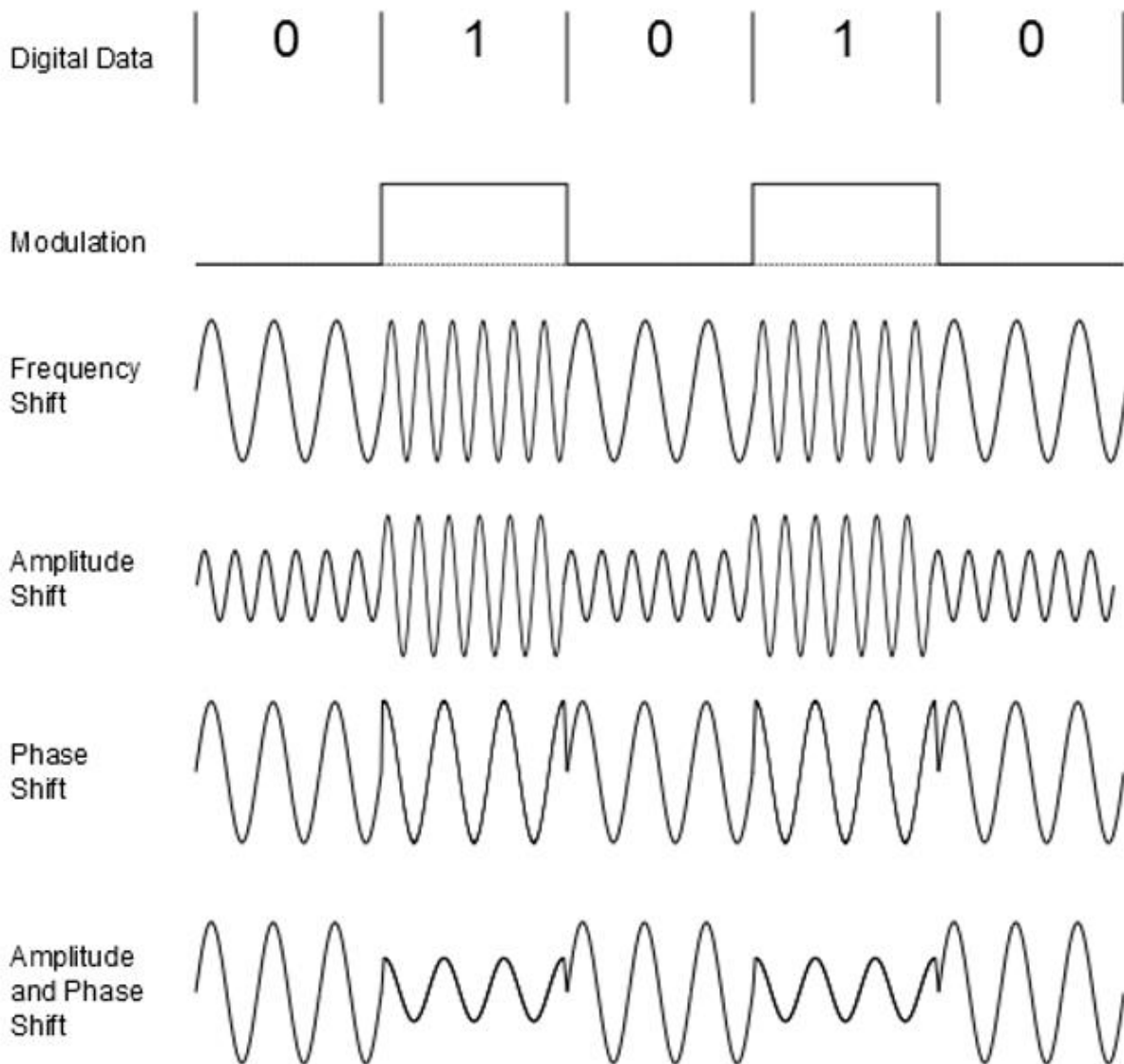


Figure 7: Modulation schemes visualized (Knowledge Amplifier, 2021).

Building from the conclusions drawn from the how a brushless motor operates, amplitude modulation must be removed. As switching noise is always present, power transmission can be considered an ambient property of the thruster and it does not change with the speed the

thruster is rotating. Therefore, the amplitude cannot be easily controlled. Furthermore, if the goal is to maintain the operation of the thruster without any interference, phase modulation can be removed from consideration. The control algorithm of the ESC takes control over this parameter, and it cannot be discretely controlled. If signal phase were controlled, it would manifest as physical rotations in the motor independent of the desired speed.

As opposed to amplitude and phase, frequency is independently controllable on the ESC with no impact the operation of the thruster. Within the realm of frequency modulation, there are multiple approaches that can be implemented. Shown above is Frequency Shift Keying (FSK), where a symbol is represented by a single frequency value. An alternative approach to using a single frequency to represent each symbol is to use a pattern of frequency changing over time. The most common version of this is known as linear frequency modulation (LFM), where the frequency changes with respect to time over a duration. A visualization of this signal type can be seen in Figure 8. The benefit of this approach is that it is more resistant to noise due to it having a distinct pattern, resulting in a performance increase in decoding the received signal. However, the cost of this approach is that individual LFM symbols require more time to transmit. The Seatrac modem for instance, a lower cost commercial model, has a maximum data rate of 100 bit/s, whereas initial tests with FSK thruster transmission showed rates of 500 bit/s (Neasham & Sharphouse, 2015) (Butka, Cronin, & Romney, 2018). This throughput differential in the links is large enough that for initial testing, an FSK approach will be used. Until the need for a high link reliability can be deemed necessary, the work shall strive to push the optimization goal and increase the link capacity.

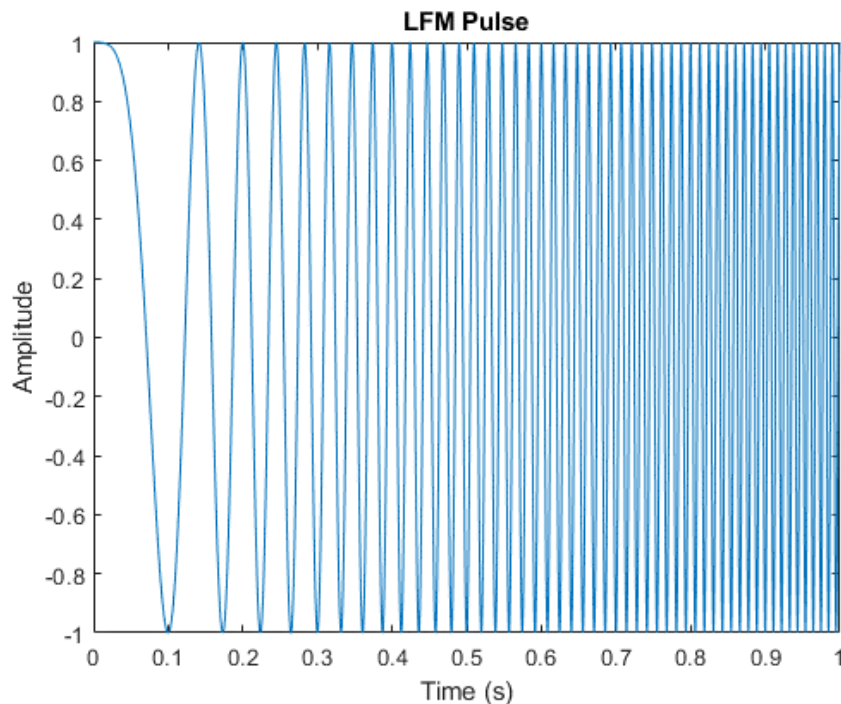


Figure 8: LFM Chirp

### Proposed Area of Work

From these initial considerations, the proposed system is to create a short-range data link for communication between multiple subsurface vehicles or subsurface to surface vehicles. The link will use the already existing vehicle thrusters, without reducing the typical operational capabilities of the thruster. This also means communication capabilities can be added to the vehicle without additional cost or integration into the vehicle. By leveraging the properties of the motor, operating the modem functionality of the thruster should bear close to zero overhead for transmission power. On the other end of the data link, a system capable of receiving the transmitted signals will be utilized to create a complete communication system as well as to validate theoretical predictions about the behavior of the system.

This system is not without limitations, both in terms of power and control over the signals being transmitted. The transmitted power is derived from the motor itself as opposed to the being generated by the transducer. This fundamentally caps the range that can be transmitted. The other major limitation is a product of the ESC, in that control over the signal phase is relinquished to the FOC algorithm to maintain the motor operation. This limits the maximum decoding accuracy and reduces the symbol rate because without phase control, established methods such as a phase lock loop cannot be employed to track the signal and properly estimate the position of upcoming symbols.

## Chapter 2: Literature Review

In this section, themes central to acoustic localization and communication are examined. This investigation will begin with the history of underwater acoustics leading into the modern industry. Following this, the current technology will be considered, looking at the diverse technical solutions that exist. Following this, the technical aspects of localization and communication systems will be reviewed alongside the primary design considerations external to the technology that must be accounted for in the implementation of this type of system. Finally, a discussion of testing and verification of system capabilities is presented.

### History

The foundation of the science of underwater acoustics began with the musings of Leonardo da Vinci in 1490. In this he writes: "If you cause your ship to stop and place the head of a long tube in the water and place the outer extremity to your ear, you will hear ships at a great distance from you". Although da Vinci wrote this, it took until 1687 when Isaac Newton first described sound in mathematical terms in the work, *Mathematical Principles of Natural Philosophy*. Again, as with da Vinci, Newtons' work would not be built on again until the 1800's, where the first applied measurements of the speed of sound were taken in 1826 by Daniel Colladon and Charles Sturm. The end of that century was truly the beginning of the modern era of acoustic theory, with Lord Rayleigh's writings on the *Theory of Sound*.

Building off the theoretical and applied beginnings, modern acoustics truly became actively researched and developed with sonar technology for World War I and II, particularly for the detection of mines and submarines. From this basis, the need for additional technologies and improvements of current capabilities drove the iteration of the technology and carried us into the modern era, where the technology works on the same fundamental basis, with merely greater theoretical backing and engineering capabilities behind them (Clay & Medwin, 1977).

### Acoustic Modem

The transition from the theoretical beginnings of underwater acoustics was not without challenges. As discussed, there are many technical challenges that need to be considered when developing communication systems. Beyond these challenges, the performance goals of the system must be considered in the development of a modem. These considerations include data rate, error rate, range, power, and other criteria. Methodologies for analysis and verification of these is needed to ensure development goals are met as well as provides a comparison to existing technologies to judge the merits of the performance against.

### Communication Reliability

The transmission of data is inherently not without risk. Modulation of data, transmission range, frequency, and propagation effects can all impact the ability to receive error-free data. When selecting the modulation scheme to be used, the relationship between the bit error rate (BER)

and the energy per bit to noise power spectral density ratio ( $E_b/N_o$ ) must be considered. A representative table of this was created for frequency shift keying, shown in Figure 9. As the data rate of the link increases, the reliability of the transmission decreases (Kaur, Kaur, & Sandhu, 2016). Determining the impact of noise and the required reliability of the link will guide modulation decisions. This plot also shows that simulation of the transmission behavior is possible, which can provide a useful means for testing cases that are logistically difficult in the real world, such as longer ranges or with different quantities of ambient noise.

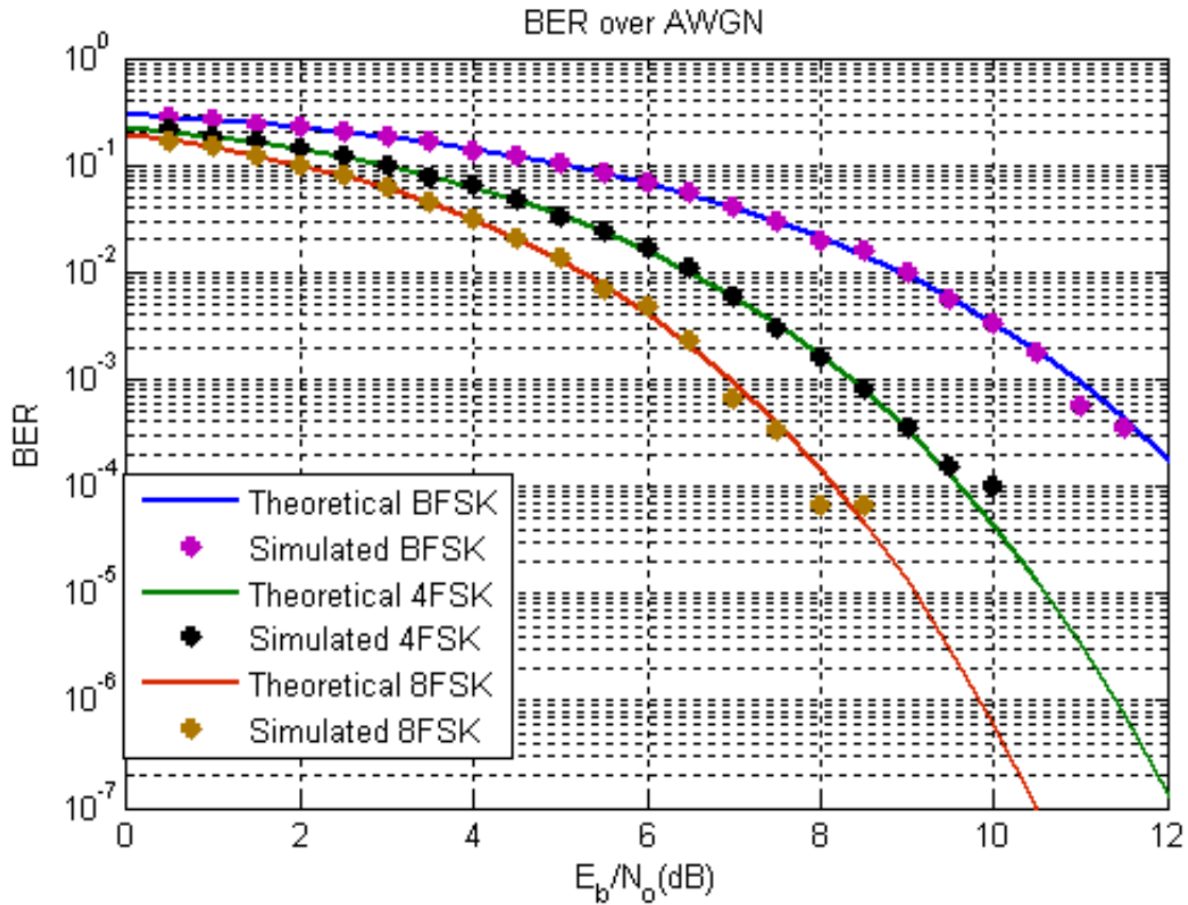


Figure 9: FSK modulation BER (Almashhadanai, 2017).

Beyond the scheme of modulation itself, the other primary consideration in communication comes in the protocol employed for sending data. Typically, the aspect that is relevant to reliable communication is error detection or correction codes that are added on to the transmitted data. As in much of the communication field, there are many solutions to this problem; each with solution has different performance characteristics and behaviors over various BER values. In the work by Naderi, a comparative study of error mitigation approaches was conducted. To this end, varying coding schemes were implemented to compare the behavior of the Peak Signal-to-Noise Ratio (PSNR) over varying bit error rates (Naderi, Rabiee, Khansari, & Salehi, 2012). Looking at a

representative plot of this in Figure 10, some different behaviors over the range of BER values can be seen. Most of the Automatic Repeat Request (ARQ) schemes for instance, show the ability to correct errors at low error rates, indicative of the constant PSNR. This is a desirable characteristic; however, it relies on the ability to have bi-directional communication, which in the case of the proposed system is not possible. Beyond this characteristic, the other metric that should be considered is the slope of the produced curves. This physically is indicative of the impact that the noise of the environment can have on the integrity of the signal transmitted. As can be seen, there is a large range of sensitivities to bit errors, each with certain overhead and performance considerations associated. For the proposed system, a comprehensive analysis on the nature of the data transmission needs to be conducted to select the best decision for the implementation of the modem. As the data being sent from the acoustic modem is being directly used in the localization of the device, a particular focus on resilience or detection of errors will likely be the key factor.

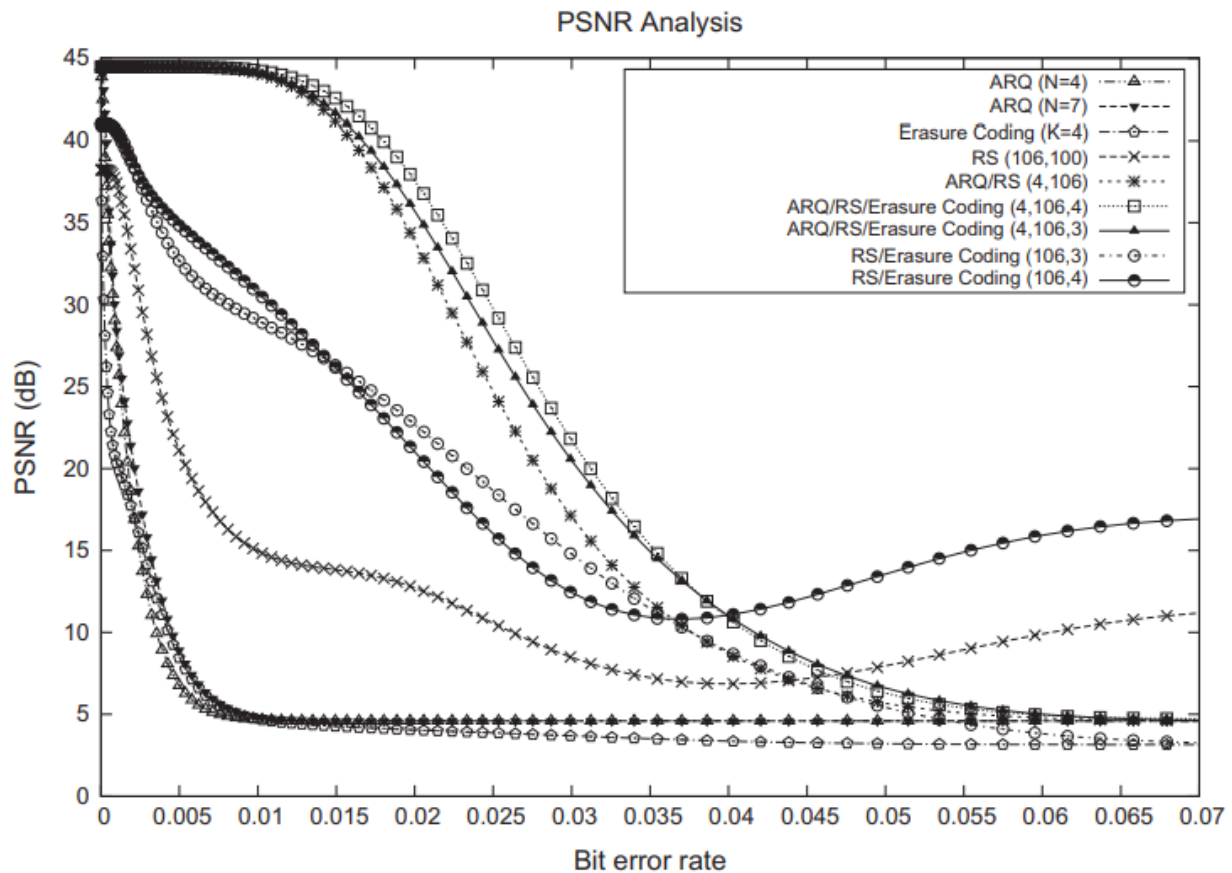


Figure 10: Average PSNR under varying channel bit error rates (Naderi, Rabiee, Khansari, & Salehi, 2012).

When considering the impact of SNR and encoding scheme on BER, error correcting codes must be acknowledged. This refers to a portion of the message transmitted being used to detect and fix errors in a transmission. In implementation, this can represent two main design decisions in the overall communication link. The first is the reduction in the percentage of bandwidth



allocated to data, meaning that the same bit rate is used, but less payload per second is transmitted. The second methodology involves increasing the transmission rate. While this would increase the error rate, the extra bandwidth can be allocated to correcting errors, potentially offsetting the error increase while maintaining the payload data rate. Although an important design consideration in the selection of encoding schemes overall, error correction codes will not be presented in this work. The specific encoding scheme in this work serves to validate predictions on behavior, not to be optimized to find peak performance.

### Current Modem Technology

Underwater acoustic communication (UWAC) at its core behaves the same as any other wireless communication system. It provides a means of communicating throughout a space without physical communication. Like most areas that implement wireless communications, the commercial and research space is full of a diverse number of solutions implemented to serve varying use cases. The primary factors in a given application used to select a modem solution are that of bandwidth, data rate, power consumption, range, and cost. A review of the current commercial and research developed modems was carried out by Sendra in an overview of the current state of the art in acoustic modem technology. Table 1 shows the collected results of this work (Sendra, Lloret, Jimenez, & Parra, 2016). As can be seen, there is a wide variance of capabilities filling many of the use cases one would have in underwater communication. It should be noted that the proposed solution does not serve to replace any of these solutions, merely supplement them through removing physical constraints of a transmitter and in a reduction in cost.

Table 1: Comparison of commercial and research modems (Sendra, Lloret, Jimenez, & Parra, 2016).

COMPARISON OF COMMERCIAL DEVICES AND DEVELOPED DEVICES

Underwater Acoustic Modem	Modulation	Carrier Frequency	Bandwidth	Data rate	TX Power consumption	RX Power consumption	Idle Power consumption	Max. distance
<b>DEVICES DEVELOPED BY RESEARCH GROUPS</b>								
[5]	FSK	320 Hz and 10 kHz	1 kHz	96 bps and 2400 bps	12 mW	24 mW	3 $\mu$ W	100 m
[19]	n/a	n/a	n/a	1-10 Mbps	n/a	n/a	n/a	100 m
[25]	FSK	35 kHz	6 kHz	200 bps	750 mW		35 mW	350 m
[27]	KSK	85 kHz	n/a	1 kbps	108 mW	24 mW	8.1 $\mu$ W	2400 m
[28]	n/a	9-14 kHz	75 kHz	1.2 kbps	n/a	n/a	n/a	2000 m
[21]	BPSK	80 kHz	n/a	80 kbps	n/a	n/a	n/a	50 m
[30]	FSK	30 kHz	n/a	300 bps	n/a	n/a	n/a	400 m
[32]	FSK	9 kHz	n/a	1900 bps	n/a	n/a	n/a	200 m
<b>COMMERCIAL DEVICES</b>								
Aquatec AQUAModem 1000 [36]	n/a	9.75 kHz	4.5 kHz	2000 bps	20 W	0.6 W	1 mW	5000 m
DSPComm AquaComm Marlin [37]	n/a	23 kHz	14 kHz	480 bps	1.8 W	0.252 W	1.8 mW	1000 m
DSPComm AquaComm Mako [38]	n/a	23 kHz	14 kHz	240 bps	1.8 W	0.252 W	1.8 mW	100 m
DSPComm AquaComm Orca [37]	n/a	14 kHz	100 kHz	0.007 bps	0.252 W	1.8 W	25.2 mW	3000 m
Desert Star Systems SAM-1[38]	n/a	37.5 kHz	9 kHz	154 bps	32 W	0.168 W	n/a	1000 m
EvoLogics S2CR 48/78USBL [39]	n/a	48-78 kHz	30 kHz	31200 bps	18 W	1.1 W	2.5 mW	1000 m
EvoLogics S2CR 40/80 USBL [39]	n/a	38-64 kHz	26 kHz	27700 bps	40 W	1.1 W	2.5 mW	1000 m
EvoLogics S2CR 18/34wise [39]	n/a	18-34 kHz	16 kHz	13900 bps	35 W	1.3 W	2.5 mW	3500 m
EvoLogics S2CR 12/24 USBL [39]	n/a	13-24 kHz	11 kHz	9200 bps	15 W	1.1 W	2.5 mW	6000 m
EvoLogics S2CR 7/17 USBL [39]	n/a	7-17 kHz	10 kHz	6900 bps	40 W	1.1 W	2.5 mW	8000 m
LinkQuest UWM1000 [40]	n/a	35695 kHz	17.85 kHz	17800 bps	1 W	0.75 W	8 mW	3500 m
LinkQuest UWM2000 [40]	n/a	35695 kHz	17.85 kHz	17800 bps	2 W	0.8 W	8 mW	1500 m
LinkQuest UWM2000H [40]	n/a	35695 kHz	17.85 kHz	17800 bps	2 W	0.8 W	8 mW	1500 m
LinkQuest UWM2200 [40]	n/a	71.4 kHz	35.7 kHz	35700 bps	6 W	1 W	12 mW	1000 m
LinkQuest UWM3000 [40]	n/a	10 kHz	5 kHz	5000 bps	12 W	0.8 W	8 mW	3000 m
LinkQuest UWM3000H [40]	n/a	10 kHz	5 kHz	5000 bps	12 W	0.8 W	8 mW	3000 m
LinkQuest UWM4000 [40]	n/a	17 kHz	8.5 kHz	8500 bps	7 W	0.8 W	8 mW	4000 m
LinkQuest UWM10000 [40]	n/a	10 kHz	5 kHz	5000 bps	40 W	0.8 W	9 mW	1000 m
Teledyne Benthos Atm9xx [41]	PSK	11.5 kHz 18.5 kHz 24.5 kHz	5 kHz	15360 bps	20 W	0.768 W	16.8 mW	6000 m
Teledyne Benthos Atm9xx [41]	MFSK	11.5 kHz 18.5 kHz 24.5 kHz	5 kHz	2400 bps	20 W	0.768 W	16.8 mW	6000 m
Teledyne Benthos Atm88x [41]	PSK	11.5 kHz 18.5 kHz	5 kHz	15360 bps	84 W	0.756 W	16.8 mW	6000 m
Teledyne Benthos Atm88x [41]	FSK	11.5 kHz 18.5 kHz	5 kHz	2400 bps	84 W	0.756 W	16.8 mW	6000 m
TriTech MicronModem [42]	n/a	22 kHz	4 kHz	40 bps	7.92 W	0.72 W	n/a	500 m
uComm Underwater Acoustic Modem [43]	n/a	26 kHz	n/a	9000 bps	40 W	60 mW	3 mW	3000 m
AM-OFDM-S [44]	OFDM	21-27 kHz	n/a	1600 bps	5-20 W	0.7W	0.13 mW	4000 m
MATS 3 G 12 KHZ [45]	n/a	10-15 kHz	n/a	Up to 7400 bps	75 W	0.6 W	40 mW	15 Km
GPM 3000 Acoustic Modem [46]	DSSS	n/a	n/a	Up to 1200b*s	300W	1.8 W	0.08 W	25 Km

Current Modem Research

The systems presented above represent the current state of the art in terms of production caliber devices. Although some are developed by research groups, these devices still have reached levels of reliability to be used in research applications and vehicles. As exploration of the oceans expands, novel technologies are being developed to improve upon the modern acoustic modem.

### Full-Duplex Acoustic Modems

The first modem technology of note is the implementation of a full-duplex modems. A full-duplex modem allows for both sides of an acoustic link to be transmitting and receiving data at the same time, within the same frequency band. In terms of channel capacity, this effectively allows for twice the amount of data to be transmitted within a given frequency band. To achieve this transmission capability, these modems function similarly to any other traditional modem, but with an additional stage used to filter the received acoustic data. As both sides of the link can be within the same band as each other, the transmission from one side would interfere with its own ability to receive data from the other side of the link. This noise is not only within the same frequency band as any other transmission source, but it is also significantly louder than another source at range, as attenuation over the size of a modem is nearly nonexistent. This means that even systems using different bands could experience the transmitter overwhelming the attached receiver, in terms of amplitude or in frequency harmonics. To remove this self-induced noise, an analog cancelation of the transmission source from the receiver is utilized. As on a given modem, the distance between the transmitter and receiver is known, the transmitted signal can be routed on the circuitry to be added into the received signal, shown in Figure 11. If this is done 180 degrees out of phase with the received transmission noise, the signal is canceled from the receiver, and only transmissions from another source are received. (Shen, Henson, & Mitchell, 2019)

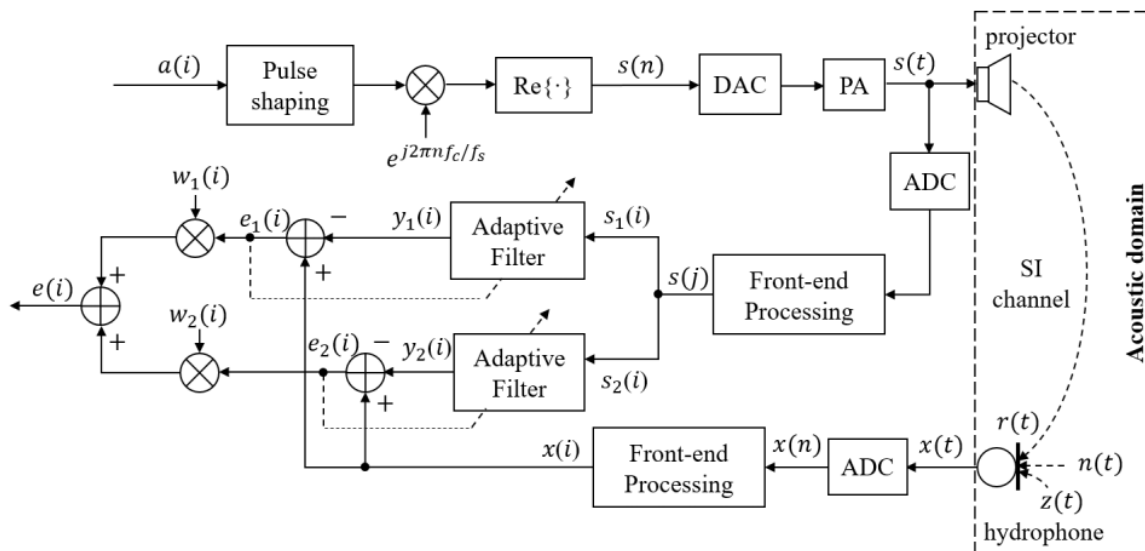


Figure 11: Full-duplex acoustic modem circuit diagram for interference cancellation (Shen, Henson, & Mitchell, 2019).

### Acoustic Modem Networking

There are environments in which many acoustic modem systems may be in operation in conjunction with one another to establish a means of routing data over longer ranges or at higher speeds than any one modem can achieve. Much like the full-duplex system, this too can represent a complex challenge when many modems may be communicating withing the same frequency

band as one another. Modem networks also have the additional challenges around minimizing the power usage of the network itself and the network being unable to know the location of all or any parts of itself. Research into effectively routing data through these networks takes many approaches (Tariq, Shafie Abd Latiff, & Ayaz, 2017).

#### Modem Testing

The target for this work is in coastal or littoral environments, where the environment can have a large impact on adding noise to the signals. In the physical sense, this environment can be characterized a few ways. Large length to depth ratios of communication links represents coastal and river bodies. In this environment, the presence of phenomena such as signal fading and phase fluctuation due to multipath are quite high and should be represented. The other targeted environment would be near piers or solid concrete structures where reflection effects come from all angles and represents a difficult challenge in any localization and communication scheme. In the work presented by Galvin, a representative test environment, shown in Figure 12, spanning two different ranges of a shallow channel is presented. Test cases of 2.2 km and 900 m yielded length to depth ratios of 150:1 and 70:1, respectively (Galvin & Coates, 1995). While producing ratios in testing of this distance may not be perfectly achievable, this metric is something to remain cognizant of while performing testing on the proposed system.

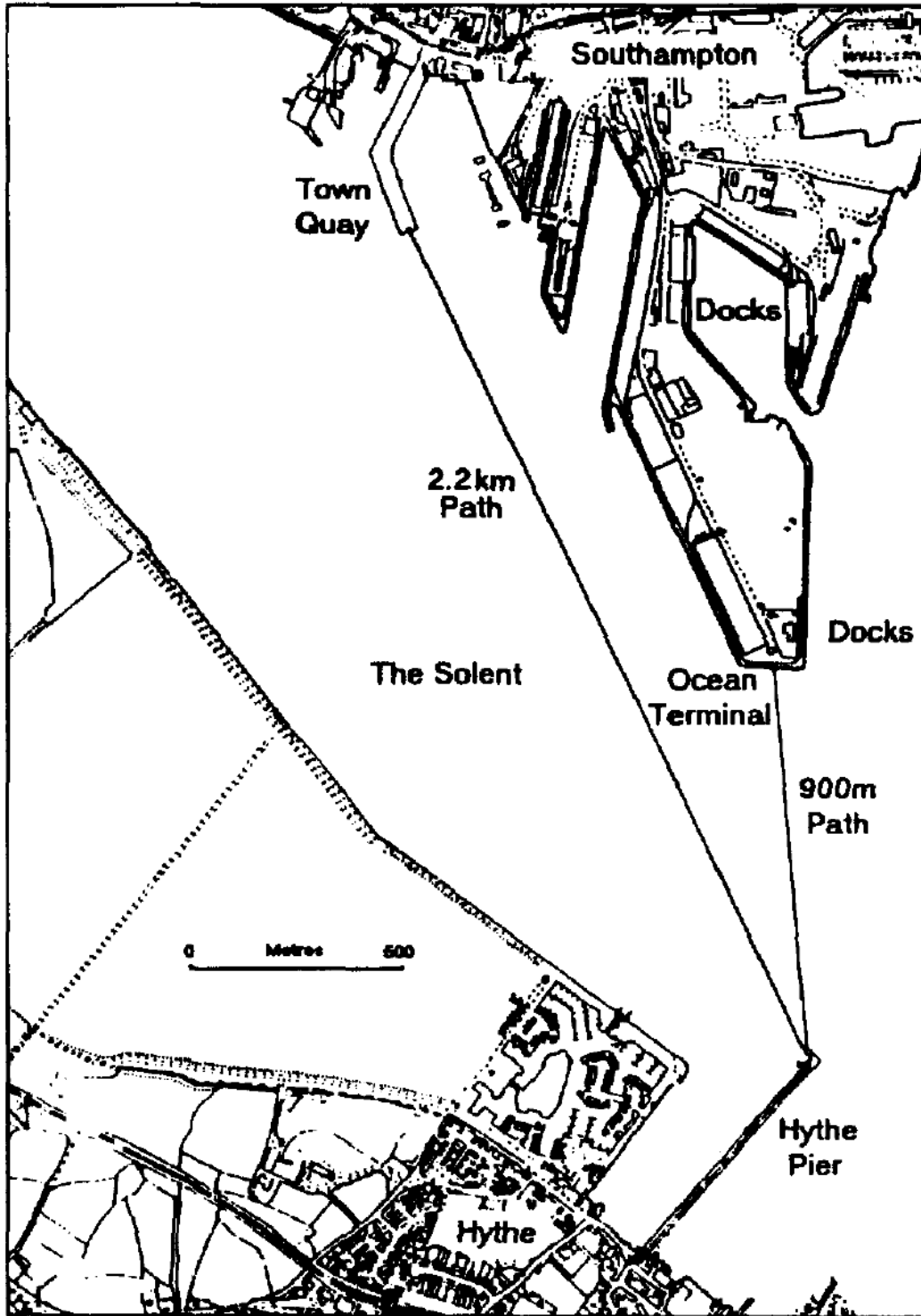


Figure 12: Shallow channel test case (Galvin & Coates, 1995).

## Signal Propagation Effects

As communicating wirelessly inherently results in the transmission interacting with the environment it travels through, there are external factors impact the received signals. These external effects are common to all forms of wireless communication, with different transmissions such as radio frequency or optical having to account for them differently. The impact of effects includes frequency shift, phase shift, and amplitude changes. The implications of these changes on the signal are that it makes the decoding of the data more difficult to accomplish by obfuscating the data transmission. A key metric in communication is the signal to noise ratio (SNR) of the received transmission. What this metric describes is the portion of the received signal that is transmitting the data of interest over the portion of what is received that is not contributing to this.

## Attenuation and Scattering

In acoustic communication the primary source of degradation along the transmission paths are scattering and attenuation. Attenuation describes the energy lost through propagation in a medium. As most all medium have an associated viscosity, there is a thermal consumption of energy caused by this viscous interaction. Stoke's law of sound attenuation describes the relationship for a Newtonian fluid, which water is such a fluid. Equation 1 describes the nature of how a signal attenuates, where  $\alpha$  is the rate of amplitude decrease,  $\eta$  is the dynamic viscosity coefficient,  $\omega$  is the angular frequency,  $\rho$  is the fluid density, and  $V$  is the speed of sound in the medium (Stokes, 1845). Equation 2 shows the relationship describing the actual decrease in amplitude, where  $A(d)$  is the amplitude at some distance  $d$ , and  $A_0$  is the original amplitude. The behavior that can be seen from this is at the amplitude of the wave will decrease by a factor of  $1/e$  per meter the sound propagates.

*Equation 1: Stokes law of sound attenuation*

$$\alpha = \frac{2\eta\omega^2}{3\rho V^3}$$

*Equation 2: Amplitude reduction from Stoke's law*

$$A(d) = A_0 e^{-\alpha d}$$

A summary characterization of these impacts was completed by Stojanovic and Preisig. Figure 13 shows representative curves of how frequency attenuates and its impact of different ranges of testing (Stojanovic & Preisig, 2009). Of note is the flattening of the curve throughout the frequency band as the range decreases. The target of this work is focusing on shorter range communication, less than 100m, for small systems. As such, this effect should not be dominant, but must be considered if ranges are scaled or a high frequency band is selected.

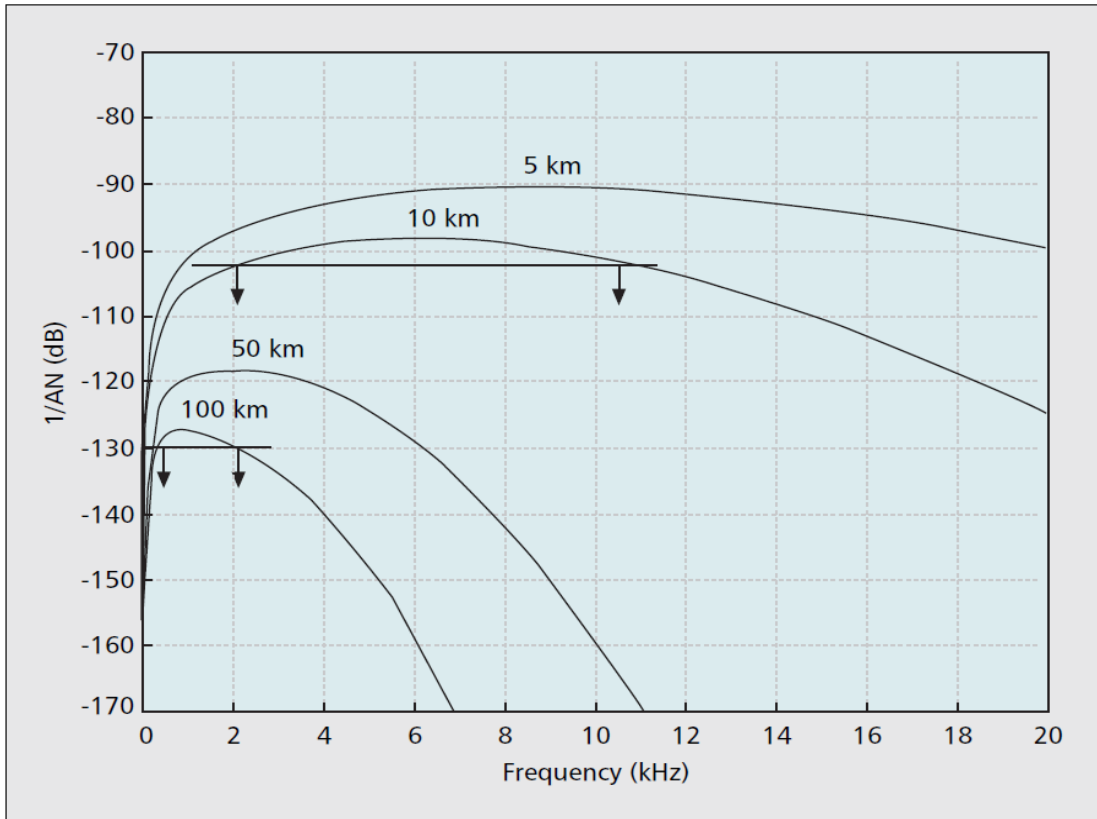


Figure 13: Attenuation throughout the frequency band (Stojanovic & Preisig, 2009).

Scattering results from distributed particles, bubbles, or any other change in material experienced by the primary transmission path. Physically, it represents the reduction in power of the transmitted signal by radiating a portion of that power off the material scattering. In shallow water communication, common sources of scattering are often present, with sediment and particulates coming off the sea floor as well as bubbles being often present resulting from water motion. This manifests as a reduction of overall received power and has nearly no mitigation available. At the ranges of the links expected, on the order of hundreds of meters, the effect is not dominant in the received signal power, much like attenuation. Unlike attenuation, there is no general approach to modeling the impact off scattering in a channel. Statistical models of experimental tests have shown that in some cases Rayleigh fading or Jakes' model can be applied, however this result is not consistent in all tests. As such, the impact of scattering will not be attempted to be isolated in any testing or simulation, rather it will be considering included in the noise floor of the environment.

#### Range Based Power Falloff

Beyond the impacts of scattering and attenuation at range, it is prudent to consider because of how sound propagates, there is a reduction in signal strength when transmitting at any range. The relationship of power and range is shown in Equation 3, where P is signal power. This effect is a result of how transmitted power radiates outwards in a spherical like manner. Figure 14

visualizes this effect with a transmission that is a segment of a sphere, a typical shape for a transducer with directivity. Across the surface areas of each range multiple ( $r$ ,  $2r$ ,  $3r$ , ...) the power is constant; however, the power density decreases as the surface area increases. This reduction in power directly relates a reduction in SNR. Equation 4 shows this relationship, where SNR is the signal to noise ratio,  $M$  is the number of bits per symbol,  $E_b/N_o$  is the energy per bit to noise power spectral density,  $P$  is power,  $G$  is gain,  $K$  is Boltzmann's constant,  $T$  is the effective noise temperature,  $B$  is bandwidth,  $\lambda$  is the transmitted frequency wavelength,  $R$  is the transmission range and  $\eta$  is the efficiency. The subscripts  $t$  and  $r$  refer to the transmitter and receiver, respectively. When considering a link broadcasting at a desired range, this relationship shows what parameters of the communication system can be changed to reach the desired signal to noise ratio. Practically speaking,  $P_t$ ,  $G_t$ ,  $G_r$ ,  $\lambda$  are the variables potentially adjustable. In the confines of a thruster as a transmitter, only the receiver gain and wavelength are discretely accessible, as the transmitter power and gain are nonadjustable hardware properties. What this tells us is that in the design of the full communication system, extra considerations should be taken into the design of the receiver as well as the selection of the transmission band to ensure the reliability criterion a link can be met.

Equation 3: Range squared power falloff

$$P_{received} \propto \frac{1}{Range^2} * P_{transmitted}$$

Equation 4: Link budget equation

$$\frac{SNR}{M} = \frac{E_b}{N_o} = \frac{P_t G_t G_r}{KTB} \left( \frac{\lambda}{4\pi R} \right)^2 \eta$$

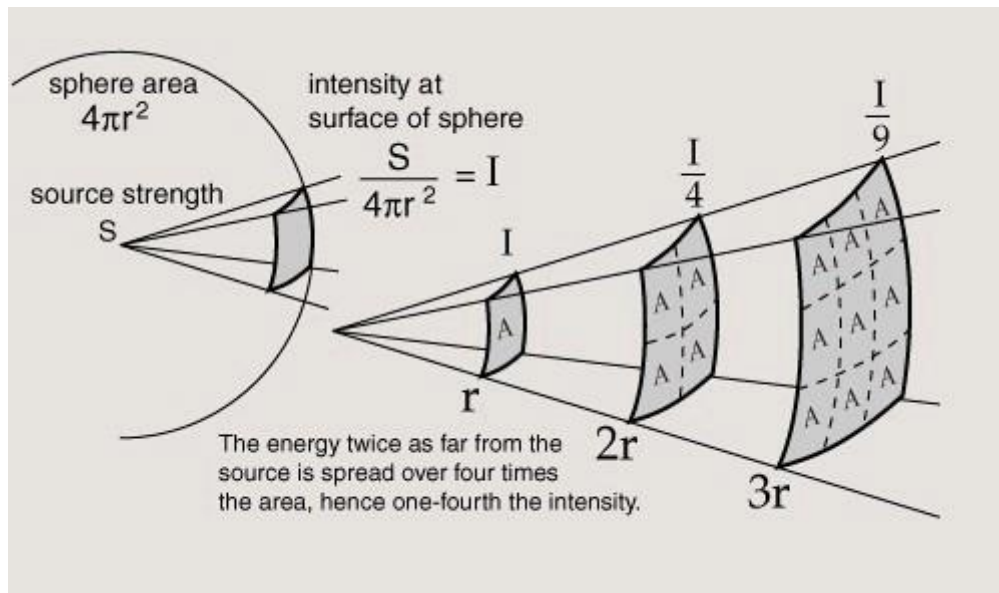


Figure 14: R squared power falloff (HyperPhysics, 2021).



## Multipath

Multipath is the result of sound reflecting throughout surfaces in the environment. Where multipath differs from scattering is in the impact it has on the received phase angle of the signal. As sound transmitted spreads spatially, it will come into contact with portions of the environment that can reflect. This reflection will bounce the signal in a way the receiver will pick up, albeit delayed. A visualization of this effect is shown in Figure 15, as can be seen, the received signal is quite different upon reception, with both alterations to its amplitude over time as well as the time period it occupies. In the context of communication, this can mean that individual symbols spread beyond their allotted period and can interfere with later signals.

### Multipath - Distortion

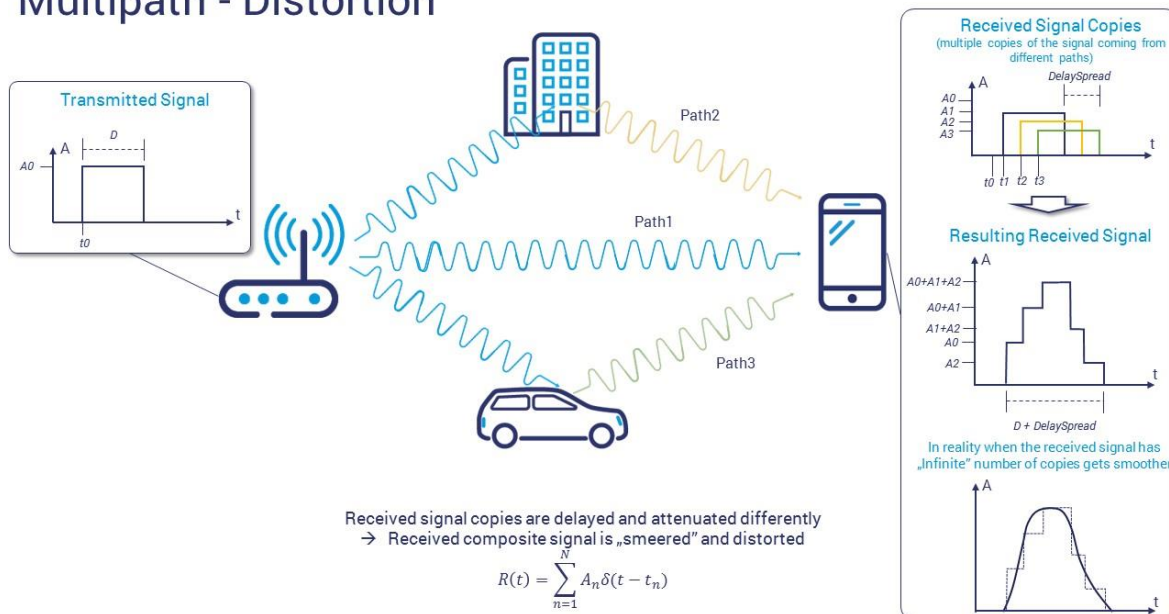


Figure 15: Multipath visualization (Grandmetric, 2021).

Multipath is especially relevant in the shallow conditions proposed for operation, where the ground, particulates suspended, and the surface of the water all provide close sources of reflection. For reference, the transmitter and receiver in this test case were mounted on fixed mounts 4 and 2 m above the seafloor, and at a range of 1 km, with a total water height between 9 to 14 m between the two. As shown in Figure 16, this can have a large impact on the intensity of the arrived signal, and as such the SNR (Stojanovic & Preisig, 2009). What this figure illustrates is four main reflected paths (a,b,c,d) that can be extracted from a transmitted signal. Each path has its own unique delay and intensity along the transmission, with a histogram visualization of intensities grouped at the bottom of the figure. Although not shown, each path experienced random phase noise around a constant slope. As can be seen, the delay each path arrives at a different delay time, proportional to the distance traveled, and can have varied intensity, a product of the signals conflicting with each other as they propagate.

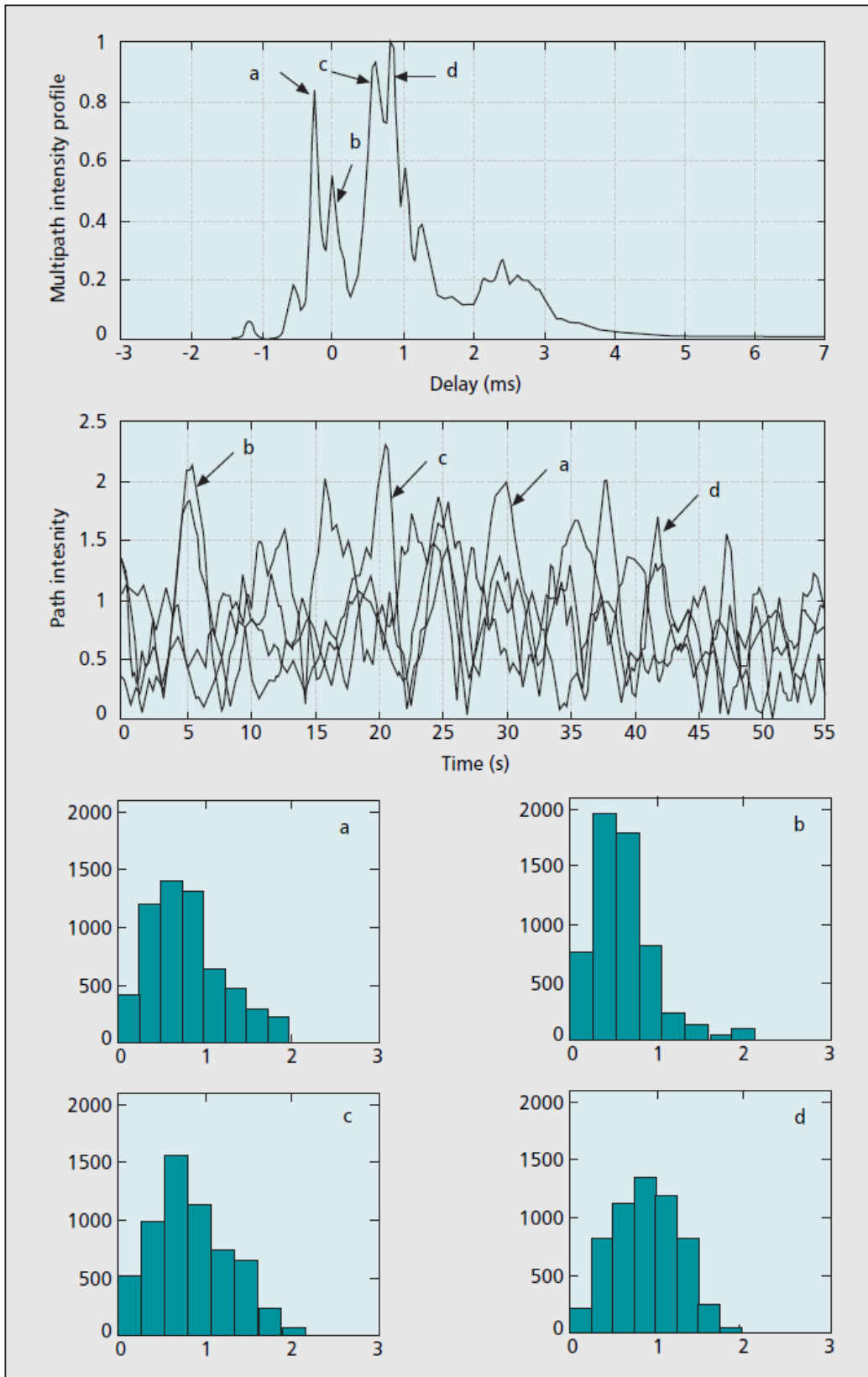


Figure 16: Multipath intensity profile, time variation of the amplitude and the corresponding intensities of arrivals a,b,c,d (Stojanovic & Preisig, 2009).

There are a few methods for mitigating multipath, of note for communication is using a linear frequency modulated (LFM) pulses to transmit data. This signal pattern provides a reliable reference to perform matched filtering against by creating frequency separation between the arrival time of the pulse and the arrival of multipath, as all reflected pulses must arrive behind the original. Successful implementation of an LFM pulse for localization was conducted in the work of Neasham in the development of the Seatrac USBL. This technology both enabled it to decode data more reliably as well as localize source of the signals transmitted, something that can only be accomplished with accurate phase information. As can be seen in Figure 17, even when traveling alongside the wall of a concrete pool, an environment prone to many reflections, an accurate tracking of the position of the receiver was achieved. However, as noted prior, this type of approach comes at the cost data throughput, with this link only capable of a 100 bit/s, a fifth of a prototype thruster link at 500 bit/s (Neasham & Sharphouse, 2015). This case is representative of many of the shallow environments proposed for the use cases for the system.

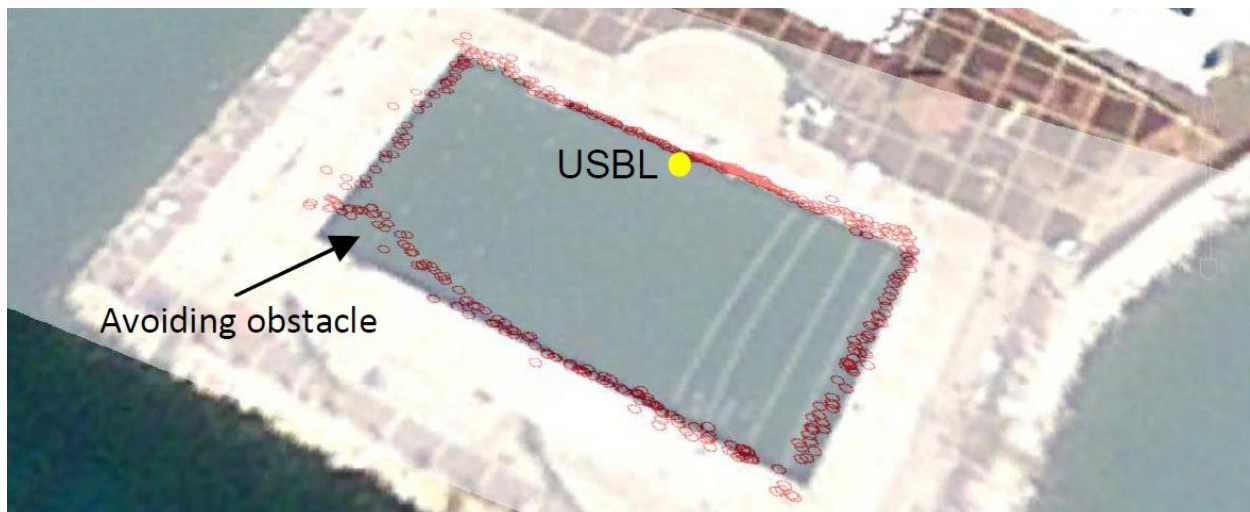


Figure 17: Seatrac USBL testing – concrete pool with a length of 50m (Neasham & Sharphouse, 2015).

## Doppler

Doppler shift is the variability of the frequency due to the speed of the source of the receiver transmitter, as well as the speed to sound in the medium. This relationship is described in Equation 5, where  $c$  is the speed of sound,  $v$  is velocity, and  $f$  is the frequency. In underwater communication, it should be noted that the potential for variability in the speed of sound as compared to the magnitude makes this a relevant parameter. In the work of Sharif, means to compensate for the impacts of this shift are discussed. The major method to compensate for doppler shift is the use of an ambiguity function. This will show a matched filter response to doppler shift variations. This involves searching the space of frequency shifts which can be reduced through being cognizant of the speed capabilities of the source and receiver. Robustness in Doppler shifting can be achieved through the knowledge of the transmission lengths of messages. Utilizing this a priori knowledge, a shift can be described over the message (Sharif, Neasham, Hinton, & Adams, 2000).

Equation 5: Doppler Shift

$$f_{received} = \left( \frac{c \pm v_{receiver}}{c \pm v_{source}} \right) * f_{transmitted}$$

This compensation approach is just a part of fully estimating the impact of Doppler shift. The speed of sound in sea water, is also dependent on the temperature, depth, and salinity. Equation 6 shows the Mackenzie model for estimating the speed of sound in salt water,  $c$ , where  $T$  is the temperature in degrees Celsius,  $S$  is the salinity in parts per thousand and  $D$  is the depth in meters (Mackenzie, 1981). Although an old model, it has held the test of time with newer methodologies yielding minimal accuracy improvements. To put this equation in perspective, a case at the water's surface will be considered with the full valid range of temperatures for this model, 2 to 30 degrees Celsius. A salinity of 25 parts per thousand is selected to maximize the speed difference. At the full range of temperatures, the speed of sound is 1457.73 and 1542.29 m/s at 2 and 30 degrees, respectively. Although such a temperature deviation is rather unlikely in practice, considering the worst case allows for a more complete assessment of the potential issues in the link that must be addressed.

Equation 6: Mackenzie calculation for speed of sound in sea water

$$c(D, S, T) = 1448.96 + 4.591T - 5.304 * 10^{-2}T^2 + 2.374 * 10^{-4}T^3 + 1.340(S - 35) \\ + 1.630 * 10^{-2}D + 1.675 * 10^{-7}D^2 - 1.025 * 10^{-2}T(S - 35) - 7.139 * 10^{-13}TD^3$$

In considering the impact of doppler in work, the worst-case in frequency shifting must be considered. A worst-case frequency shift occurs when the transmitter and receiver are traveling away from each other at maximum speed. Typical vehicle operations in this class have operational speed around 1.5 m/s. Using a speed of sound in water of 1500 m/s, the frequency shift is approximately 0.2% of the transmitted frequency. If we apply the two speed of sound values computed in the Mackenzie model, the frequency shift is approximately 6% transmission frequency. While far more substantial than using a fixed speed of sound, typical operations would experience far lower temperature shifts over the operational ranges proposed, dramatically reducing this impact. As such, the effects of doppler at this time will be consider negligible to account for in the link design.

### External Noise Sources

While many propagation effects directly impact the transmitted signal, there are ambient environmental factors that must also be accounted for. This is referring to any source of noise in the environment that is not produced from the data link itself. In communication terms, this noise would all be part of the noise floor, or the base noise present regardless of link decisions. Every environment will have unique noise sources; however, the typical behavior of noise sources is useful to consider. A characterization of Puget Sound looked at the average contributions of the present noise sources. Figure 18 shows the four discrete sources of noise identified in testing.

The ship in question is a ferry that traveled a route regularly across the sound. Quiet refers to natural physical process taking place in the environment, including tides, waves, etc. (Basett, Thomson, & Polagye, 2010) Analyzing the data the measurements appear to agree with what would be expected from attenuation across the frequency domain. The relationship does not always trend down in power, but the sources of noise in the environment are diverse and spikes simply correlate to frequencies being produced by the processes noted. In general, what this data shows is that external forces, vehicles, weather, and biology are all at least as impactful as the inherent noise of the sound. While some of these sources cannot be avoided, it can inform decisions about the link design. Selecting a frequency band outside of the primary ship frequencies, for instance, would provide better reliability in data transmission. In practice this could be implemented as simply as taking a few measurements of an environment before operations and selecting a link band, all the way to adaptive systems that react to these environment effects.

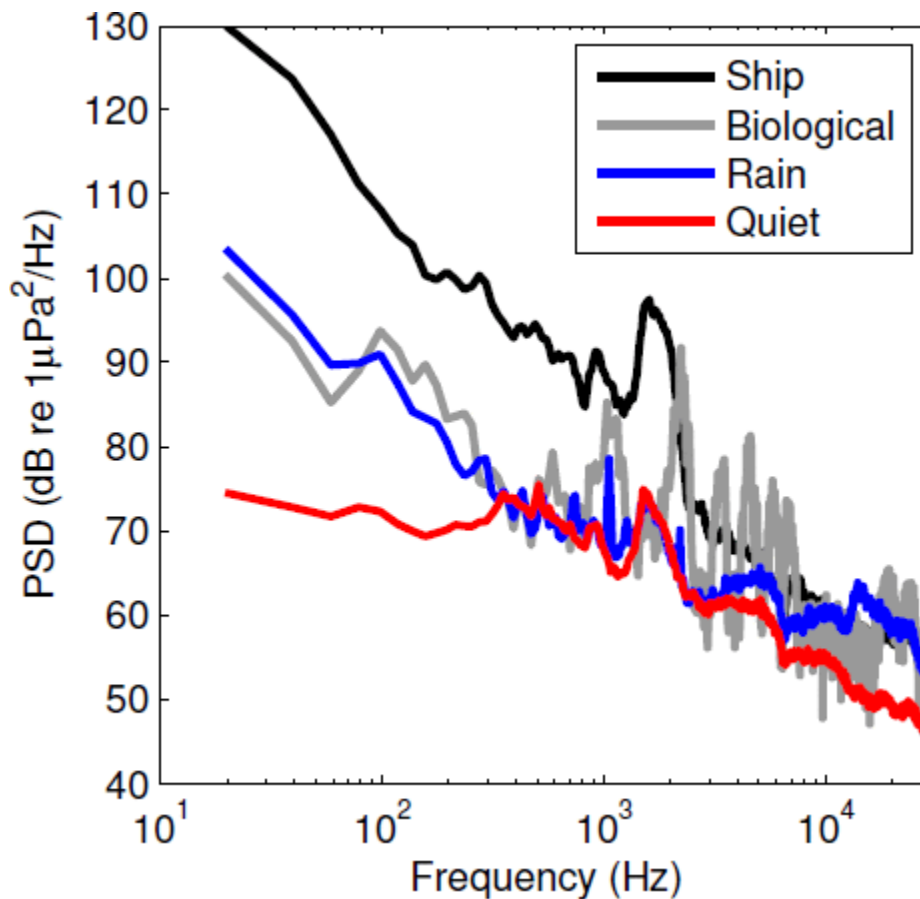


Figure 18: Acoustic spectrum of ambient sources in a waterway (Basett, Thomson, & Polagye, 2010).

## Fourier Transformation

In communication, it is often necessary to look both at the frequency and time domain and to move between the two. The conversion between the time domain and frequency domain is known as the Fourier transform. Equation 7 shows this transform, where  $x(t)$  is the signal being transmitted over time,  $j$  is the complex number,  $f$  is the frequency component, and  $t$  is time (Bracewell, 1986). What this transform describes is the notion that any signal in the time domain can be expressed as an infinite summation of sinusoids of differing frequencies. The practical application of this approach is in the ability to analyze the signal being received in a wireless link, which will be captured as a time series, and determining the frequencies that make up this transmission. For wireless communication, frequency modulation is a common approach to the modulation of data, and the ability to determine the frequencies present at a given time is necessary information for signal decoding.

*Equation 7: Fourier transform*

$$X(f) = \int_{-\infty}^{\infty} x(t)e^{-2\pi jft} dt$$

## Chapter 3: Communication System

Looking at the field of communication systems, typically the commercial sector has focused on longer range systems, with most targeting ranges of over a kilometer. While useful for many applications, there is a need for contributions to shorter ranges, less than 100 meters, while transmitting at bandwidths above 1 kBit/s (Sendra, Lloret, Jimenez, & Parra, 2016). In this environment, the size and class of vehicles that typically operate are generally underserved in the modem capability, both from a cost perspective and in consideration of the size and power additions that come from adding a communication system. To fill this need, a novel communication system is proposed, leveraging ambient noise produced by brushless electric thrusters.

The whole communication system is comprised of multiple hardware and software systems designed to complete the task of taking data from one system and transmitting it to another via acoustic signals. This section looks at the specific systems involved in this transmission. For clarity, the system as described consists of all hardware and software used to encode and transmit the data, and all hardware and software to receive and decode the transmitted data. In further sections, experiments involving case studies in the transmission of different types of data will be explored, but at the core is the transmission of data without distinction.

### ESC Hardware

The basis of the communication system is based around the VESC Open-Source Project. Specifically, the hardware used is an implementation of the VESC 4, shown in Figure 19. This ESC was selected because it was compatible with the thruster selected, discussed below, and the ease of modifying and deploying the firmware with the custom components that needed to be added. To operate a particular thruster, the ESC can be tuned for the specific motor and have all relevant parameters stored on the on-board EEPROM. What this means for the system overall is that this ESC solution is able to be implemented on a larger range of thrusters, as well as to be more easily integrated into an existing system by only changing this component. In operation, the VESC 4 has numerous IO options for control of the motor, making it easy to integrate into any specific system, such as USB, PWM, PPM, I2C, and CAN (Flipsky, 2021). Not only can these be used for control of the vehicle, but the firmware can be configured to leverage these interfaces for other processes. In the context of a modem, it means an interface could be used to directly access and transmit data from a sensor.

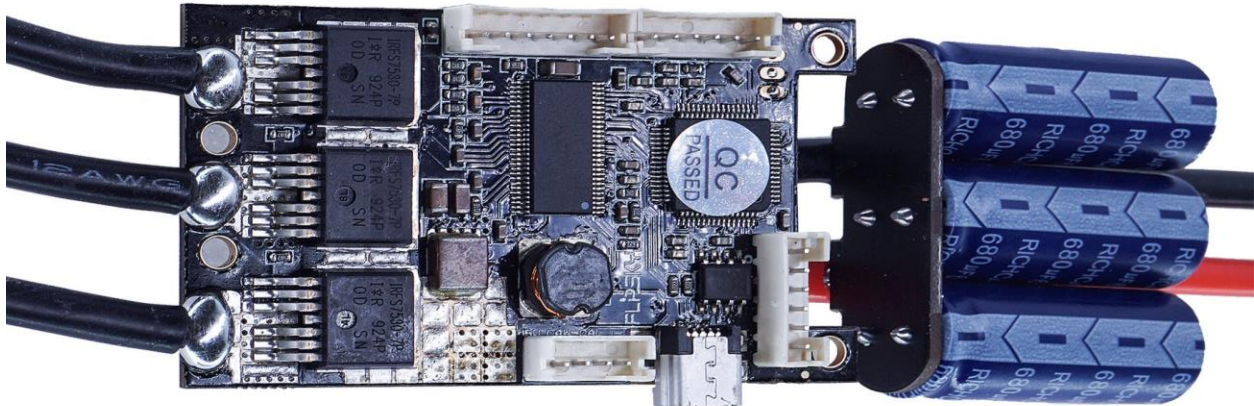


Figure 19: VESC 4 hardware (Flipsky, 2021).

### Data Transmission

Before considering the firmware implementation allowing for the transmission of data, it must establish how data is being transmitted. In terms of aspects of the ESC that can be controlled without impacting other aspects of its operation is in the control over the switching frequency of power delivered to the thruster. In terms of transmission, this means that frequency modulation (FM) approaches are what can be utilized. As firmware is controlling the transmission, this means that the modulation is inherently digital. The specific definition of the digital implementation of FM is Frequency Shift Keying (FSK). In particular, the general form of this approach shall be used, M-FSK, describing that a symbol can represent more than one bit value.

Transmitting via FSK means that every distinct symbol being transmitted has a distinct frequency associated with it. Data is modulated over time, with a specific symbol frequency being set for each symbol period. A symbol for reference refers to any distinct piece of information being represented on the data channel. This could be at its simplest two frequencies representing two states, 0 and 1 in binary for instance. However, more symbols can be used to represent more complex pieces of data, including multiple bits per symbol or certain much more sophisticated meanings if common or crucial to transmit. In the case of multiple bits per symbol, four symbols could be used for instance to represent two-bit binary numbers, 00, 01, 10, and 11. For our purposes, the ability to adjust the number of bits per symbol will be a configurable aspect of our data link as it will allow for experimentation in optimizing the link once understood through hardware characterization.

### ESC Firmware

Control of the motor is managed through the firmware running on the ESC (GitHub, 2021). This is executed from the on-board ARM processor. As the firmware is open-source, custom builds of



the firmware to be built and deployed onto the ESC. It is through this this process modifications can be made to add support for FSK transmission. For clarity, an overview of the system architecture is shown in Figure 20. The completed firmware solution focuses on two individual data links, that being the acquisition and queuing of data to send as well as the transmission through the thruster. The specifics of the firmware on communication fill the top row, beginning with the serial link. Here data to be transmitted is sent from an external device to an onboard data buffer. Pieces are pulled from this buffer and are used to set the switching frequency of the control loop. This controller, also taking in speed commands, is what delivers both thrust and data transmission from the motor.

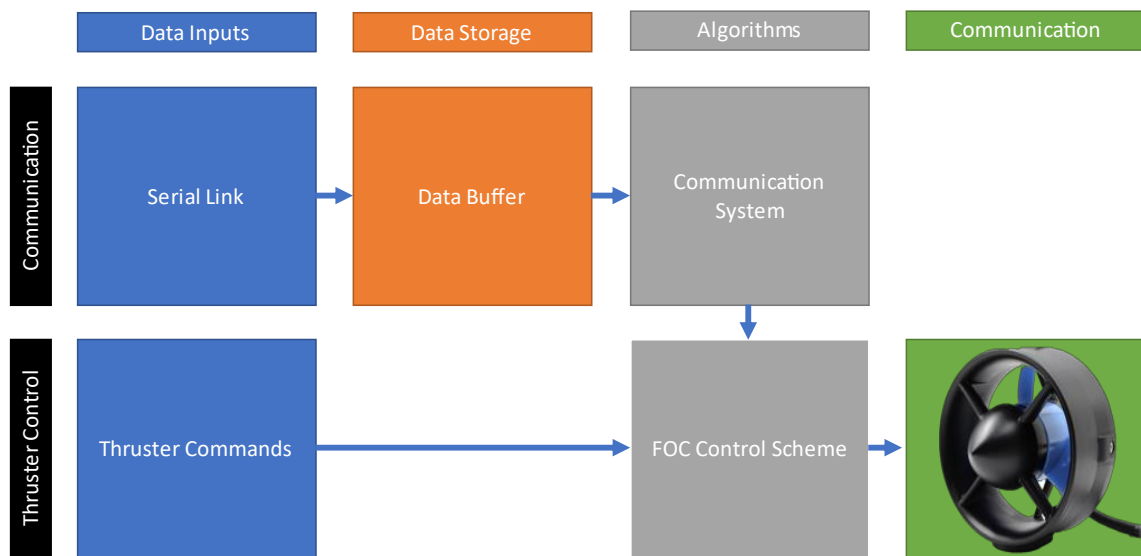


Figure 20: Communication System Architecture Overview

Transmission is accomplished by adding a routine to the FOC loop in the firmware to change the switching frequency used. The full code is cited in the references below, but for reference segments will be included here to discuss algorithms (Cronin & Romney, 2021). Figure 21 shows the code added to the FOC loop to change the frequency. This function is acquiring a time step from the on-board hardware timers and is determining whether or not a whole symbol period has occurred. If one has, it will determine the next frequency for the control loop. Of note, the timers being queried have an accuracy below one microsecond, or over a thousand times more than the typical symbol periods. The specifics of how this determination of whether or not a frequency change is required is shown in Figure 22. The prior state of the timer is tracked as the control loop operates on the change in time as opposed to an absolute time. If the change in time exceeds a symbol period, the next bit value is evaluated, and the timer has one period length subtracted. Back in the FOC loop, this updates the switching frequency if a change is needed by setting the proper register.

```

float nextFreq = FM_getNextFreq(dt);
static float lastFreq = FM_DEFAULT_FOC_FREQ;
if(nextFreq != lastFreq) {
    // If FM demands a new switching frequency, implement it.
    mcpwm_foc_set_frequency_on_the_fly(m_conf, nextFreq);
}
lastFreq = nextFreq;

```

Figure 21: Code segment, setting PWM frequency

```

float FM_getNextFreq(float dt) {
    static float tmr = 0;
    static float freq = FM_DEFAULT_FOC_FREQ;
    static int current_bit = -1;
    tmr += dt;
    if(tmr >= BIT_PERIOD) {
        tmr -= BIT_PERIOD;
        current_bit = FM_getNextBit();
    }
    freq = frequency_vals[current_bit + 1]; // accounts for the fact that null is -1;
    return freq;
}

```

Figure 22: Frequency switching routine

Managing the data to be transmitted is a buffer system that stores the data to be transmitted. The data buffer firmware is shown in Figure 23. As can be seen, both the location of where the buffer is being filled and emptied from are tracked continuously and updated with every access request. Communication with the ESC is done by a discrete thread taking in formatted messages on the serial link. These messages each have a unique ID and are passed through a CRC to ensure message integrity. Data to be transmitted over the link is sent to the ESC over its on specific control message, comprised of multiple 16-bit values and is stored in the buffer to queried from. This is for use in the actual message protocol, discussed later in this section. Enabling this data transmission on the firmware, custom messages were added to allow data transmission as well as controlling settings for transmission. Transmission settings include frequency limits, symbol rate, and number of bits per symbol. From these, symbols are spaced as to provided minimal interference with each other. A more detailed discussion on band allocation an inter symbol interference will take places in the optimization section. At a high level, however, interference is minimized by ensuring the main portion, approximately 90.3%, of a symbols power is allocated to its own portion of the frequency spectrum.

```

uint16_t fm_buffer[FM_BUFFER_SIZE];
unsigned int fm_buffer_level = 0;
unsigned int fm_buffer_ridx = 0;
unsigned int fm_buffer_widx = 0;
float frequency_vals[16] = { 22500, 20000, 25000 };
int MESSAGE_LENGTH = 8; //in symbols
float BIT_PERIOD = (1.0 / 1000.0);

bool add_byte(uint16_t b) {
    if (fm_buffer_level >= FM_BUFFER_SIZE) {
        return false;
    }
    fm_buffer[fm_buffer_widx++] = b;
    if (fm_buffer_widx >= FM_BUFFER_SIZE) {
        fm_buffer_widx = 0;
    }
    fm_buffer_level++;
    return true;
}

uint16_t FM_getNextByte(void) {
    if (fm_buffer_level > 0) {
        uint16_t c = fm_buffer[fm_buffer_ridx++];
        if (fm_buffer_ridx >= FM_BUFFER_SIZE) {
            fm_buffer_ridx = 0;
        }
        fm_buffer_level--;
        return c;
    }
    return -1;
}

```

Figure 23: Data buffer logic for data transmission

## Thruster Hardware

Although ESC hardware and firmware manages the encoding of data, ultimately the physical transmission of signals is accomplished by a thruster. For the purposes of our testing the BlueRobotics T200 Thruster, shown in Figure 24, was selected as a representative, commercially available propulsor in the class of vehicles looking to be used for this project. The thruster is brushless as is required for this technology to function. Data collected from the Robosub competition, an AUV competition on the size and range scale of the intended use case, sees an 86 percent utilization of BlueRobotics Thrusters of the 50 teams that were surveyed. While not the perfect representation of the marine market as a whole, it does indicate that the product can be successfully used on this class of sub. For reference, the Robosub competition limits vehicles to a size of 6' x 3' x 3' and with a maximum weight of 125 lbs in air.



Figure 24: BlueRobotics T200 Thruster (T200 Thruster, 2021).

The specifications of the thruster are included in Table 2. Spatially, this thruster is designed for vehicles with small vehicle footprints, while being able to produce a meaningful amount of thrust to propel them. The exact speed and performance expected from this thruster will vary accordingly with the vehicle it is mounted on, but vehicles using this system as the propulsion system operate typically within the 0.5-1.5 m/s range. At these speeds, vehicles can operate in waters that are not stationary, such as rivers, streams and surf zones. Although a single thruster is presented here, the system concept is independent of the particular motor and any can function for data transmission.

Table 2: BlueRobotics T200 Specifications (T200 Thruster, 2021).

<b>Parameter</b>	<b>Value</b>
Full Throttle FWD/REV Thrust @ Nominal (16 V)	5.25 / 4.1 kg f
Operating Voltage	7-20 volts
Full Throttle Current @ Nominal (16 V)	24 Amps
Diameter	100 mm
Length	113 mm

### Transmission Protocol

There are many protocols that can be implemented for a modem, with the best choice dependent upon many operational factors beyond the thruster and ESC. These include data formats being transmitted, error correction needs, and BER requirements. A more complete investigation of how to select a protocol and payload is conducted in the optimization section, however testing and validation of a system can be conducted on a large variety of protocols. For most of the

results that will be discussed in the experimental sections, a protocol of 1 Null symbol indicating the start of a message followed by an 8-symbol data payload will compromise a message, with the number of bits per symbol being adjustable. This protocol was not selected to be optimal in any particular type of data transmission, but rather to allow for ease in testing with base two sized datatypes.

Initial testing used pseudo-random values covering the full range of values in the data payload size. Covering the full range of values allows for a large variety of symbol patterns to be represented, ensuring that unique issues that may arise are considered. Testing first focused on 8-bit and 16-bit payloads as it allowed for ease of validation of performance in all cases, as well as in validating that the theoretical behavior of the modem was matching the tested results in all cases. It should be noted that the goal of this work is not to produce an optimal data link in a particular application, rather to validate the behavior of the thruster-based transmission. If proved to behave as expected, established literature optimizing data transmission of different data streams can be utilized.

### Receiver Hardware

Reception of signals beings the process of the other half of a wireless link, where the data transmitted is understood by another system. The first step in this process is taking the acoustic signals transmitted and converting them into analog voltage signals. These voltage signals can then be operated on through things like filters or amplifiers. These analog signals are ultimately converted to digital measurements that can be decoded. The hardware enabling the first step in this process is the physical hydrophone transducer, with converts the ambient sound into a differential voltage signal. For our experimentation, two different receiving solutions were used. The Teledyne TC-4013 was the first of which, shown in Figure 25. A detailed discussion of the hardware behavior of the sensor will take place when discussing characterizing the system, but at a high level this sensor provides omni-directional reception and a flat response curve throughout the frequency domain used by the motor. This means that the sensor can receive the acoustic signal regardless of sensor orientation or symbol frequency.



Figure 25: Teledyne TC-4013 hydrophone (Teledyne Marine, 2021).

The second hydrophone solution employed was the Sparton PHOD-1, shown in Figure 26. Unlike the TC-4013, this sensor has internal amplification of signals, with an internal amplification of 37 dB. This gain, approximately 70x, provides much higher signal strength for testing transmission at longer ranges. Of note, this gain is adaptive, meaning that it attempts to output a fixed amplitude signal, not to apply the maximum gain at all points in time. This allows for various signal strengths to be tested on the same system easily.



Figure 26: SPARTON PHOD-1 hydrophone (SPARTON, 2021).

When a hydrophone is used to listen for the transmitted data, it does not only acquire the useful data. As the signals received describe the entirety of the acoustic noise in the environment, it results in other sources of noise potentially dominating the received signal. This overpowering is known as clipping, and describes the amplitude limits of the sampling hardware, discussed in more detail further on in this section. Clipping, as shown in Figure 27, can make it impossible to separate frequency components, potentially making decoding of data not possible.

To demonstrate the impact of clipping, a visualization was constructed to demonstrate the impact it has on determining the correct frequency. What clipping results in is the inability to distinguish whether a given frequency is at its particular frequency or a harmonic. As Figure 28 shows, when a sinusoid is clipped at half of its amplitude,  $\pm 0.5$  in this case, a portion of the frequency response is shifted to the higher order harmonics. The implications of clipping mainly lie in the digital filter stage of decoding. Digital filtering relies on the filters shaped around the expected frequency allowing an individual symbol to be separated. When power is distributed elsewhere, this reduces the received power in this filter, and as such lessens the received SNR. In this example, no SNR is shown for clarity in the impact of clipping, however in practice there will always be some noise. A generalization of this relationship is shown in Figure 29, where the percentage of the signal's amplitude that was clipped was varied. The corresponding portion of

the frequency response relating to the actual frequency is plotted against this. In the case of a single frequency, this is a value of 1 in the case of no clipping, as it is the only frequency present. As every stage of the signal acquisition can have an impact on the accuracy of the decoding, taking consideration into each aspect that can reduce the strength of a symbol must be considered.

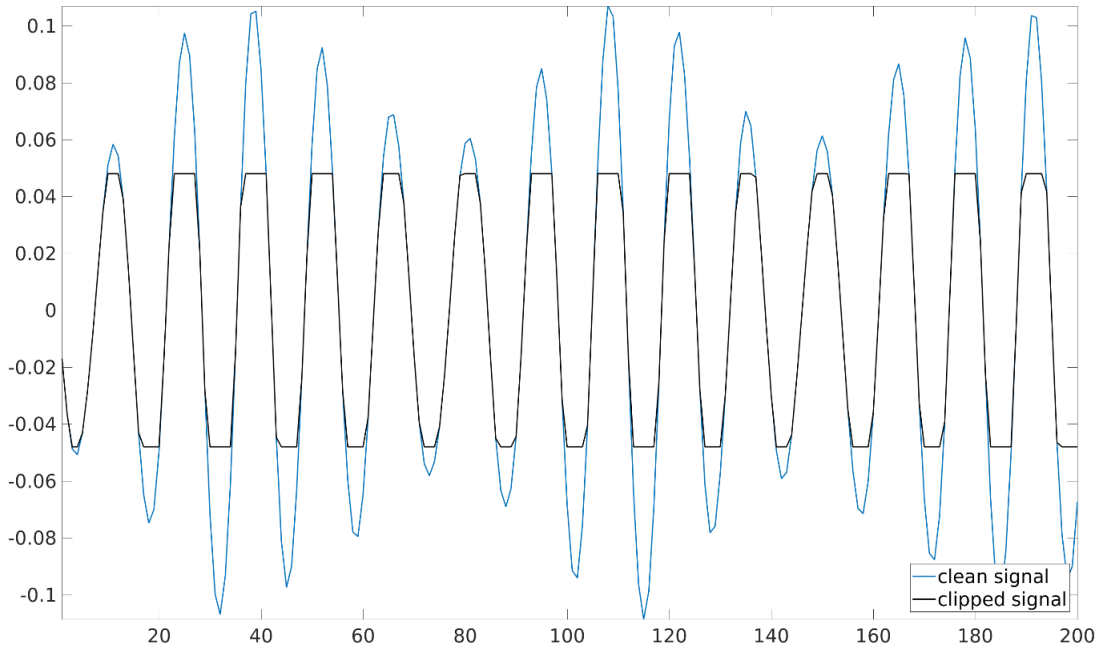


Figure 27: Signal clipping

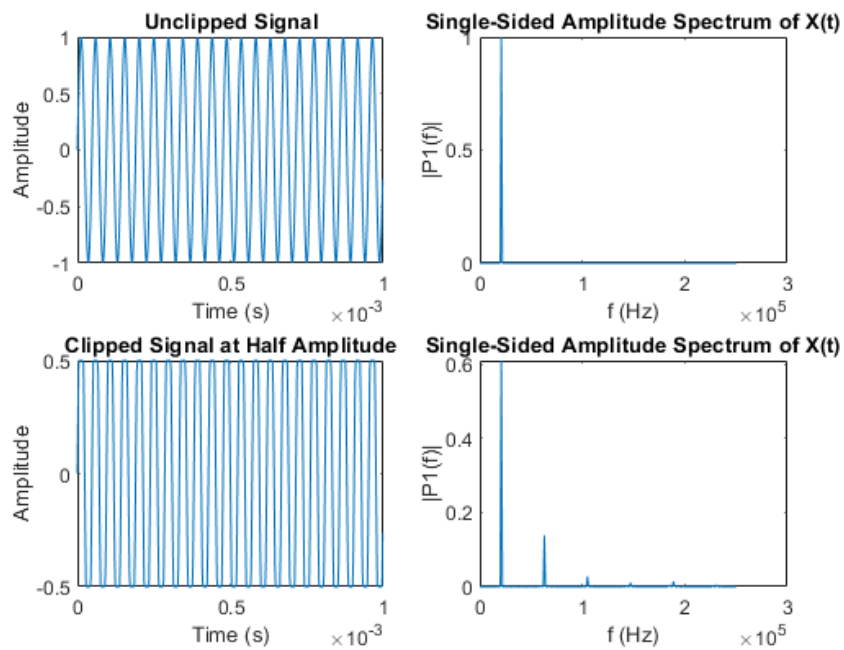


Figure 28: Signal clipping response analysis at half amplitude

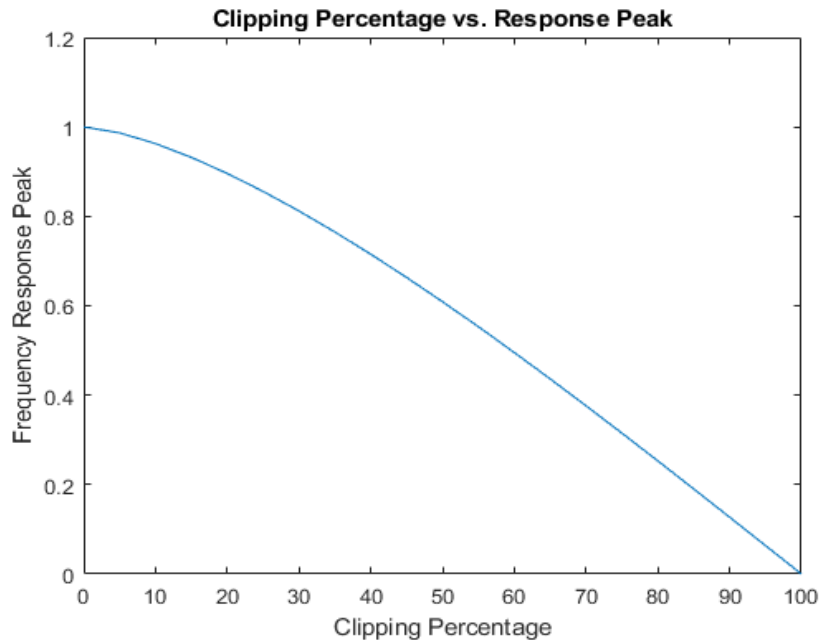


Figure 29: Clipping percentage vs. peak frequency spike amplitude

To mitigate clipping risk in the TC-4013, frequencies outside a band are removed with a combination of a high pass filter and a low pass filter. This filtering is done on a circuit, designed and constructed by a student to facilitate this work, shown in Figure 30, with each stage being passed through an OPA 134A and LTI 1739. What these integrated circuits (ICs) do in combination is to apply both a high and low pass filter on frequencies outside of the channel. This removes the risk of a loud external source dominating the received amplitude. Although the board shown below is fully populated for five hydrophone inputs, only one channel is needed for communication. In practice, multiple hydrophones being used for data reception would either improve decoding success through techniques such as voting schemes, or each channel could be optimized for different bands and as such different transmitters. For initial validation and characterization of the system, a single hydrophone will be used to isolate variables.

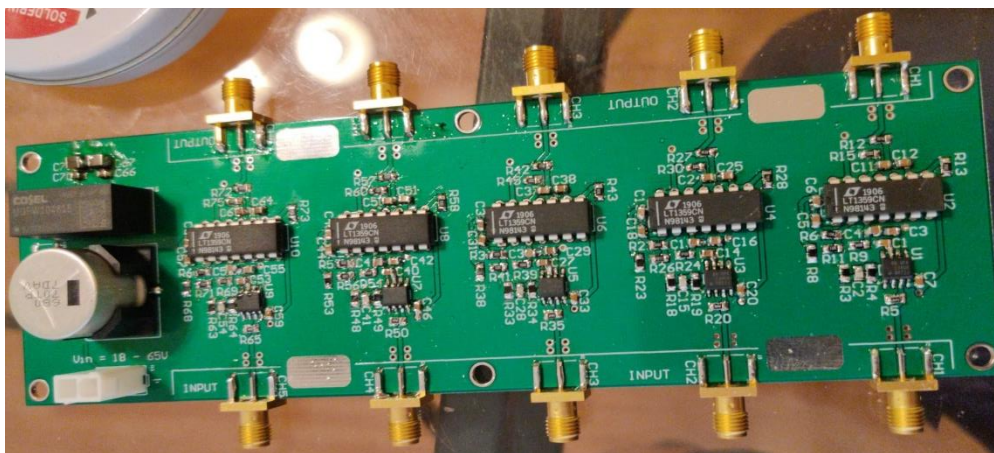


Figure 30: Analog filter circuit



At the end of the filtering process, the signal is passed through a low noise amplifier (LNA). This serves to take the bring the signal strength received and align it better to the voltage range of the data acquisition system (DAQ). The purpose of the DAQ is the conversion of the analog signals into a digital representation of data. This representation allows for digital signal processing to applied onto the signal ultimately resulting in a decoded signal. For testing, the NI-9222 DAQ, shown in Figure 31, was the selected device for this acquisition. A discussion on why this DAQ was used is held below and in following sections.



Figure 31: NI-9222 DAQ in an ethernet chassis (National Instruments, 2021).

Although discussions on amplitude and clipping have been had, it is not the only consideration in the selection of a DAQ. Other characteristics of NI-9222 made it a desirable option for this testing. Sampling rate, for instance is the speed at which a signal can be represented in time, as well as the frequency, as governed by the Nyquist criterion. On this DAQ, sampling takes place at 500,000 samples/s/channel (National Instruments, 2021). Considering Nyquist, in which sampling must take place at twice the maximum frequency to be resolved, there is more than enough of a sampling rate for the range of frequencies that motor can produce, up to approximately 37.5 kHz. However, in most cases, the established rule of thumb for data acquisition is 10 times the Nyquist criterion, something this sampling rate also achieves.

The other major consideration in a DAQ is the resolution of the voltage representation. When communicating wirelessly, signal strength can vary dramatically as a function of things such as distance or transmitter power, meaning that accurately voltage steps is needed to ensure a signal is correctly understood. The NI-9222 DAQ has a 16-bit resolution, meaning it can produce 65,536

distinct voltage levels over its input range. This input range is  $\pm 10$  volts, meaning that analog voltages can be represented in increments of just over 0.3 mV. This minimizes the impact of range for our tests, the shape of a signal can be accurately described. In a full solution with longer communications ranges, there are other approaches to ensure signals can be properly resolved, such as adaptive gains on received signals, such as is done on the Sparton Hydrophone. For this work, the focus was on proving the technology in a relatively short-range environment and the necessity of using an adaptive gain solution in all testing was deemed unnecessary.

## Decoding

The final step in the data link is the conversion of a digital symbol back into the original messages transmitted. This is accomplished through the use of a data decoding algorithm that is run on this acquired digital signal. The first step of this process is to receive the DAQ measurements on the devices processing the decoding. This is achieved in the case of the DAQ selected through a library capable of converting the ethernet packets measurements into usable data structures. The full measurement is a data structure, shown in Table 3, provides additional timing information alongside the voltage measurements. Of note here is that the resolution of the voltage value  $Y$  and of the DAQ are different because of the nature of variable precision floating point values. The use of a 64-bit floating-point number allows not only a 16-bit value to be correctly stored, but to account for the small adjustments the DAQ applies on measurements as a function of temperature. These corrections ensure correct representation of the signal, but due to the small nature cannot be correctly described without higher resolutions. From this data structure, a waveform at a particular received time can be visualized and have operations applied to it. Figure 32 shows this visualization for one hydrophone reception. Visually, it can be seen that the received signals are indeed of variable frequency, a high-level validation that data is being transmitted.

Table 3: DAQ measurement data structure

Component	Description	Data Type
t0	A timestamp representing the time at which the signal starts.	Int64 – seconds since epoch Uint64 – positive fractions of a second
dt	A double numeric that describes the difference in time in seconds between each sample in the signal.	Double
Y	A 1D array of doubles that contains the values of the samples of that signal.	Double

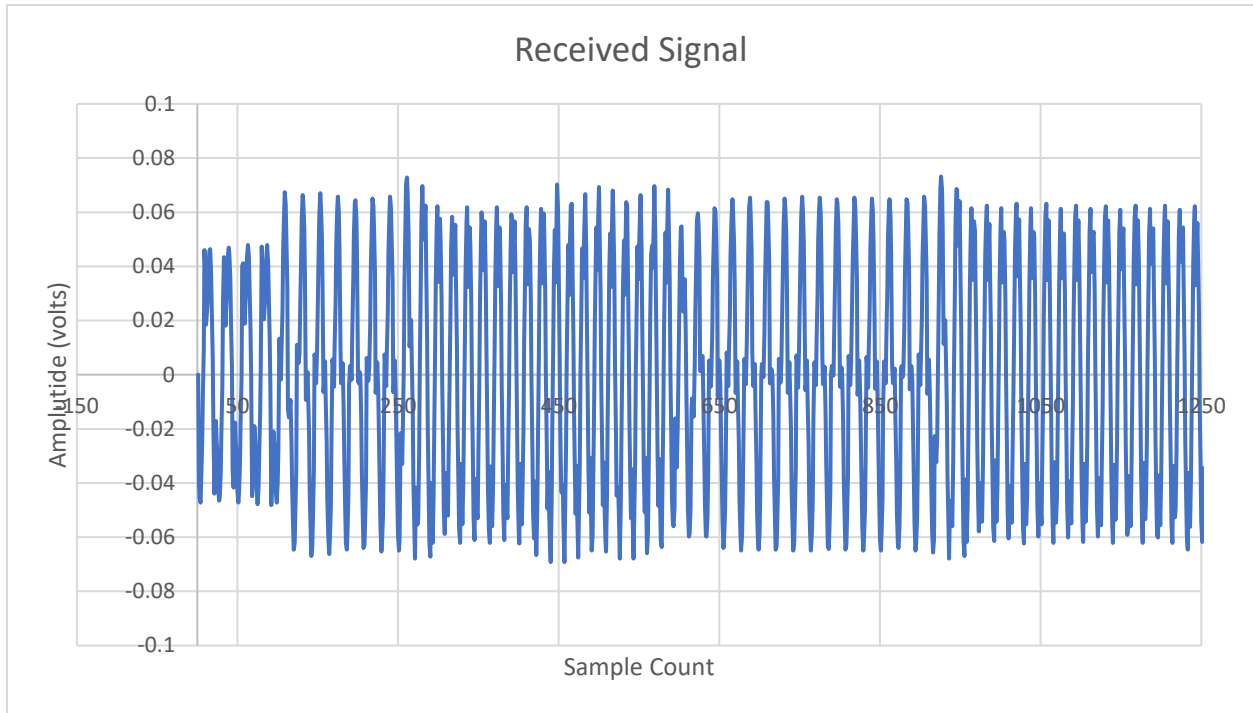


Figure 32: Single hydrophone received data - hardware filter applied

After signal acquisition, filters are constructed and applied around each of the symbol frequencies in the FSK scheme. Specifically, the waveform is first passed through a bandpass filter followed by a lowpass filter. Both filters are their respective versions of a Butterworth filter, with the high cutoff frequency at the symbol frequency plus the carrier rate and the low cutoff frequency at the symbol frequency minus the carrier rate. The filters differed in order, with a third order and a ninth order being used for the bandpass and lowpass, respectively. Filter order selection was done through experimental testing on increasing the order until the decoding error did not improve.

This filtering approach shows the proportional presence of each frequency over the recording time. To account for the slight variance in individual frequency responses, the results of these filters are scaled to the range of -1 to 1, giving a consistency in representation to all symbols. Figure 33 shows the results of these filters and scaling, and as can be seen individual messages become apparent even with visual inspection of the time series. Each color in the plot represents a different symbol specific frequency, shown plotted over time. In this case, the data was being transmitted with 2-bits per symbol as well as one Null frequency for indicating the start of a message. As can be seen, at any given point in time, all frequencies are present. This is due to noise effects discussed prior, namely multipath resulting in delayed paths arriving later. However, also as can be seen, there is a clear symbol dominant at each portion of time, indicating that decoding will work and that there is sufficient signal to noise ratio for accurate results.

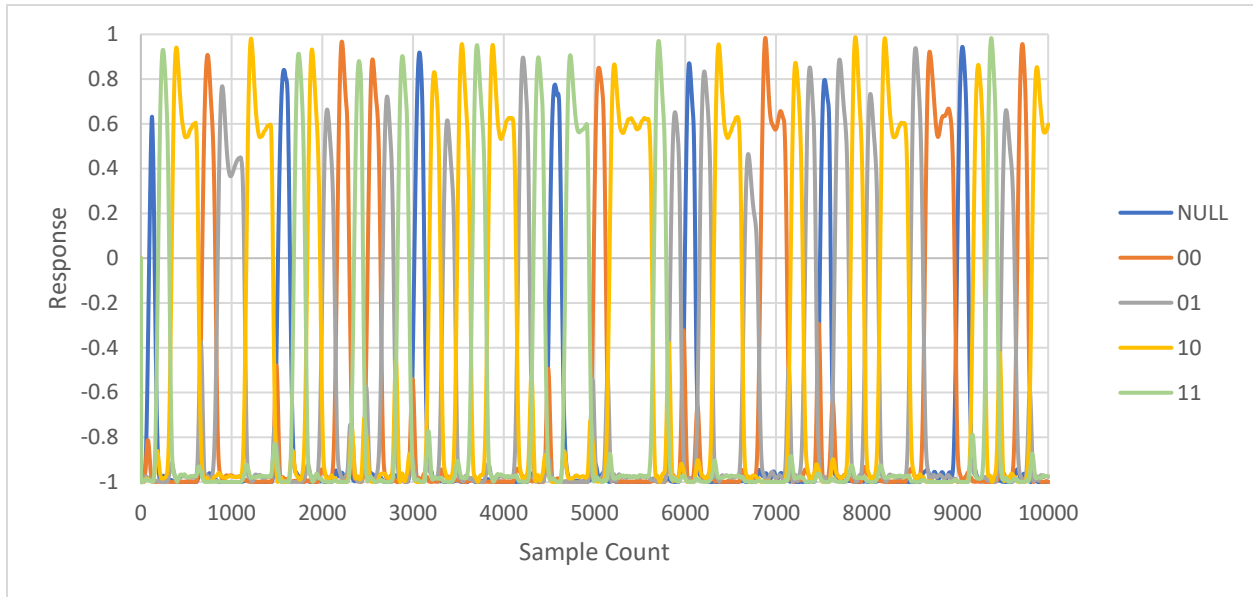


Figure 33: Response after decoder filter application

With the filters applied to the signal, the result can be converted into a N-value response by taking the strongest response between the symbols at each sampling time. This is done by taking the maximum response of the N signals at each time step and storing it as which signal had the maximum value at each time step. The result of this operation is shown in Figure 34, where each individual symbol is given a unique numerical value. In this case there are 5 symbols from our protocol, 1 Null and four data symbols, and they are listed from 0 to 4. As can be expected from the message structure, the Null frequency, index value 0 in this case, appears at a regular frequency of one symbol width with nine symbols in between. Data bits appear more randomly as the data being transmitted is variable and is reflected in their more varied occurrence, not being present in some messages and showing up multiple times in others.

At this juncture, extraction of individual messages from the overall data can be accomplished. First, only the null frequency is of interest and this plot is converted to a value of 1 for null and zero for anything else. A mask consisting of one null symbol followed by the length of the message and a secondary null symbol can be applied to the extracted symbol response, locating the presence of messages. The use of a null bit at the beginning and end of the message ensures that a full message will be extracted. Truncated messages will be handled later in the process. This mask is slid across the channel response yielding peaks correlating to full messages. Figure 35 shows an example of the result of the cross-correlation operation. A spike represents the presence of messages, and the separation between these spikes is approximately 4500 samples, what is expected with a message length of nine symbols and a symbol rate of 1000 symbols/s. To account for periods of time where no messages are being sent and only the null frequency is present, a filter on peak height as a function of a multiple of the standard deviation of the correlator response is used.

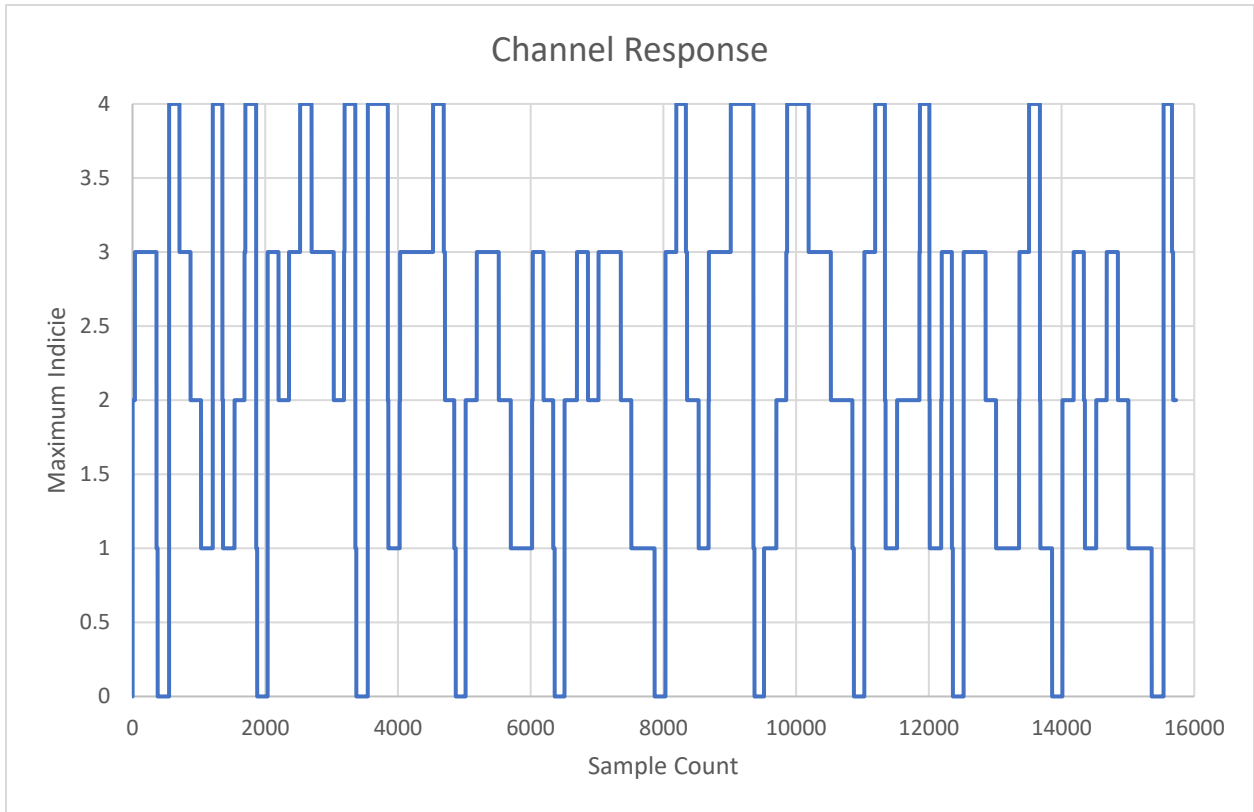


Figure 34: 5-Value representation of strongest symbol response

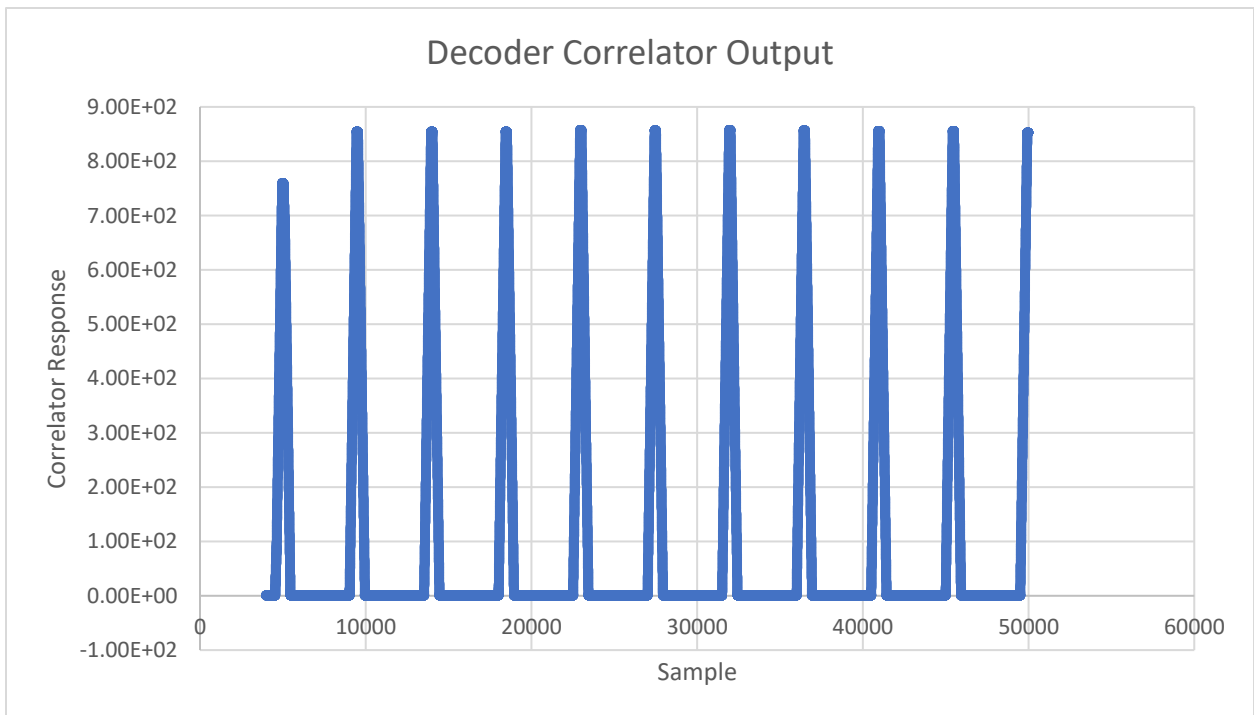


Figure 35: Decoder Correlator Output

This process results in the starting indices of messages being present. To ensure issues have not arisen in processing, further checks are made against the width between these indices. The width between these messages is considered against a known payload size to determine if a message is incorrectly detected. After messages have been detected within the signal, the remaining portion of signal is stored to be appended to the front of the next DAQ measurements. This accounts for the fact that messages can be partially sent within two measurements. Time correction to the second measurement is applied so the starting time is correct with added remaining portion.

With the start indices determined, the process now uses the data from the original N-value response plot. For each individual message, the data portion is evenly divided between the number of bits in the payload. For each of these regions, the mode of all response samples is taken, and a decision of the symbol value is made. The mode-based approach attempts to mitigate the impact of multipath, which can manifest as short duration impulses of noise on the response. With every bit value computed, the message can be constructed. At this juncture the accuracy of the messages received cannot be validated, a discussion about how this is accomplished will take place in the experimental testing section.

## Chapter 4: System Characterization

To properly understand the behavior of the thruster as a transmitter, a characterization of the system must be produced. This will describe the characteristics of the transmitter over the frequencies it can transmit, as well as its behavior at different operating speeds. From this, any unique operational characteristics that a thruster has compared to a discrete transducer will be identified and described. Beyond the specific insights yielded, the characterization will allow for the creation of a simulation describing the behavior of the system in operation, allowing for far more testing to be conducted on variables such as transmission protocol and decoding performance.

### Hardware Characterization

To be able to correctly characterize the motor itself, considerations about the other hardware in the system that would be used in this determination must be had. This section investigates all hardware components to be characterized, namely the thruster, as well as the supporting hardware, filter circuitry and hydrophones, that could impact the description. When the supporting hardware has been described, it will allow for the characteristics of the motor to be uniquely separated.

### Receiver Characterization

Up until this point, our theoretical prediction of the behavior treated the thruster as an ideal transducer. An ideal transducer is a theoretical source that can produce equal powered frequencies throughout its entire operating spectrum. This assumption is disconnected from the actual nature of transducers. Even purpose-built transmitters suffer from the inability to consistently produce all frequencies at the same power. Figure 36 shows the transmission sensitivity of a Teledyne TC1026 sensor, a purpose-built acoustic transmitter, similar to a thruster as it shares an omnidirectional transmission pattern and a similar frequency band to the T200 motor (Teledyne Marine, 2021). As can be seen throughout the frequency band, there is a maximum power difference of 14 dB. This power difference directly relates to the SNR, as transmission will have a base noise floor to overcome, and as such will impact the ability to transmit error-free messages.

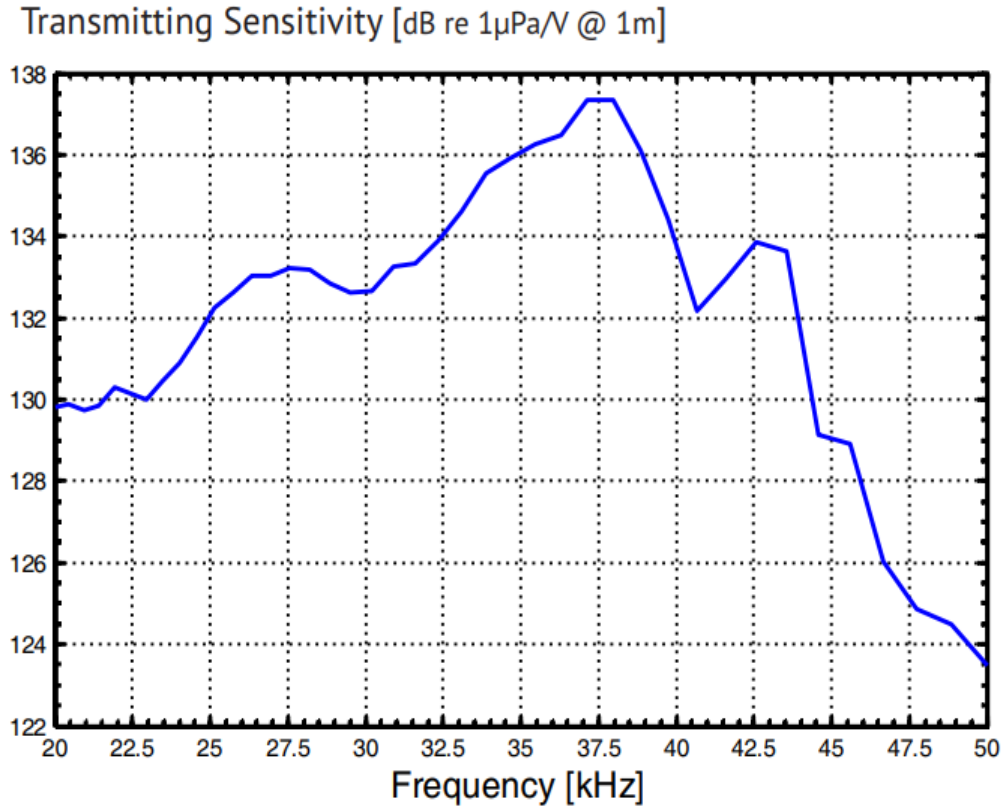


Figure 36: Teledyne TC1026 frequency response (Teledyne Marine, 2021).

To characterize the motor, the contribution of the received signal from all other sources of frequency attenuation must be determined. The factors to be isolated include analog filter circuits, range-based attenuation and the hydrophones receiving the signal. Each factor must be characterized or addressed individually, as a direct measurement of the response of the signal is not possible.

Starting with the first stage of a received signal, the hydrophone response is accounted for by leveraging the calibration information provided by the manufacturer. Currently our facilities are incapable of calibrating the sensors ourselves, and as such the manufacturer provided data must be trusted. The two main factors in consideration of the sensor are the directivity response, and the frequency response, which in our band of interest, 20-30 kHz. This band selection process will be shown later on and is derived from a physical upper limit from the hardware, and desire to have more signal phases available in the received signals on the low end. Figure 37 shows the characteristics of the sensor. In terms of directivity, is approximately omnidirectional in the horizontal direction, meaning that the rotation of the sensor is not crucial to be in a fixed position for testing. The vertical directivity does vary, and the sensor will be mounted as consistently vertical to account for this. The frequency response of the hydrophone has a variation of roughly 3 dB in the band of interest, which has the potential to be impactful on the signal. Further testing



of the other components will determine if it is dominant in the response or if other aspects of the system overwhelm its impact. Of note here, this directivity measurement data was at a higher frequency than is expected to be used for transmissions, 100 kHz, however this data shows the mechanical properties of the sensor rather than the exact directivity response at all the frequencies intend to be used. The uniform nature of the directivity indicates that the materials surrounding the transducer as well as the transducer itself are free from manufacturing defects that would impede this. All sensors used in testing were calibrated by the manufacturer and had response values comparable to this reference example.

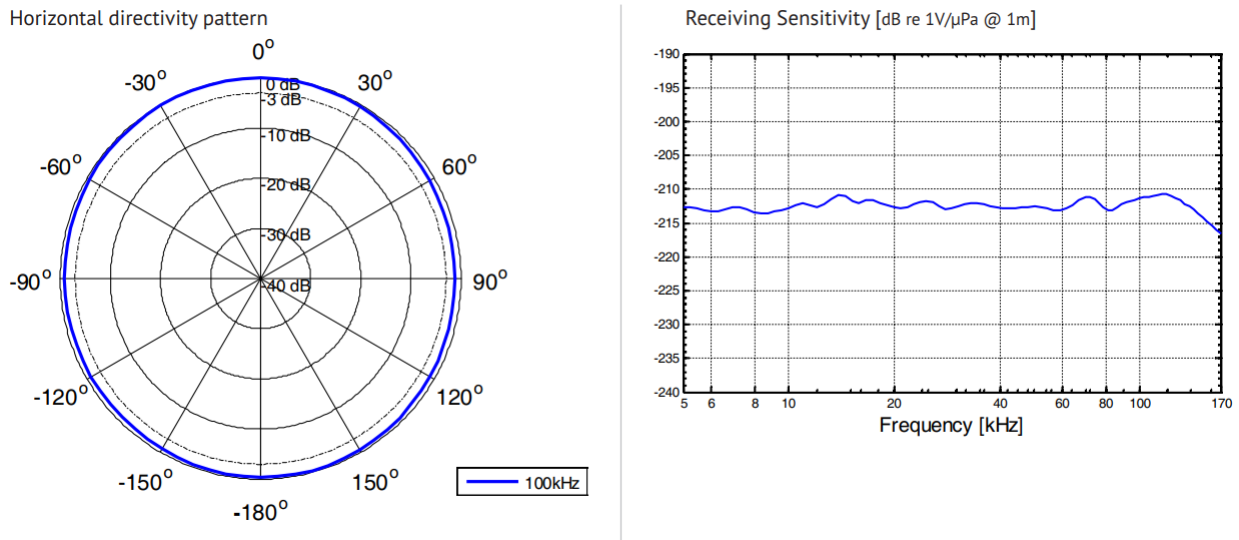


Figure 37: Teledyne TC4013 directivity response (left) and frequency response (right) (Teledyne Marine, 2021).

The next step of the processing process is an analog filter layer. It is comprised of three stages, a high pass filter for frequencies above 20kHz, a low pass filter for frequencies below 50kHz and a non-inverting amplifier stage for better aligning the output to the input range of the DAQ. All these circuits are fixed filters with high tolerance components used, and as such effects such as thermal variability will not be considered at this time. If any evidence of the need occurs, it will be further investigated. To characterize this stage of the process, a signal generator is used to produce reference sinusoids throughout the frequency band. This signal is simultaneously routed through the filter circuit into the DAQ as well as directly into the DAQ. This allows for a direct comparison of the signal to be achieved, alongside any relevant sources of noise to be considered. This setup also allows for individual verification of the function generator. The test setup for this testing is shown below in Figure 38. Of note, a direct BNC to BNC cable connection between the function generator and the box containing the filtering circuitry and DAQ. In operation with hydrophones, there sensor would be plugged into one of the other connectors shown on the box, that adapts it to BNC. While this does mean that there is a slight difference on the connections, all connections are rated for the frequency range used and as such there is no evidence this would impact the characterization.



Figure 38: Hardware system characterization test setup

Testing involves slowly stepping through the frequency band. The function generator itself uses analog inputs to set frequency values, so the reference signal in the DAQ is used to verify the transmitted frequency. To test, the analog dial was slowly rotated throughout the frequency range, with slight frequency increases followed by a pause of approximately 30 seconds. This process was continued throughout the full frequency range tested. Once sampled, the recorded signals are passed through a short-time Fourier Transform (SFTF) spectrogram. With this, the dominant frequency can be determined at each individual time step, alongside its magnitude. For reference, a time length of 64 samples was used with a 75% resulting in a measurement every 64 microseconds. Frequency measurements were placed into 8192 bins, or approximately 61 Hz ranges per bin. These parameters were selected to provide accurate representation of the input signal. Results of channel attenuation are shown below in Figure 39. From this testing, it appears that the response is behaving as expected. Of note, hardware solution will not produce a perfectly flat response over a frequency range. The variance within the frequency band is within a range of approximately 2 dB, and can be predicably described, which allows it to be properly accounted for.

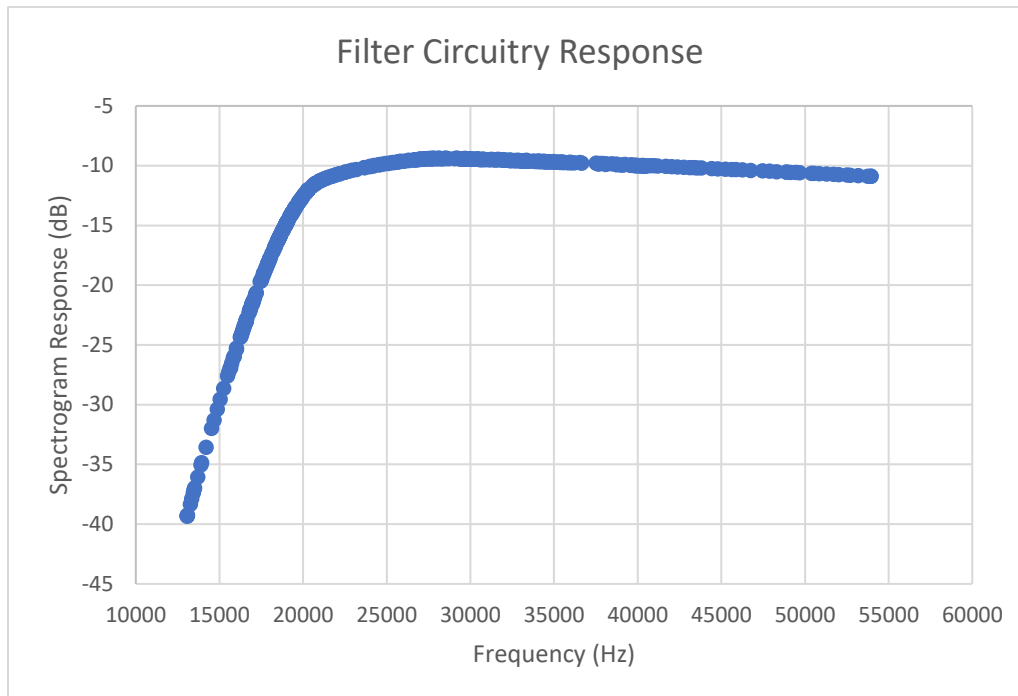


Figure 39: Hardware filter response throughout frequency spectrum

### Thruster Response

The unique aspect of a thruster as compared to a traditional transducer is the ability to produce propulsive forces. As such, a core part of characterizing the thrusters will be determining the impact that various duty cycles have on the transmission. To validate the behavior, peak-to-peak voltage of the received signal was compared over various duty cycles. A maximum speed of 20% in either direction was what was possible while mounting the thruster statically at a sufficient depth. This is needed for a correct comparison of duty cycles; motion could influence measurements. To address the risk of attenuation from biasing the measurement, a single continuous frequency tone was used, in this case 21 kHz. In the cases of a single frequency isolated in its environment, the peak-to-peak voltage would correlate with the signal to noise ratio of the transmission. This comparison can be more useful than SNR which is difficult to calculate in environments where multipath is the dominant noise, as it is the signal itself generating the noise. While peak to peak voltage would also be impacted by multipath, using small time periods and averaging the peak-to-peak voltages ( $V_{pp}$ ) over a longer recording will mitigate the impact of multipath, as it results in both and increases and decreases in signal strength from the conflict.

This test was run both on the Sparton and Teledyne hydrophone solutions, in each case at a range of one meter. Testing was conducted at the universities pool with static mounts for both the hydrophones and thruster at a depth of one meter. Each mount was suspended away from the wall to prevent a secondary transmission path. While this testing approach does not manage to eliminate the impact of multipath, the amplitude noise produced by it does behave as random noise when so many reflectors are present. This means that by averaging the result over a longer

period the impact of the noise will tend towards zero. Each test case was transmitted for approximately five minutes each to ensure sufficient data was collected.

What is expected from evaluating both cases are that the amplitude behavior will be the same, but the exact amplitudes will be different, as each system has a different amplification. Figure 40 and Figure 41 show the results of these tests on the Sparton and Teledyne hydrophones, respectively. As can be seen, there is some variability at various speeds but there is no distinct relationship between the speed and received signal power. This result furthers the ideal that the system is behaving in the same manner as a traditional transducer, meaning that subsequent analysis on it can use the same methodologies.

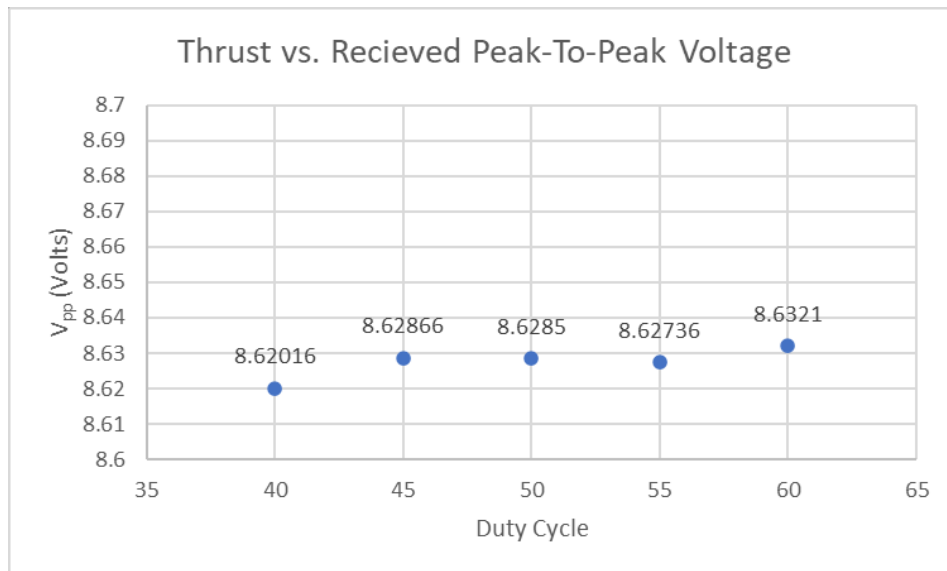


Figure 40: 1m range voltage test, Sparton PHOD-1

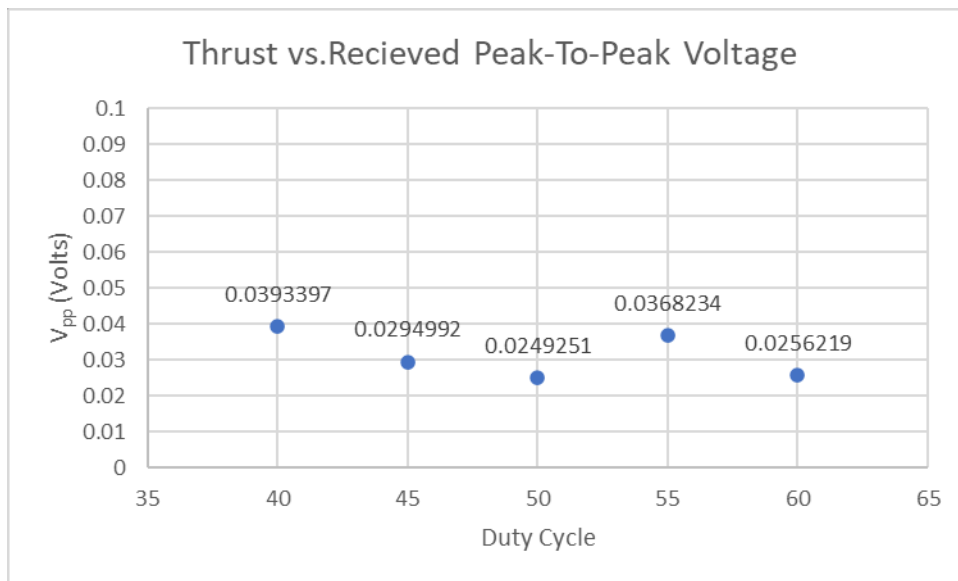


Figure 41: 1m range test, Teledyne TC-4013

## Frequency Domain Analysis

The Fourier Transform, Equation 7, tells us that the modulation of data in the time domain will have an impact in the frequency domain response. As time and frequency are related, the impact of modulation will be dependent on multiple factors, including transmission rate, message protocol, and the frequencies used in modulation. To validate the transmission behavior of the thruster is as predicted, a simulated symbol will first be used to create the basis of comparing frequency responses to an of the thruster in the field.

First the impact of modulation without the specific symbol frequencies will be considered. This creates a pattern of modulated symbols impacted only by the symbol rate and protocol. The protocol being used for this analysis has a Null symbol value indicating a message followed by eight data symbols and is modulated at a symbol rate of 500 symbols/s. From these communication parameters, the frequency response on the Null symbol can be described, shown in Figure 42. Of note, until stated the results shown are simulated responses for the purpose of demonstrating the response. The major characteristic of this response is that the power is not focused on an individual frequency or spread out among a range, it is concentrated in spikes at discrete frequencies. From the protocol and data rate, the Null symbol is being transmitted 1/9<sup>th</sup> of the time. This duty cycle describes how the spikes are separated. The general form of what is being transmitted is a pulse train. Applying the Fourier transformation to this will describe the pattern of the spikes. This is shown in Equation 8, where  $n$  is the Fourier component number, and  $d$  is the duty cycle, in this case 1/9. The frequency spikes occur at multiples of the Null symbol frequency, 500/9 or 55.56 Hz in all cases where  $n$  is not a multiple of nine. As the transform would indicate, the spacing between these frequencies where spikes to not occur is at a spacing of 500 Hz, the symbol rate. Between these gaps, 8 spikes would be expected, with filling the remaining portion of the band.

*Equation 8: Fourier transform of the pulse train*

$$\mathcal{F} = d * \frac{\sin(\pi nd)}{\pi nd} = d * \text{sinc}(\pi nd)$$

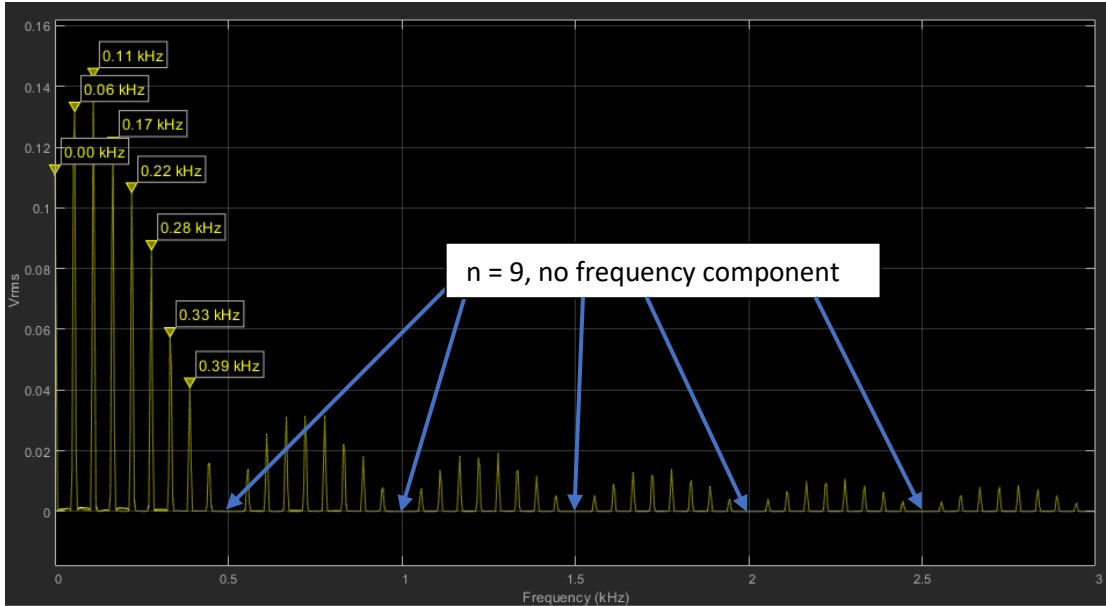


Figure 42: Null symbol frequency response

This consideration of a symbol does not account for the effect of the symbol frequency. If this Null symbol was represented with a 20 kHz signal, the frequency response will be the product of the two, shifting the response of Figure 42 to be centered about 20 kHz. Figure 43 shows the result of this transmission. The center of the frequency response is shifted to be about 20 kHz, but now both harmonics above and below this center frequency can be seen. It is still the case that in either direction of this center frequency, there are eight spikes before the first Fourier component number is a multiple of nine. In either direction, the spacing between these spikes is still 55.56 Hz, as this is a function of the protocol and not the transmission frequency.

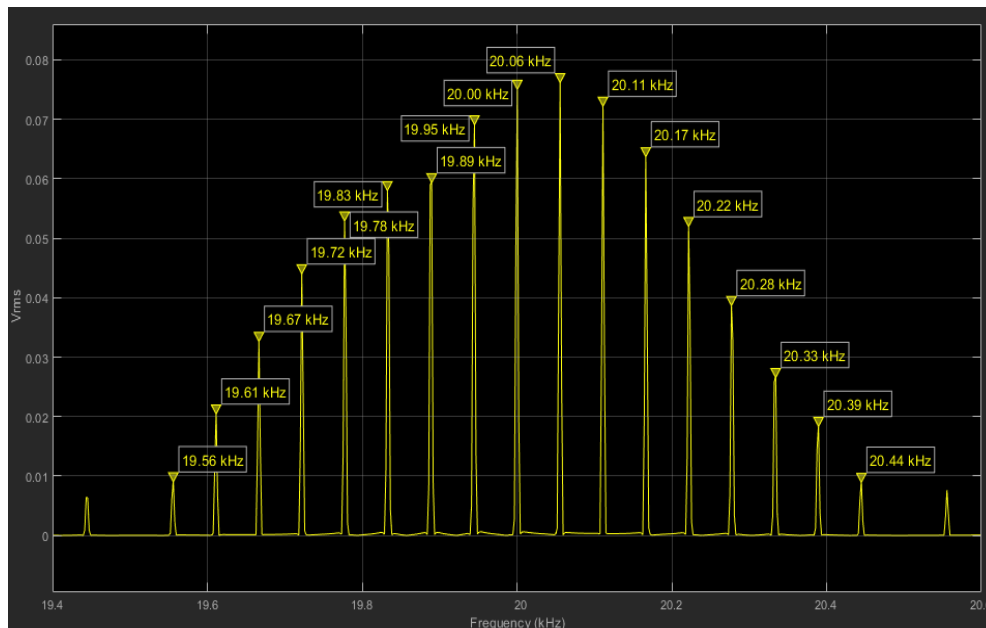


Figure 43: Symbol response with transmission frequency applied

Beyond the Null symbol, the frequency response of a data symbol follows a similar behavior, albeit with a different distribution of spikes amplitude. Figure 44 shows a symbol transmitted at 25 kHz. Of note here, the components of the response are still separated by the spacing (25 kHz)  $\pm n \cdot 55.56$  Hz. The variability in the amplitude comes from more complex duty cycle, with an individual message having the variability of 0/9 to 8/9 symbols being present.

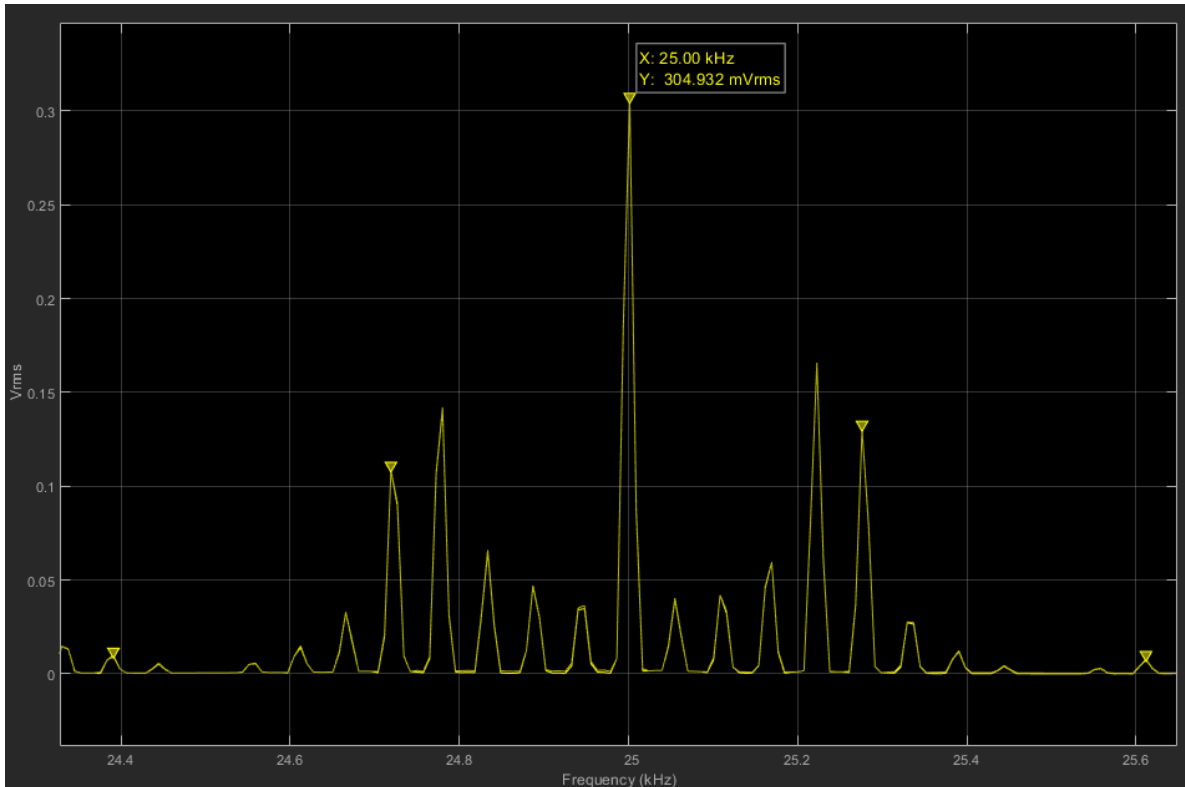


Figure 44: Symbol response of transmitted data bit

Extending this transmission to a sample using all three symbols, the behavior of the full spectrum can be visualized, with a Null symbol, zero bit and one bit at 20, 25, and 30 kHz, respectively. From Figure 45, the spreading of the harmonics throughout the frequency band can be better seen. Each symbol primarily occupies a space equal to twice the symbol rate of the link. This range for each symbol can be used to determine the point at which symbols would begin to have a large impact on each other, a full discussion on which will take place in the optimization section. From the symbol separation of 5 kHz, the maximum symbol rate would be half of this, or 2500 symbols/s. At this symbol rate, the first frequency component that has zero response on each symbol is the same value. Figure 46 shows a visualization of this.

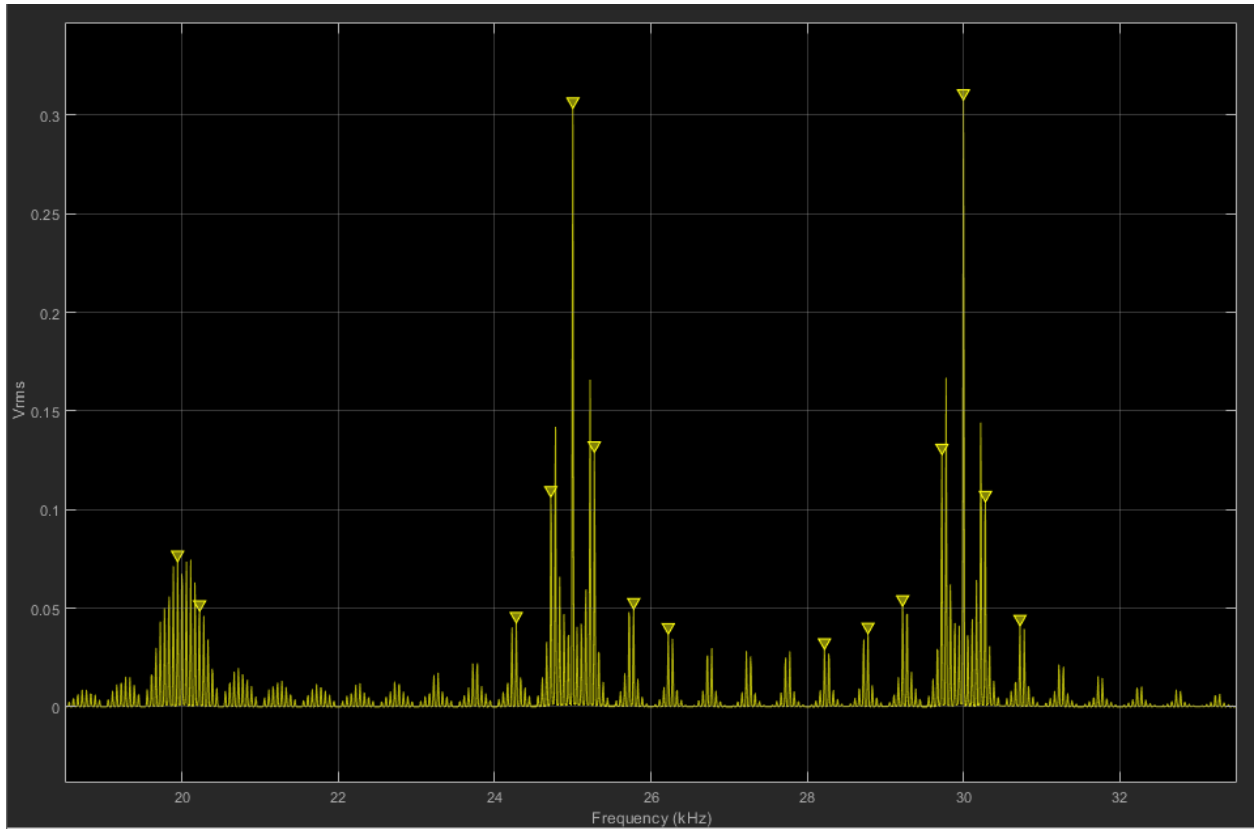


Figure 45: Frequency response of a complete message transmission

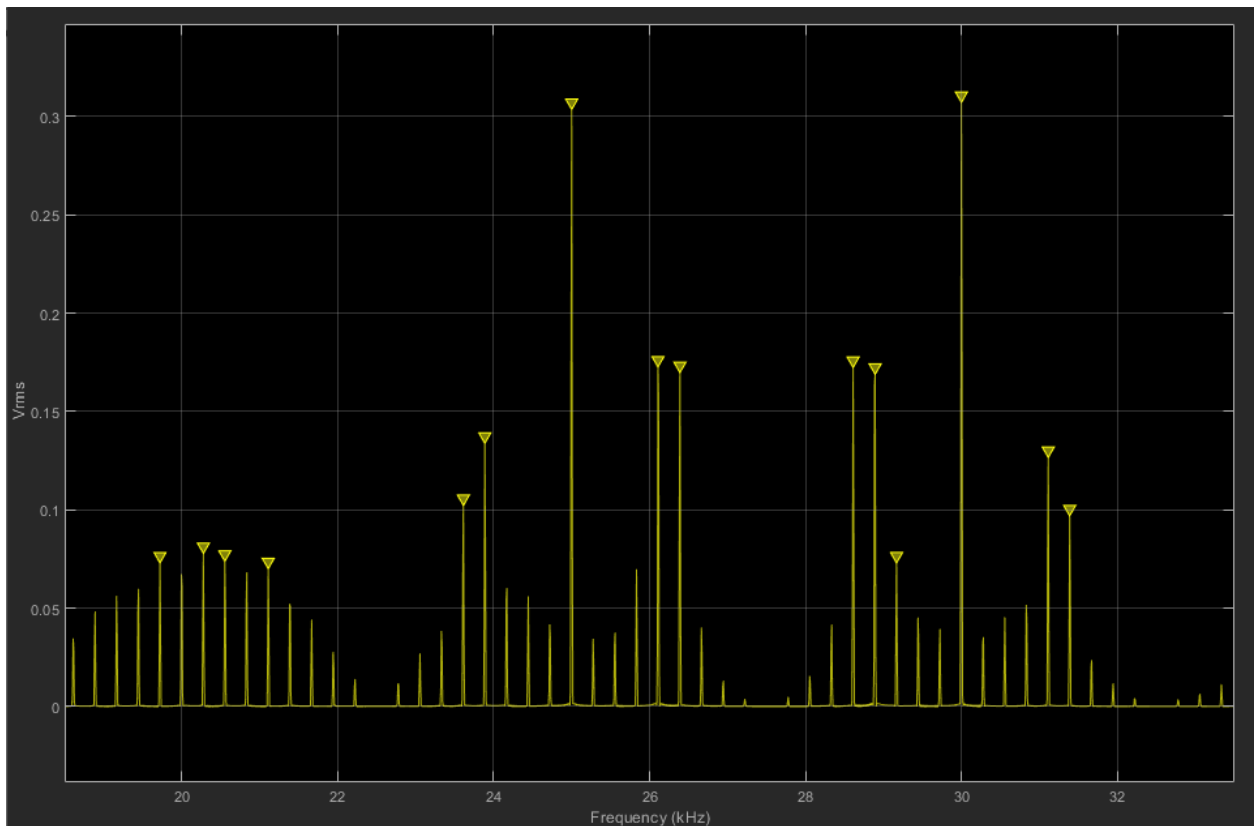


Figure 46: Frequency response with frequency component gaps aligned



To determine whether the theoretical behavior of the response is what is being produced by the thruster, recorded signals from field tests will be compared against. To provide a theoretical reference, a reference signal of three frequencies was generated with frequencies at 20, 25 and 30 kHz, respectively referring to zero, null and one bit. The message transmitted was a null, followed by the message 10101010. The symbol rate for transmission was 500 Hz. Figure 47 shows this response, with the distributions are centralized around each the symbol frequencies, with a width of twice the symbol rate to the first null. Some reference spikes have been labeled, but in a more detailed analysis, the separation of the response spikes throughout the band is following the expected separation of 55.56 Hz. Considering the harmonics, a distribution about each of the symbol frequencies with a null separation the same width as the transmission baud would be expected. This is not explicitly the case, as reflections in the environment mean induce a constant noise in the band of interest. There are proportionally significant gaps in the response at the frequencies expected however, indicating that the transmission is as expected.

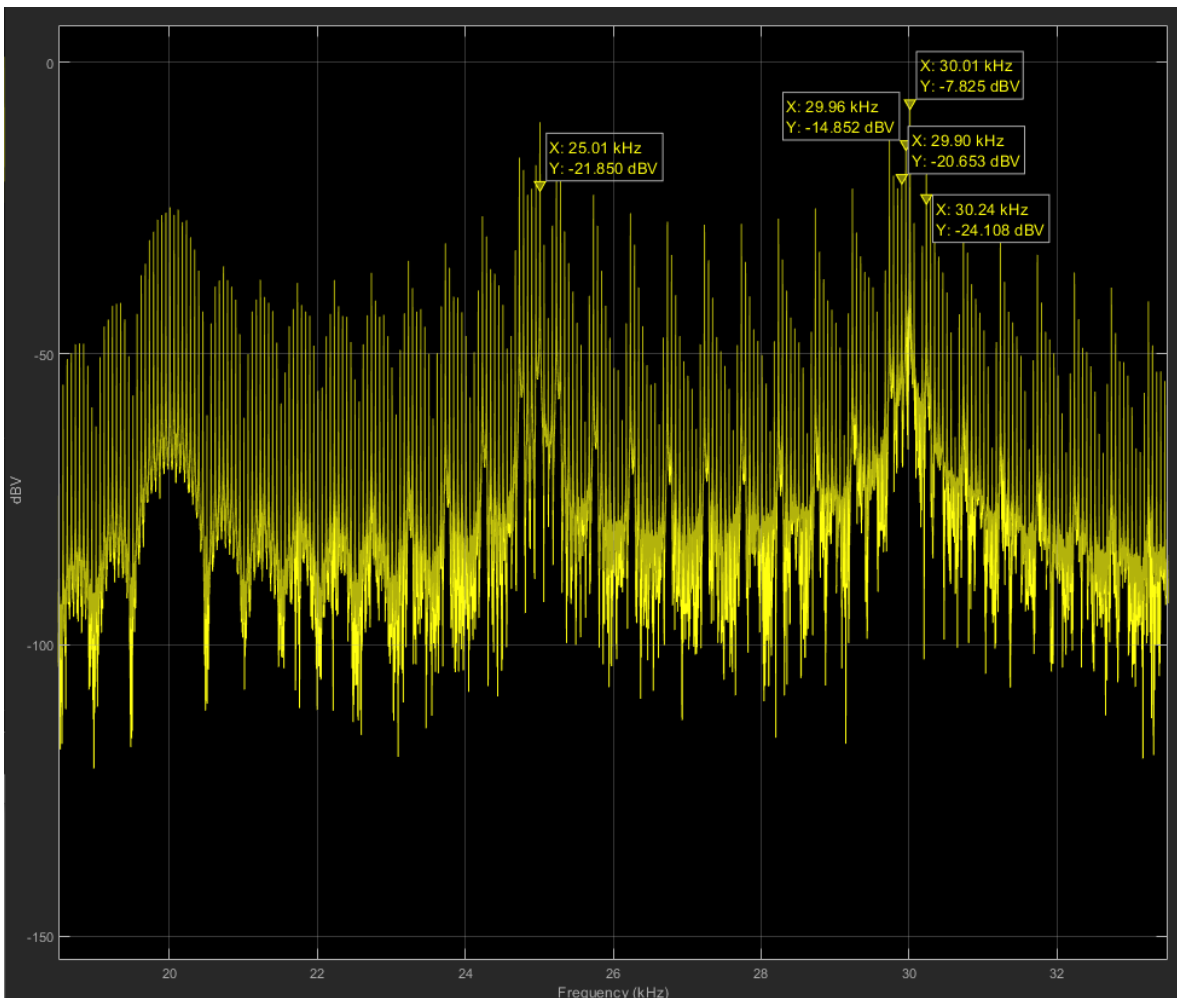


Figure 47: Real-world band response

Another insight that can be taken away from Figure 47 is the distribution of power in transmission. Both of the data symbols, 25 and 30 kHz, have significantly more power in the spectrum than the null symbol, 20 kHz. As each data bit is present four times the amount as the null symbol, this is the expected result and further aids in confirming the understanding of the thruster operation. Also of note is the fact that the strength of the spectrum is not as symmetrical as in the theoretical cases. This is both a property of environmental effects and of data patterns used, and variability is expected in data recorded in the field.

#### Thruster Characterization

With the other portions of the system characterized, the behavior of the thruster can be isolated. To test this, individual frequency tones were produced by the thruster and recorded. Testing was conducted at the same test site as the experimental testing and will be discussed in more detail in that section. The only difference was the separation of transmitter and receiver was reduced to a meter to minimize attenuation effects, although minimal in all cases. From recorded signals test signal, each individual frequency band is extracted and is normalized. This gives a common reference signal power to compare the scaling of each frequency. Initial results are shown in Figure 48, where the received peak-to-peak voltage is a relatively flat response across the spectrum, until approximately 37.5 kHz. At this frequency, the ESC was not capable of achieving the update rate, and it led to an uncontrollable motor, in that full rotor rotation no longer occurred. The other frequency of note is that of 20 kHz, where two measurements are found to be outliers in terms of voltage. The status of them being an outlier was confirmed by additional testing within that frequency. From this collected data, it can be seen that throughout the frequency regime the response is quite flat. Figure 49 shows this data with the outliers and the higher frequencies the motor could not operate in removed. An initial look at this plot appears to have a higher variance than the response presented before, however the voltage range has been dramatically reduced, with a total difference between the minimum and maximum value of 0.0243 volts. Of note, the purpose of the trendline is for visualization purposes and not an exact fit. With this information collected from the thruster, we can apply all the pieces of the system together to validate that no relevant effect has been neglected.

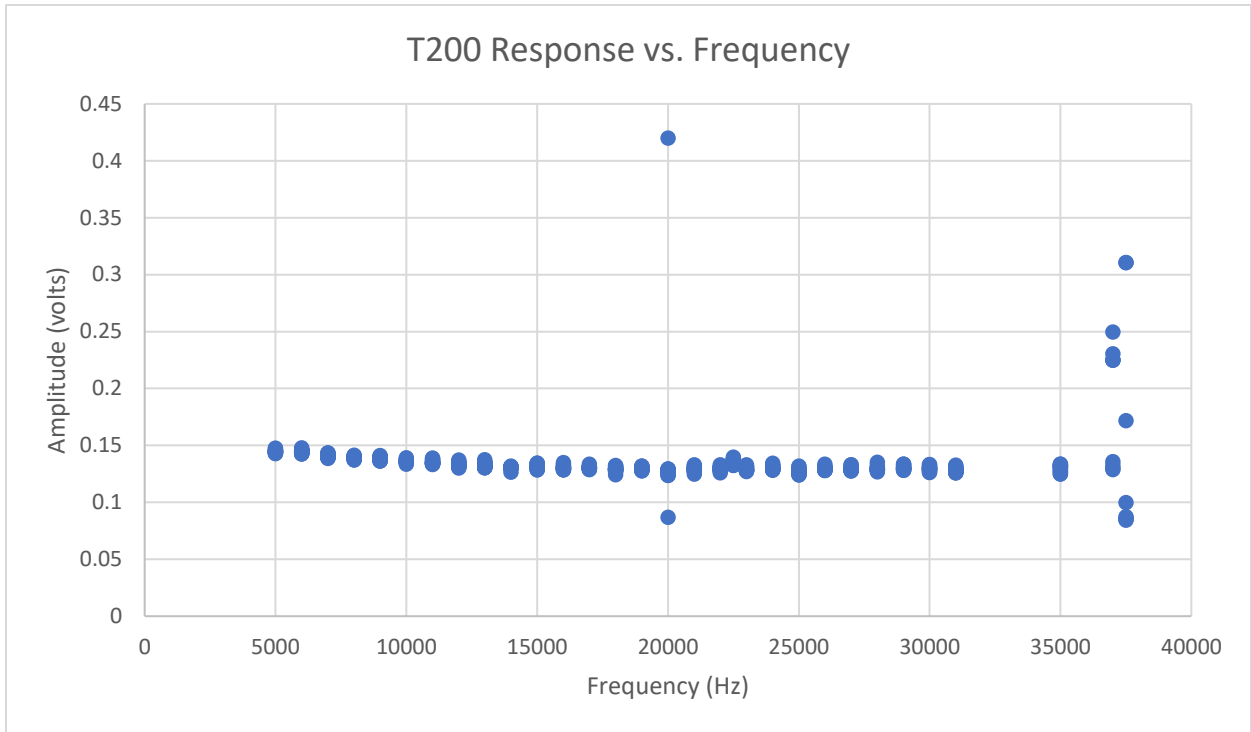


Figure 48: Initial frequency response estimation

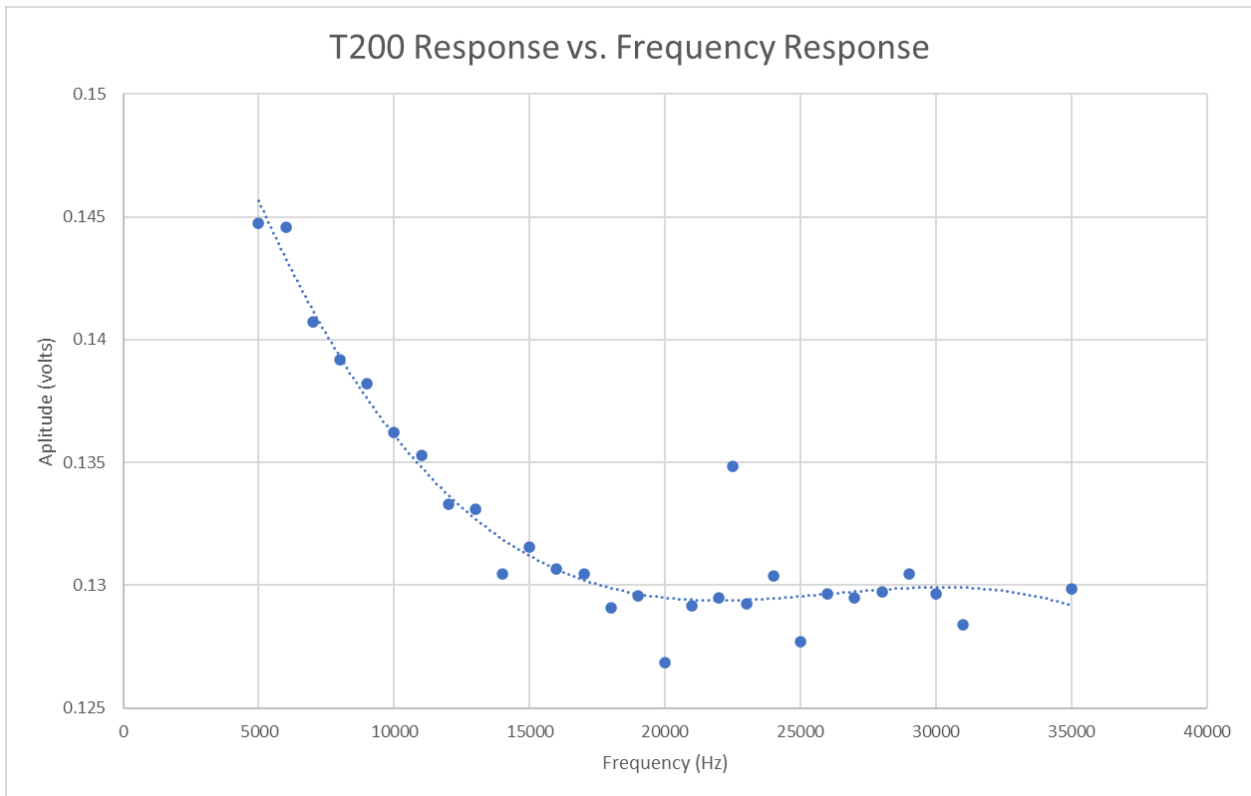


Figure 49: Frequency response of viable frequency range

### Full System Response

Combining all pieces of the system, a full characterization of the system was completed. This involved the transmission of 16-bit LFSR data through all the full system. What is of interest in this data is that the behavior of the system throughout the frequency domain is following the similar trend to the individual identifications. A first pass analysis can be conducted by assuming that the effects of various frequencies transmitted by the motor does not contribute in a meaningful way to the end frequency response due to the small variations it experiences. From this, the relative strength in power between certain frequencies can be compared to see if the behavior is consistent. Although the base decibel value will be different, the change in decibels should be consistent between the two. To test this, a similar test approach was used as in the case of the thruster response and the filter circuitry data processing. Testing was conducted at the universities pool with static mounts for both the hydrophones and thruster at a depth of one meter. Each mount was suspended away from the wall to prevent a secondary transmission path. Recorded signals are passed through a short-time Fourier Transform (SFTF) spectrogram to isolate individual frequency responses. The results of this testing are shown in Figure 50. As can be seen, there is a change of 3.53 dB over the range 20 of 25 kHz. Comparing this to the filter circuitry response in Figure 39, there is a comparable change of 4.06 dB.

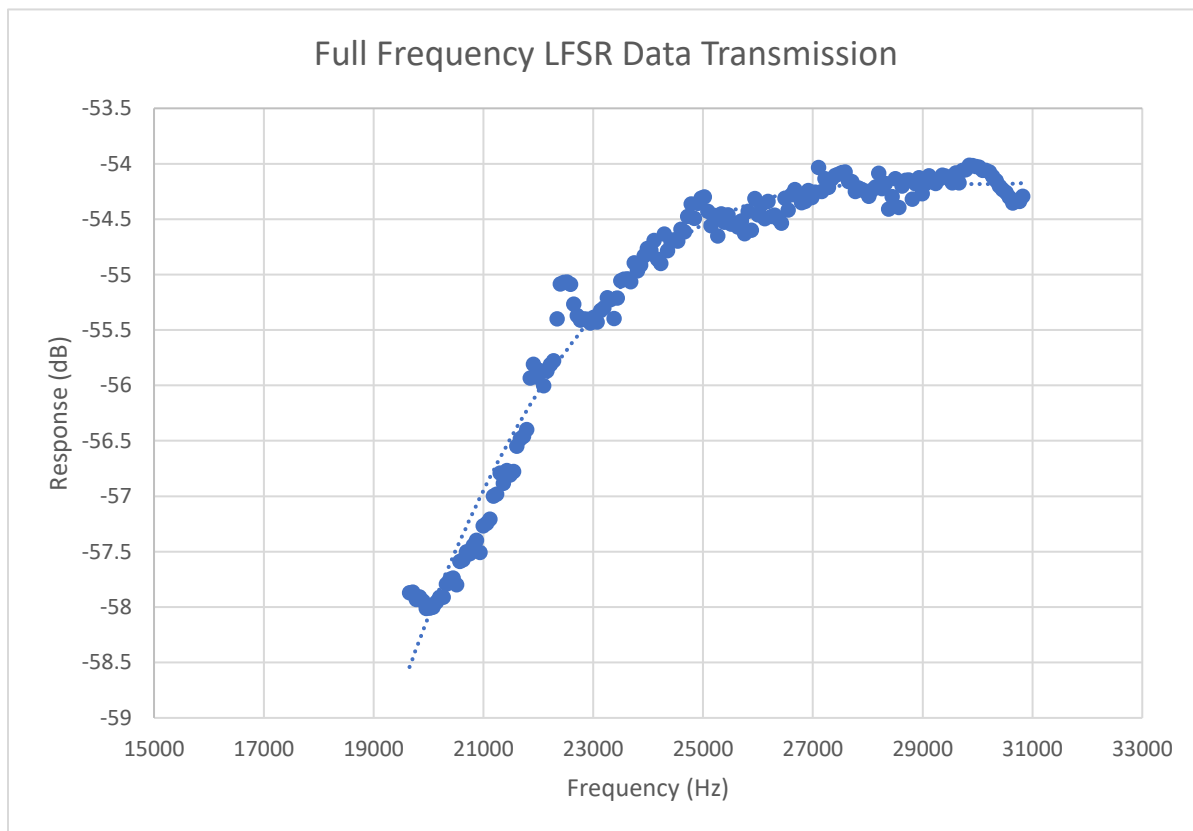


Figure 50: Full system identification - LFSR transmission

This comparative behavior can be evaluated throughout the entirety of the frequency band using trendlines fit to the data. To compare these frequency responses, the deviation in the trendline behavior can be compared between the two trends. Data was first converted to magnitude values of decibel values to make this comparison as direct arithmetic can be applied. The results are shown in Figure 51. As can be seen, throughout the frequency range, the errors from what was predicted are quite small. This implies that the understanding of the hardware is as expected.

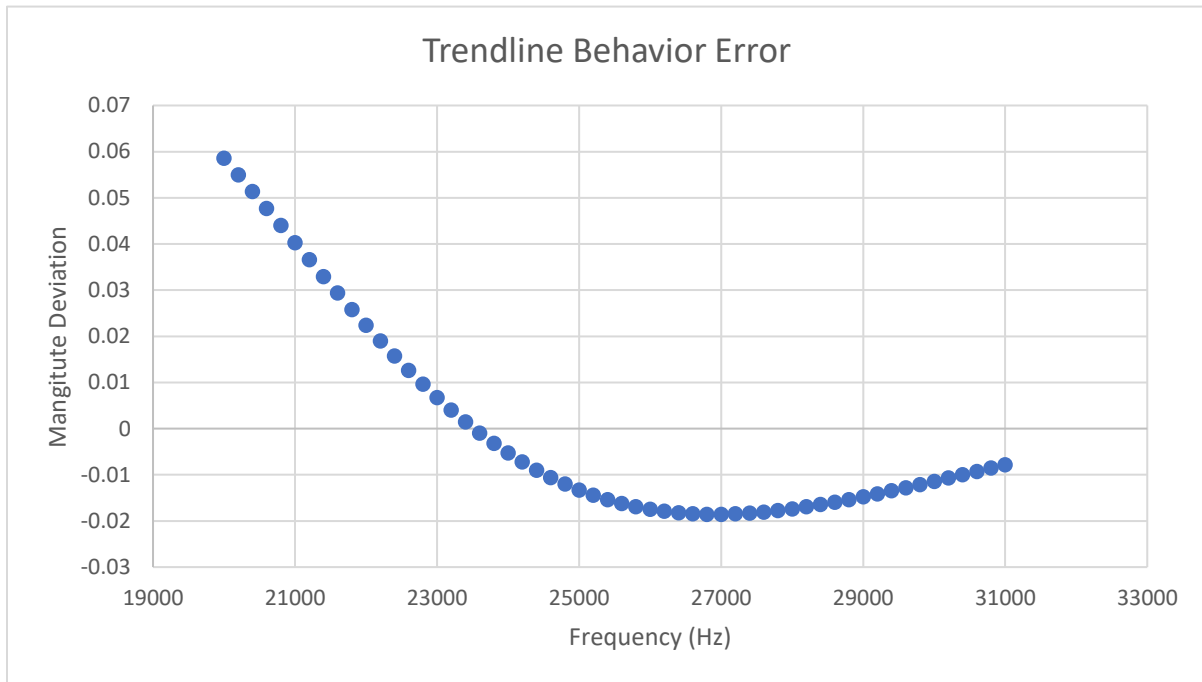


Figure 51: Comparison of trend behavior - full system and filter system

### Theoretical Transmission Rates

To assess the performance of the link, it must be determined what the maximum achievable performance of the link is. For the purposes of this evaluation, the metric that will be used to judge performance is data throughput. To determine these limits, two different aspects of the system will be considered, the maximum symbol transmission rate allowed by the hardware itself and the maximum baud rate allowed by the protocol being used.

First, the performance limits imposed by the hardware will be determined. For reference, all parameters used in these calculations in defined in Table 4. A primary aspect of this is determining the maximum achievable carrier rate, which is proportional to the symbol rate through the number of bits per symbol. To determine this maximum carrier rate,  $m$ , some characteristics of the system must be defined. The frequency update rate,  $s$ , refers to the speed at which a new frequency can be queried from by the ESC control loop. The maximum overlap,  $L$ , refers to the desynchronization of the ESC control loop and communication loop and reflects

the slight increases in symbol width that can occur from this. This overlap is described in Equation 9 and as can be seen, is a function of both the maximum carrier rate and the frequency update rate. The final consideration comes on the receiver end and reflects the impact of filter spreading,  $p$ , for a given symbol. This causes an individual symbol to allocate more of the spectrum and can interfere with other symbols.

Combining these parameters, the relationship between the hardware considerations and the maximum carrier rate is shown in Equation 10. The only additional term that should be noted is the value 1.5 on the left half of the equation. This term serves to represent the ability to distinguish between whether a portion of time represents one or two symbols of the same type. Equation 9 can be substituted into this relationship Equation 11, which removes the overlap as a parameter. From this, the relationship can be rearranged into the quadratic form, shown in Equation 12. Finally, by applying the quadratic formula, the maximum carrier can be calculated directly, shown in Equation 13.

Table 4: Maximum carrier rate parameters

Parameter	Definition
s	Frequency update rate
m	Maximum carrier rate
p	Percentage of filter spreading
L	Maximum overlap
k	$k = \frac{(1+p)}{1.5}$

Equation 9: Maximum overlap of control loops

$$L = 1 + \frac{m}{s}$$

Equation 10: Maximum carrier rate relationship

$$\frac{1}{m} * (1.5) = \frac{1}{s} * L * (1 + p)$$

Equation 11: Maximum carrier rate in terms of frequency update rate and filter spreading

$$m = \frac{s}{\left(1 + \frac{m}{s}\right) \left(\frac{1+p}{1.5}\right)}$$

Equation 12: Maximum carrier rate in quadratic form

$$m^2 + sm - \frac{s^2}{k} = 0$$

Equation 13: Maximum carrier rate solution

$$m = \frac{-s \pm \sqrt{s^2 - 4 * 1 * \frac{-s^2}{k}}}{2}$$

As expected from the knowledge that the overlap can be described in terms of the frequency update rate and maximum carrier rate, the independent variables affecting the maximum carrier rate are only the switching frequency and the frequency spreading of the filtering. This provides a general equation for all ESC communication solutions implemented in this way, but also allows for the specific values from the VESC hardware to be used. The frequency update rate of the ESC is hardware limited and runs at the maximum rate possible, in the case of the VESC, it is 10 kHz. Therefore, a relationship between the filter spreading and the maximum carrier rate can be produced by substituting the known switching rate in. Figure 52 shows this relationship. As can be seen, as spreading grows, it becomes eventually impossible to distinguish what is being transmitted, meeting our expectations. This relationship also determines what is the theoretical maximum number of symbols per second that can be transmitted, 3229 symbols/s, and this occurs only in theoretical circumstances with ideal filters.

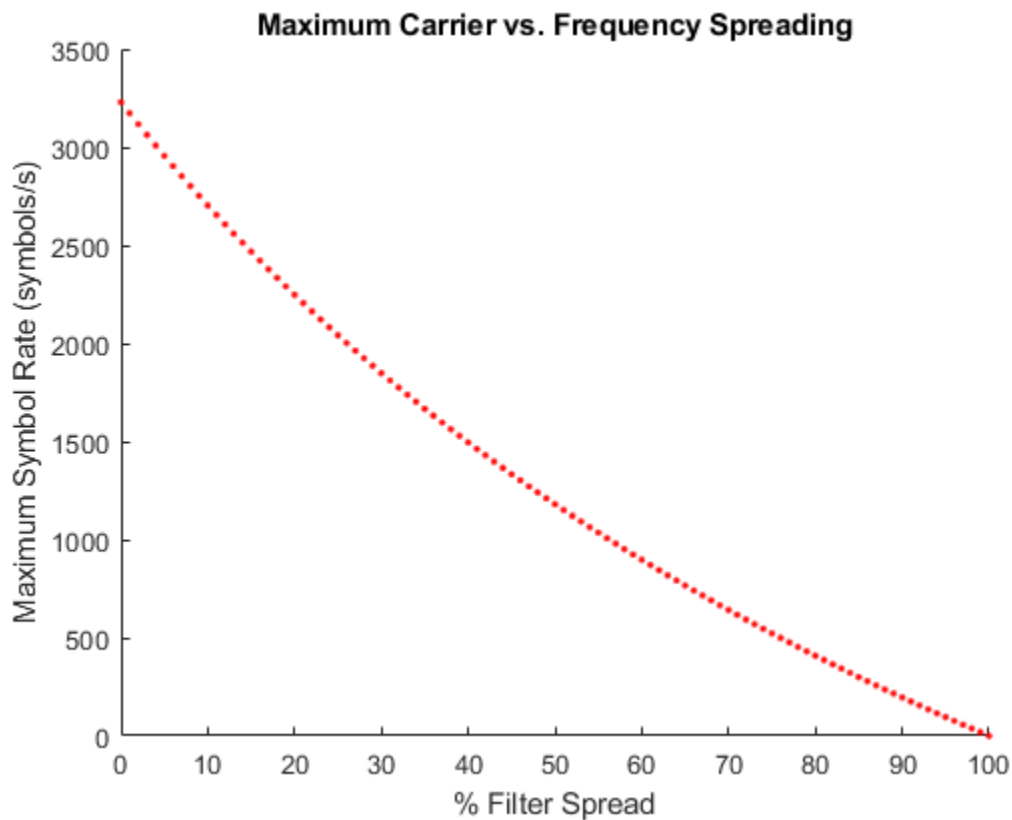


Figure 52: Maximum carrier rate as a function of filter spreading

While the system may have a theoretical limit of the number of symbols per second that can be transmitted, reaching this rate is a different matter. When applying a protocol and bandwidth limits to the data being transmitted, the actual data throughput is reduced. The protocol under consideration is a generalization of the one presented in the communication system section, where one Null symbol is followed by a number of data symbols, the specific number being configurable. The impact of the variable payload size is reflected in the amount of actual data transmitted out of the allowable maximum data rate. The Null symbol indicates the presence of a message; however, it does not contain useful information so it should be considered as overhead of the theoretical maximum data rate. For instance, considering the protocol presented in the experimental testing section, one of the nine symbols being transmitted is Null, meaning that 11.11% of the symbols transmitted were not actually communicating information. With this in consideration, the maximum data rate under our given protocol can be determined.

To conduct this analysis, the two main parameters of the protocol will be considered, the number of bits per symbol and the number of data symbols in a message payload. To compare these variables on equal footing, a constant bandwidth will be used, in this case 10 kHz reflecting most of the useable frequency range determined through hardware testing. Considering the generalized form of the protocol, the number of symbols is described by  $2^n + 1$ , with  $n$  being the number of bits per symbol. As the number of symbols increases, the carrier rate allowed by the allocated bandwidth would decrease proportionally. For reference the highest carrier rate would be in the case of one bit per symbol, or three symbols total, with a symbol rate of approximately 1667 symbols/s. This symbol rate is just over half the hardware maximum of the system, showing the large impact that the bandwidth and protocol can have on the system.

Applying the discussed relationship to a range of protocols and payload sizes, the relationship between the number of bits per symbol and data rate can be seen. Figure 53 shows this relationship. Of note, the values of one bit per symbol and three bits per symbol result in the same trendline, so the representation of one bit per symbol is obscured. From these trends, the highest performing protocol would be using two bits per symbol, with the peak data rate occurring when the highest portion of the transmission is useful data. The impact of the size of the payload decreases with each additional symbol, which is also to be expected. If projected to infinity, these plots would predict the upper limit of data rate allowed from the band allocation, 2 kbits/s in the case of the best performing protocol. From these insights, a more informed decision about what number of bits per symbol to be used, as in the initial protocol discussion this was left ambiguous.



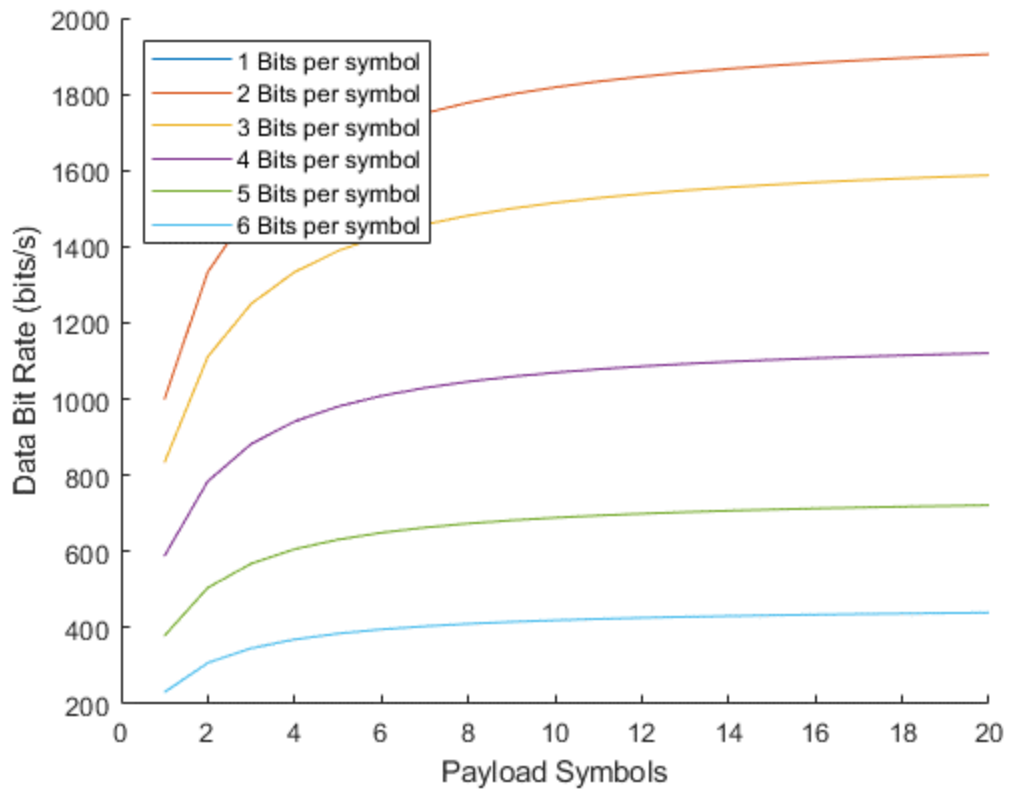


Figure 53: Data rate at various bits per symbol – 1 bit per symbol and 3 bits per symbol occupy the same space

## Chapter 5: Simulation

Modeling of the thruster as a transmitter is an important step to understanding the real-world behavior, however it is not the complete picture of underwater communication. Especially in the shallow waters of littoral regimes or surf zones, propagation effects can have a large impact on communication. To ensure the experimental testing of the system has these effects properly considered, a simulation was constructed, allowing for ease of creating various scenarios to isolate individual effects. This model is based on the MATLAB propagation models for channels and accounted for the major factors impacting communication, namely: attenuation, reflected losses and reflections.

### Image Method Simulation

In testing a communication link, it can be useful to create a simulation of how a transmission propagates through an environment. This allows for many test cases to be evaluated, something much less feasible in field testing. In its simplest form, an environment and a data link can be described as two points in a rectangular space. A two-dimensional model can be used as it will capture the impact of signals bouncing off different surfaces and the delayed reaching of the receiver, the source of self-induced noise in an environment. Other sources of propagation effects can be added independent of the environment, being treated as a noise floor added to the signal.

The original approach to modeling the transmission between a source and receiver in an environment was first proposed by Jont Allen and David Berkley in 1979. Although this would be considered old in terms of research, the methodology is based on a physics approach of expanding pressure waves and as such has stood the test of time, simply improving in accuracy with computational advances. Their approach, known as the image model, uses an approach where a transmitter in the model produces a pressure wave. Spatially adjacent points, or 'pixels', become excited simultaneously, creating spherical wave propagation (Allen & Berkley, 1979). A pressure wave expansion model is shown in Equation 14, where P is pressure, X is the source, X' is the receiver, j is the imaginary number,  $\omega$  is the angular frequency, R is the range, c is the speed of sound, and t is time.

*Equation 14: Pressure wave a single frequency point*

$$P(\omega, X, X') = \frac{e^{j\omega\left(\frac{R}{c}-t\right)}}{4\pi R}$$

A visualization of how this pressure wave propagates is shown in Figure 54, below. The source (o) and receiver (x) are within one rectangle representing the room. The receiver is mirrored about each axis to allow for direct line paths to be drawn to each of them from the source. When one of these paths intersects a wall, the energy loss of the intersection is calculated on the path.

With this methodology, an arbitrary number of paths can be calculated, and ones with the most associated power can be easily determined. When combining the paths at the end, the information about the length of the path can determine the signal phase and the delay of arrival.

## IMAGE EXPANSION $p(t)$

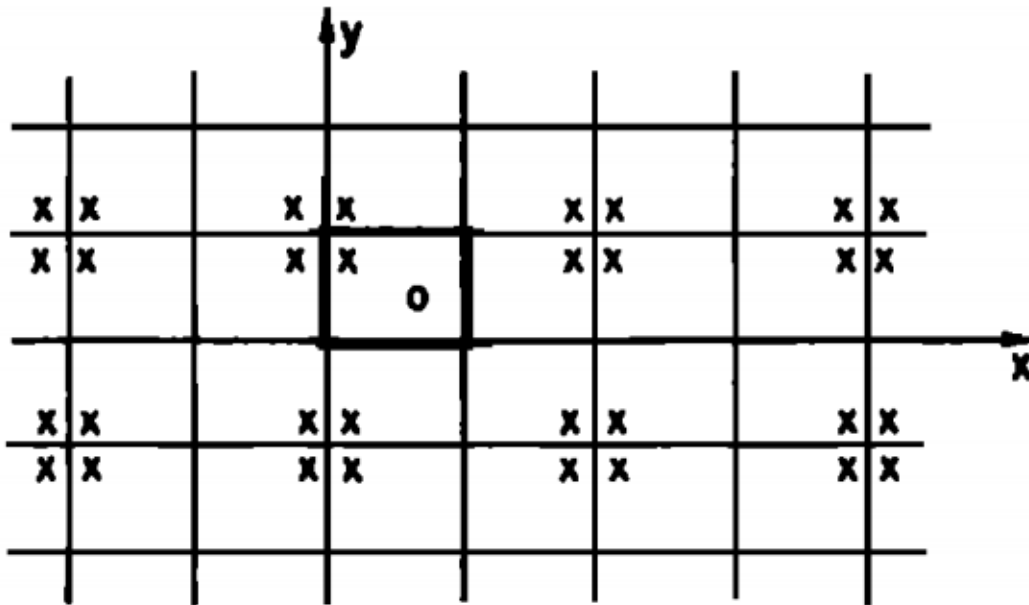


Figure 54: Image expansion of source (o) and receiver (x) (Allen & Berkley, 1979).

### Shallow Channel Model

The goal of the simulation was to be representative of the target environment as well as where experimental testing will be performed. Experimental testing of the modem was conducted in the universities pool to provide a controlled location and served to validate the functionality of the modem. In terms of shallow water propagation, this test location serves to produce a high quantity of reflected transmission paths, with depths of a meter and a separation potential separation of transmitter and receiver at a similar distance. To describe this, a MATLAB simulation was created of a shallow water channel using the image method. Figure 55 shows a visualization of the 10 transmission paths that would first arrive at the receiver. The environment shown is customizable in both depth, and source and receiver position, with a 1m separation range and 5m depth shown. The most important aspect to consider at this ranges is that even the longer reflection paths are not far behind in time from the initial arrival. In the presented case for instance, the difference between the arrival time of the direct path and the longest is only approximately 12.7ms, not more than two whole messages of difference with the current message protocol.

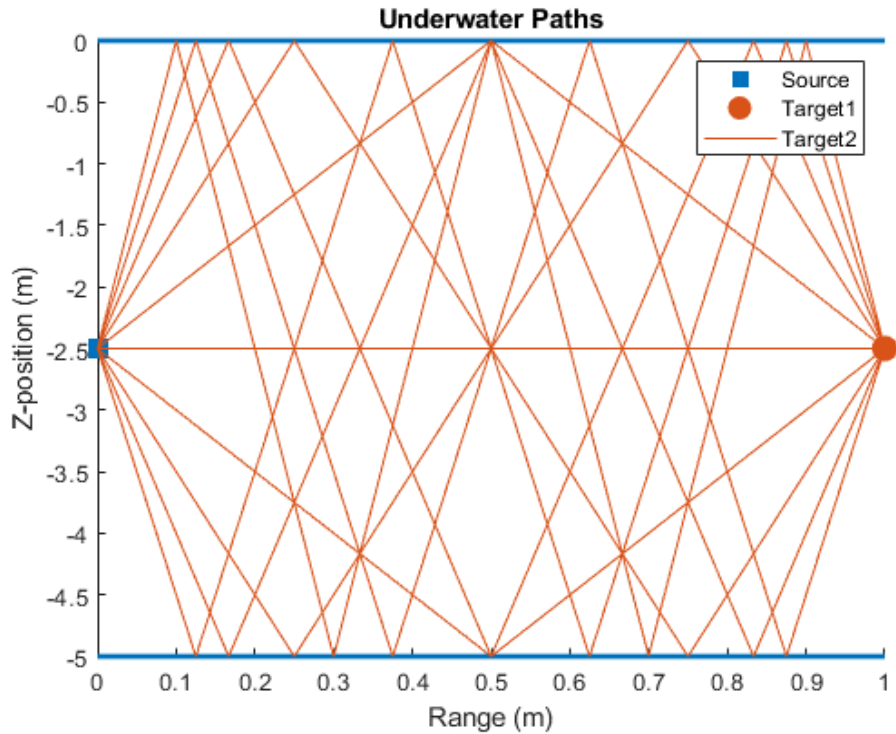


Figure 55: Shallow channel model transmission paths

Building upon this reflection model, a reference pulse can be generated and the signal at the receiver can be computed. For the presented figures following, they were generated in the environment shown in Figure 55. In transmission, the protocol and bandwidth utilized are as discussed in the communication system. A bandwidth of 10 kHz is allocated between 20 and 30 kHz to 5 symbols, a Null and four symbols representing two bits per symbol each. These 5 symbols are modulated using frequency shift keying at a symbol rate of 1000 symbols/s. A visualization of this is shown in Figure 56, with each symbol labeled above its portion of the band. As expected, this approach fills the entirety of the band, With the main lobe of each symbol filling one fifth of the band. For reference, the symbol frequencies are 21, 23, 25, 27, and 29 kHz for the Null, 00, 01, 10, 11 symbols, respectively.

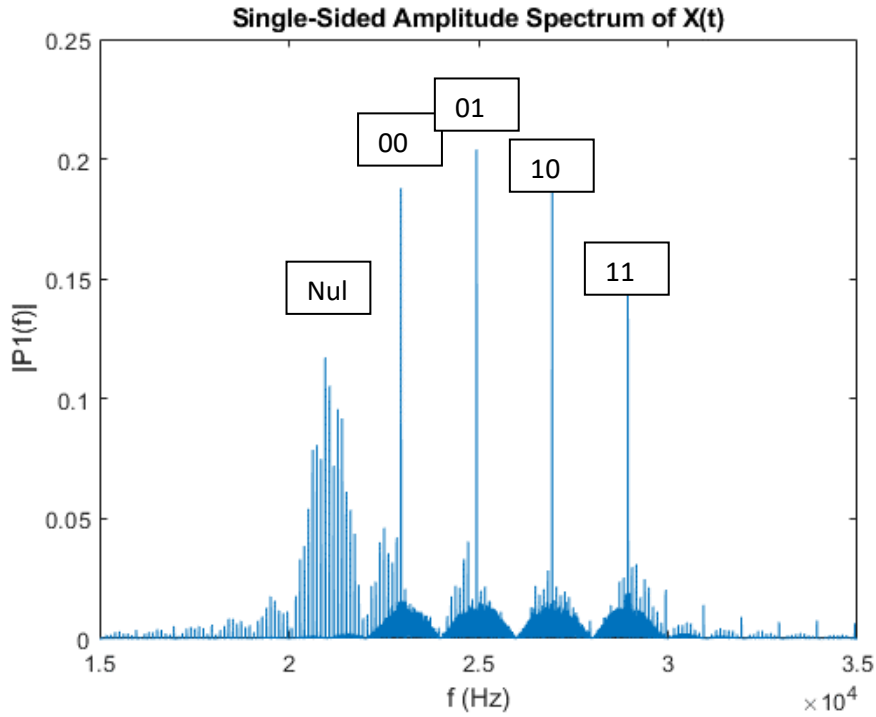


Figure 56: Frequency band of the transmitted data – full transmission, not subset visualized

To transmit, a reference signal was generated, in this case with values randomly generated throughout the 16-bit value range, 0 to 65535. Example plots will show one message from the full transmission for clarity. When transmitting, an ideal transducer is used, with the power is consistent regardless of the frequency being transmitted. This both reflects the relatively flat power response of the thruster throughout the frequency range and allows for attenuation effects to be isolated. Figure 57 shows the generated signal for transmission, in this case with a binary value of 1001011010010101 or 38549 in decimal. Labels are included over each discrete symbol for reference. For clarity, Figure 58 and Figure 59 show a symbol representation of the transmission. As can be seen in the spectrogram representation, each symbol has a period of approximately 1 ms, what is expected at this symbol rate. Also, as expected from the constant amplitude of the transmitted signal, the frequency response of in the spectrogram is of approximately the same magnitude.

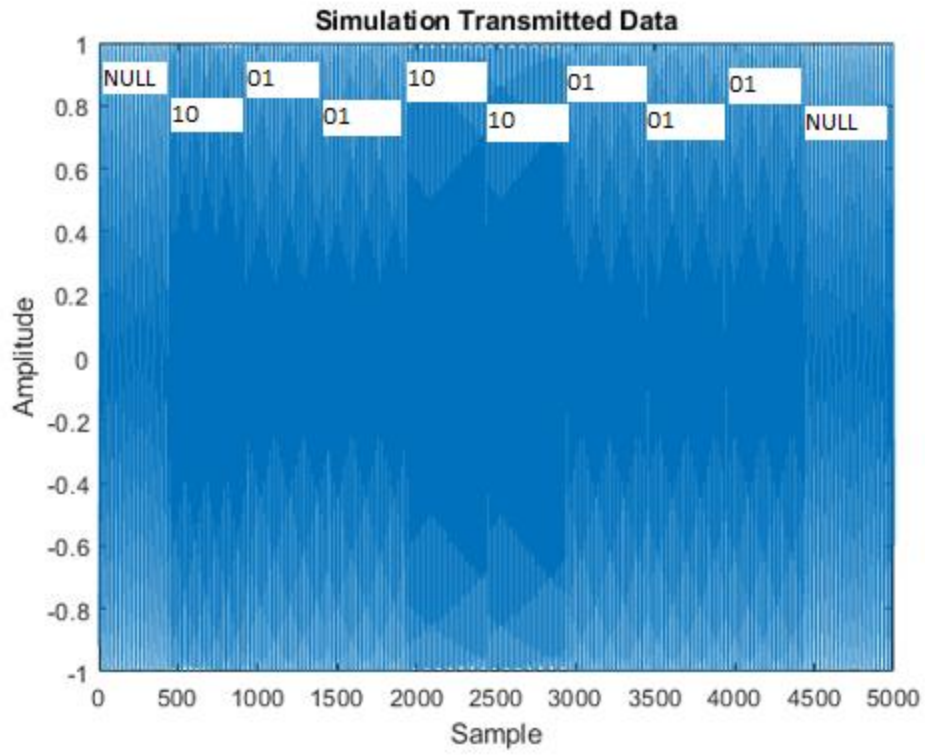


Figure 57: Transmitted data - transmission side

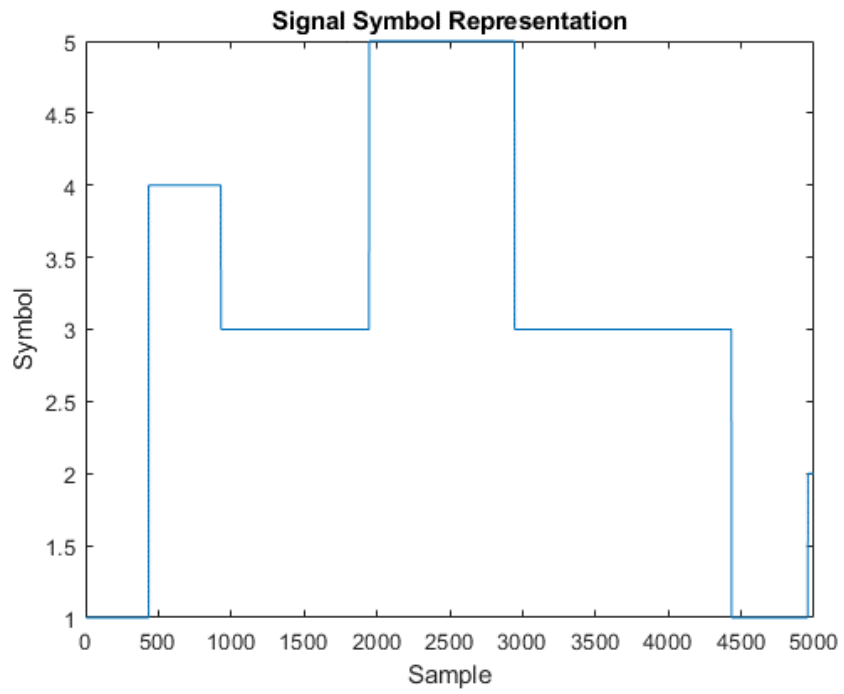


Figure 58: Transmitted Signal Symbol Representation

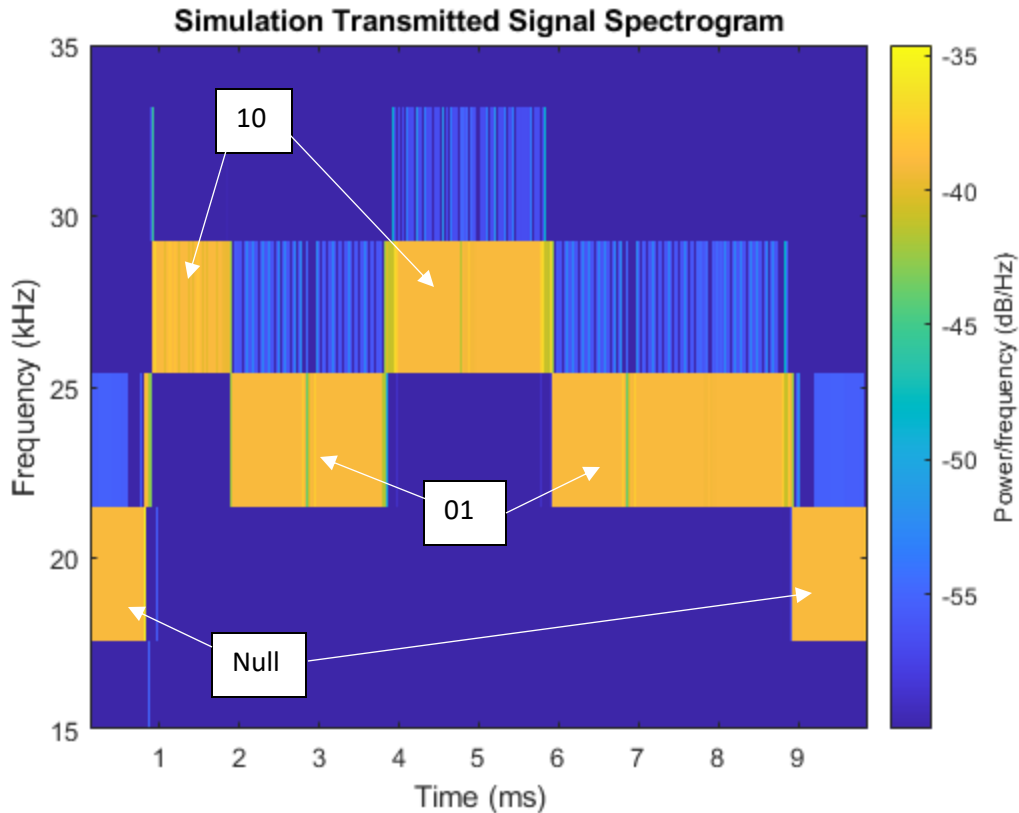


Figure 59: Transmitted data spectrogram

One of the dominant forces in short range communication is the impact of multipath reflections. The primary impact of multipath beyond the obvious impact it has on the amplitude is that it causes phase discontinuities in the signal. Phase can be useful in decoding data as it allows for the application of technologies like the phase lock loop in either hardware or software. The benefit of using this in demodulation as it can be used for extraction of the carrier signal, increasing the reliability of demodulation. In the case of our environment, this technology is unable to be used at all. Figure 60 shows the phase of a single received symbol. As can be seen, the phase angle is not at all coherent. This does not mean that the signal is unable to be decoded, as the frequency information is still present, it is simply a more difficult problem that it could be. The presence of accurate multipath in the simulation allows for decoding performance to be tested on accurate representations of signals in the real world and confirming that it is present can help with validation of the receiver.

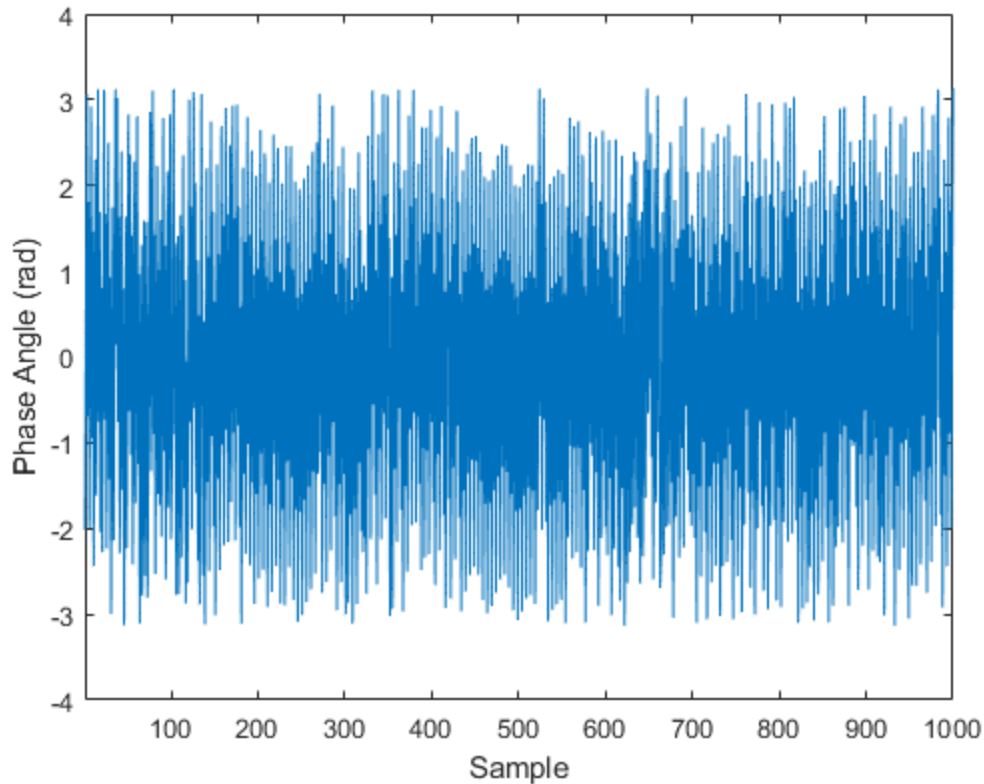


Figure 60: Phase of a signal with multipath present

The other major effect that a signal experiences underwater is the effects of signal attenuation on the various frequencies being transmitted. Although the transmission side of the model has a constant power transmission at all frequencies, the expectation would be that higher frequencies experience higher attenuation. However, this is not what is seen at this range, as shown in received signal in Figure 61. There is no clear relationship between the individual symbol strength and the frequency, with each symbol having a high variability in amplitude. The issue in the prediction is that attenuation over short distances is not the primary driving force of power falloff, multipath reflections are. To validate the attenuation properties, a test eliminating the impact of multipath effects and isolating attenuation effects is needed.



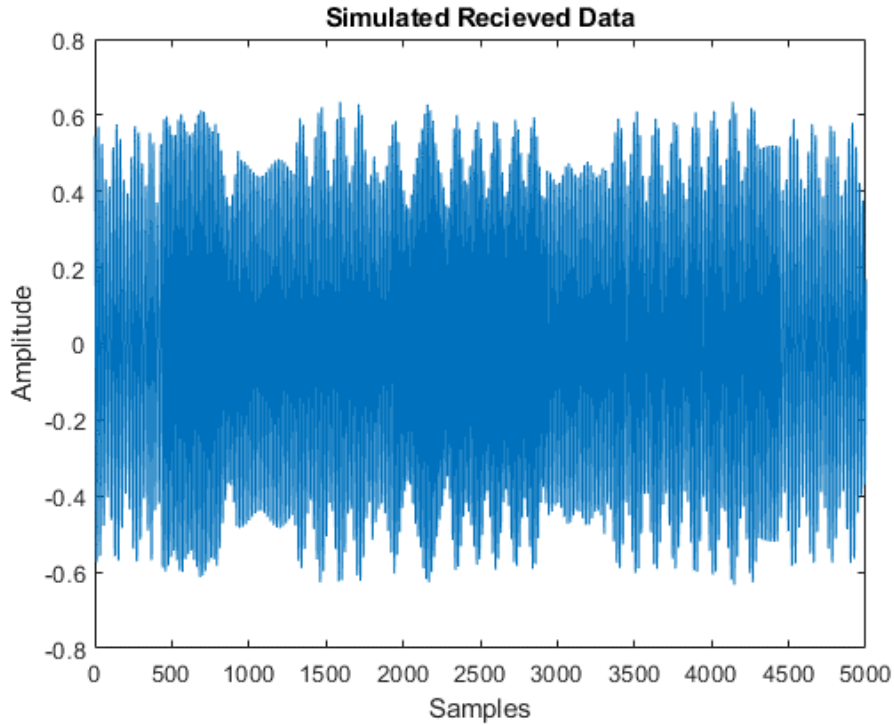


Figure 61: Model received signal

To characterize and validate that the channel is attenuating as expected, a reference linear frequency modulated (LFM) pulse was modeled going through the channel. As it sounds, this function linearly changes its frequency as a function of time, in this case going from 0 to 100 kHz over the period of a second. A sample pulse was shown in the introduction in Figure 8. To isolate it from the effects of multipath, only the direct path was used, however all other parameters of the model were kept consistent. MATLAB uses a free space path loss model to describe the impact of the medium on the signal at range. For a communication system of this nature, Equation 15 shows the relationship of losses as a function of distance and frequency, where  $l$  is the transmission distance,  $l_r$  is a reference distance,  $f$  is the signal frequency,  $k$  is the path loss coefficient, and  $a(f)$  is the absorption coefficient. This signal can then be simulated to be transmitted through the underwater channel. Figure 62 shows the received signal, with the upper and lower bounds of the function highlighted in red and yellow, respectively. As can be seen, without reflections the received signals amplitude is dependent on frequency alone and the impact is higher as the transmission frequency increases. For reference, the starting amplitude is approximately 0.5 and the ending is approximately 0.416, or a percent difference of just over 18%.

Equation 15: Overall path loss (Stojanovic & Preisig, 2009).

$$A(l, f) = \left(\frac{l}{l_r}\right)^k a(f)^{l-l_r}$$

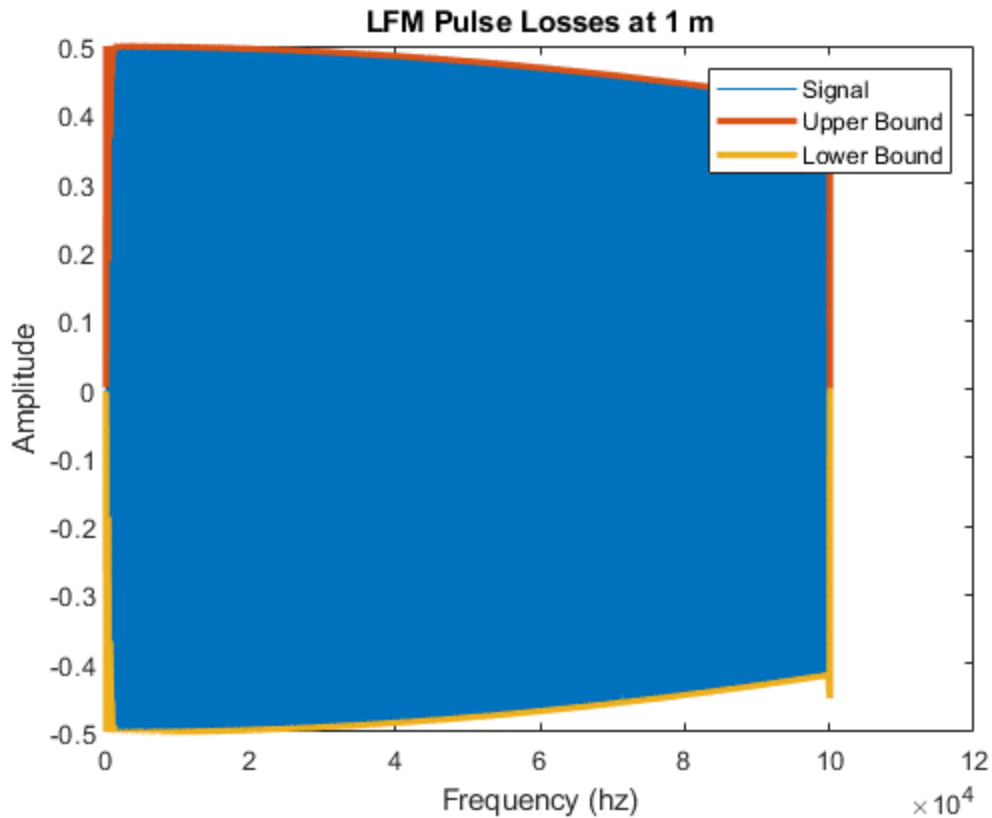


Figure 62: Channel attenuation at 1m

Looking at the received signals, it is prudent to determine whether the received signal is attenuating in a manner comparable to the established models. To begin, the band in use must be considered. As the bandwidth utilized is 100kHz, the bandwidth may be considered wideband. What can be seen in the transmission frequency range of the modem, 20 to 25 kHz, is that one of the largest rates of change in absorption is present, meaning that the received power will vary the most. While not ideal, these frequencies are low enough to minimize the overall loss while being high enough to be useful in a communication system. When considering Equation 15, the terms are dominant in contribution to the shape of attenuation behavior must be isolated. In our simulated LFM pulse, there is a constant range, so the first  $1/r$  term should have a proportionally similar impact on all signals transmitted. This means that absorption coefficient, shown in Figure 63 would dominate the behavior being tied to the frequency value. Of note, this plot is in terms of decibels, therefore it is logarithmic in nature, as reflected by the slope increasing on the change in amplitude at higher frequencies. From this predicted trend, a comparison to the simulated results can be shown. Figure 64 shows the absorption loss computed by the simulation. As can be seen, over the same frequency range, the trend in behavior is comparable. A direct comparison is not discussed as absorption coefficient values will change based on external parameters such as water temperature and salinity. The determination that the simulation is

behaving comparably to the established behavior of underwater absorption indicates that the results can be accepted.

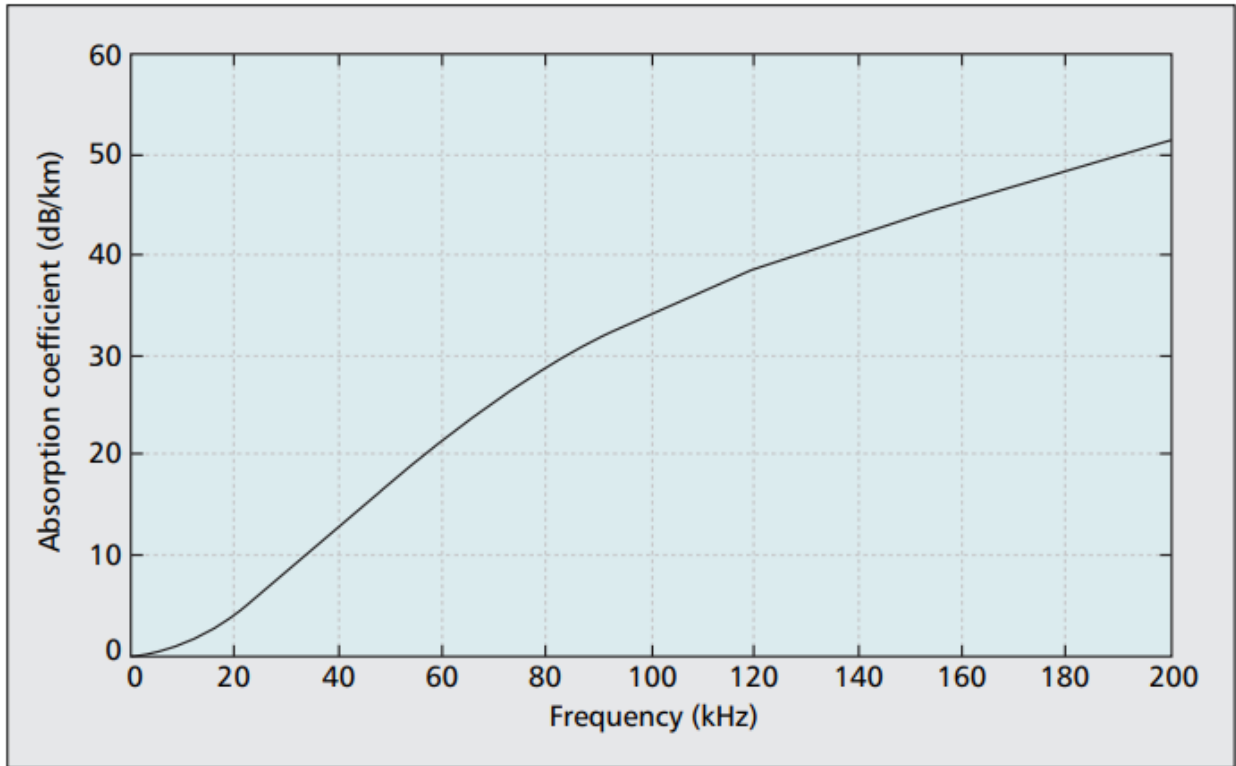


Figure 63: Attenuation as a function as frequency (Stojanovic & Preisig, 2009).

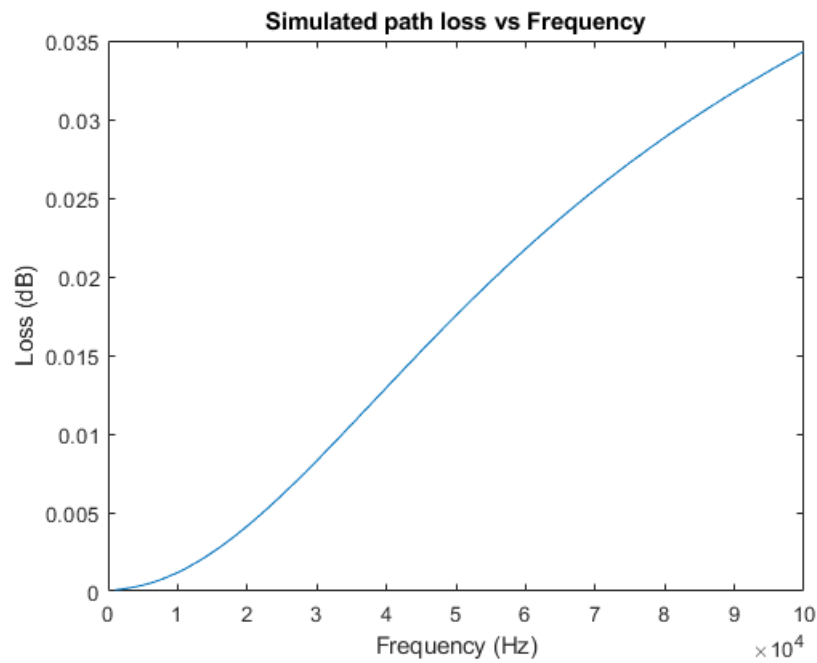


Figure 64: Simulated Path Loss

## Chapter 6: Experimental Testing

Although a characterization of the thruster has been constructed, testing is required to validate the behavior of the system. The primary aspects of the system under consideration are the relationship between the thruster output and communication performance as well as general communication reliability and BER. Beyond validation of aspects of the characterization, applications leveraging the link which are representative of real-world use cases will be tested. This includes data streams such as images and video that a system could use to communicate necessary information to an external source.

### Test Site

Experimental testing was conducted at the universities pool, as it served as a good analog to the target applications of the technology being a highly reflective and shallow environment. All testing presented in this section was conducted at this site. Figure 65 shows an overhead of this test setup, where the orange dots are the approximate locations of source and receiver. Both the hydrophones and the thruster were mounted off the wall, to remove potential transmission paths. Separation between the transmitter and receiver was approximately 10m, with each being mounted at a depth of one meter. This served to be representative of a shallow water channel, where the ratio of depth to width from the surface was 1/10 and from the wall of a ratio less than 1/10. Practically speaking, this means that the channel will have high amounts of reflections, common in the target littoral and surf zone environments this work targets. In terms of separation as compared to the wavelength of the signals being transmitted, these wavelengths are on the order of centimeters, meaning that there is sufficient separation as compared to what is being transmitted.



Figure 65: Pool test environment overhead (Google, 2021).

## Testing Utilities

To allow for ease of interfacing with the VESC, an interface tool was created, shown in Figure 66. It allows for the adjustment of device settings, sending data to be transmitted as well as opening a network socket that allows for any other program to take control of generating the data to be transmitted. The left portion of the UI serves to validate message integrity over the link. Control fields and buttons take up the right portion, allowing the specifics of the link and the data to send to be controlled and monitored. Settings are sent in a manner where the ESC is responsible for utilizing the band in a manner that minimizes the interference between the individual symbols. A full discussion of band allocation is conducted in the further optimization section.

Providing context for the ESC settings, an explanation for each is provided. The frequency band defines the lower and upper limits for the transmission band in Hz. Bits per symbol defines the number of unique data bits contained within each frequency value. Baud rate refers to the number of symbols per second transmitted. Byte and bit stop bits refer to the number of Null symbols placed between a message and an individual bit, respectively. Duty cycle allows for the speed to be manually set on the motor for testing, or a targeted rotational rate can be set in the RPM field. Mode is an unused functionality to allow for multiple transmission methodologies. Bit order refers to the endianness of the transmitted message. Finally, auto send allows for an LFSR method to be executed onboard the ESC allowing for ease of testing. These settings can be set and queried with the respective buttons. Beyond these settings, the tool can send data to the ESC to be transmitted in two ways. In the Data to Send field, data can be entered and sent with the send button. Alternatively, a UDP socket is monitored by the program and data transmitted is passed along to the ESC. This allows for ease of testing with large data transmissions being automated by another program.

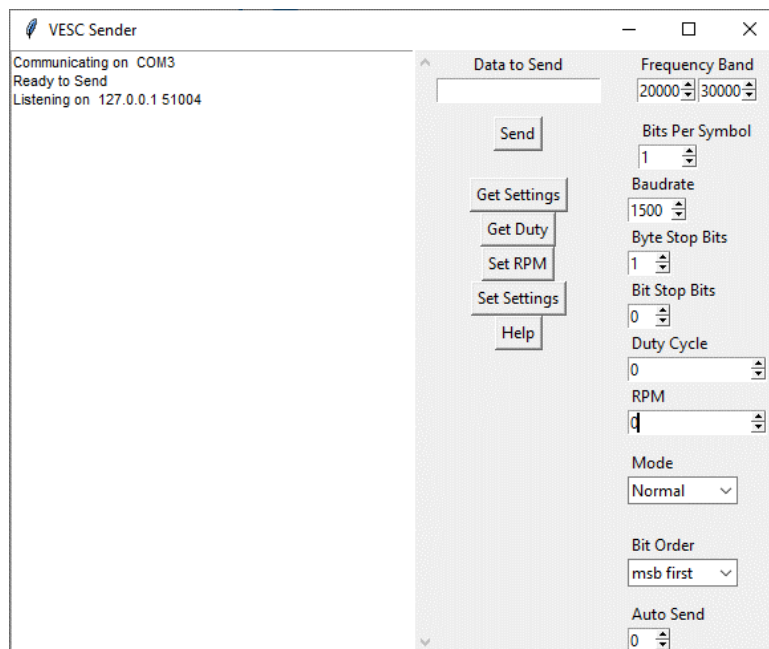


Figure 66: VESC Interface tool

## Test Methodology

To properly test and evaluate the system performance, how the transmitted data will be validated and the metrics between which different test can be compared must be defined. To evaluate the ability of the link to correctly transmit data, a means of validating the accuracy of the messages transmitted needs to be included, as the protocol being used does not have error detection or correction capabilities. From this verifiable data, a bit error rate metric will be defined so as to allow individual test cases to be compared on a common metric.

As there is no inherent error detection in the messages, the data itself is instead in a pattern that is verifiable. The messages being sent were 16-bit linear feedback shift register (LFSR) values, shown in Equation 16. This approach creates a pseudorandom distribution throughout the range of values, covering different bit patterns in a manner that better covers the creation of different reflection frequencies in the environment as opposed to a sweep of all 16-bit values. A visualization of this is shown in Figure 67. As seen, the full range of 16-bit values is covered, excluding zero. Zero is excluded because the computation of the LFSR involves the XOR operation, and the use of all zeros would evaluate to all zeros again rather than changing to a new data value.

Equation 16: LFSR Polynomial

$$\text{Feedback Polynomial: } x^{16} + x^{14} + x^{13} + x^{11} + 1$$

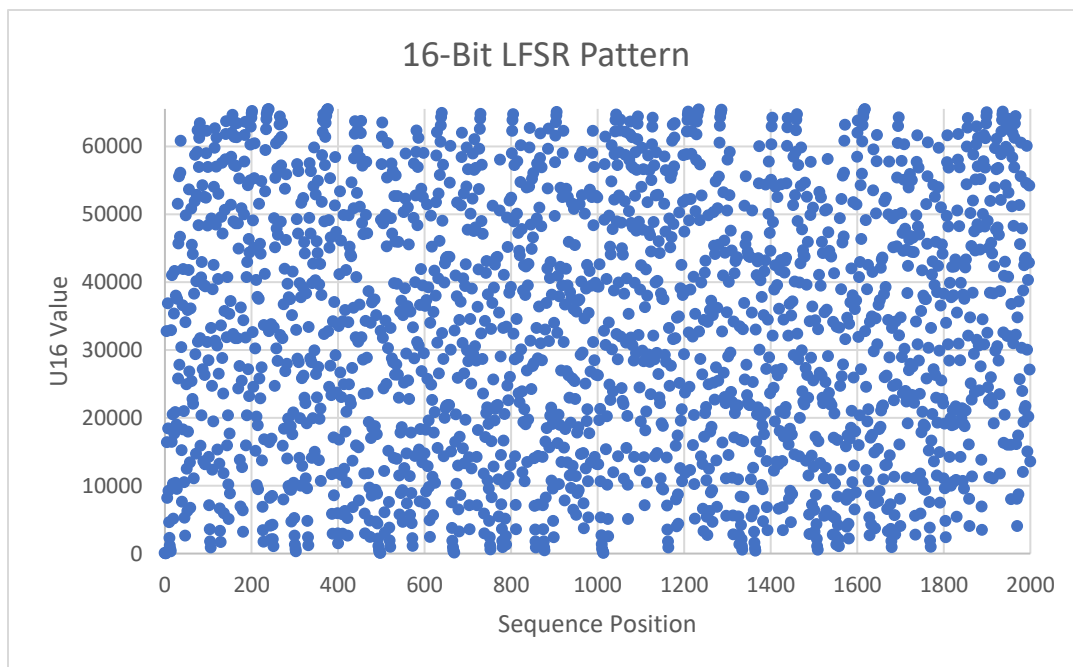


Figure 67: 16-Bit LFSR Visualization

This main benefit to this approach in data transmitted is that it allows for the prior message to be used to check if the current message is correct, as the LFSR scheme is known. This benefit of this approach to checking is that drops in receiving messages only result in one message worth

of bits being unverifiable. Each prior message is used to verify the next in sequence. It also allows for the managing of drops in communication. When a lost transmission is picked up again, rechecking of values can begin again.

The bit error rate values presented are a result of computing the number of correct bits of the current message based on the prior message transmitted. Equation 17 shows how this value is calculated. Of note is the -1 term in the messages received. As the first message cannot be validated against anything, it is removed from consideration. The bits from this message do not contribute to the numerator term of number of bits correct, and a single message of the transmission not being used is a small tradeoff for being able to validate the remaining messages correctness.

*Equation 17: BER equation*

$$BER = \frac{\# \text{ Bits Correct}}{(\# \text{ Messages Recieved} - 1) * (\text{Message Size})}$$

### Motor Spin

Testing was accomplished by sweeping through the range of duty cycles achievable. As this is a test of steady state (fixed motor speed) performance, the motor was brought up to speed before transmission begin. Duty cycles to be tested ranged from a duty cycle 35 to 65%. Higher amounts of thrust in either direction was not possible as the means to mount them statically was not there. If a motor is moving, the behavior of the acoustics is not directly comparable. For each of the duty cycles tested, multiple trials with 7500 messages each were conducted. This quantity of messages produces sufficient coverage of the spectrum while not being exhaustive of all possible values. The link parameters used the same properties as tests conducted for characterizing the link. Data was transmitted at a symbol rate of 1 kSymbol/s, meaning that an individual symbol is 1ms long, or 21 full phases at the lowest frequency of 21 kHz. This is far more than the theoretical requirement of 1 full phase to determine a frequency's presence. A bandwidth of 10 kHz was used, along with five symbols, one Null and four data, filling the band entirely.

The key aspect of the characterization to consider in experimental testing is the prediction about the behavior of the thruster at various speeds. However, this cannot be considered alone, as will be discussed. An analysis of the impact of signal to noise ratio must be simultaneously conducted to eliminate other potential biasing in the data. The determination of the SNR at any given point is difficult as the primary driving source of the noise from multipath. To address this matter, an assumption is needed. As this experiment was presented in one test with a consistent hardware arrangement between all test cases, it can be assumed that the noise produced is consistent between all cases. With a fixed position, the primary reflection paths would be consistent. The variable aspect of the noise would be derived from the actual data being transmitted, as the frequency continuously changes because of being transmitted. The use of an LFSR to cover all the range of possible values to transmit, and as such all frequency patterns being present means that the noise will have an average value that it converges to.

A possible source of error in these results may arise from data being transmitted through a secondary path. In the case of this testing, it would be from electro-magnetic emission between the cabling runs. To eliminate this as a potential factor, additional testing of test cases was conducted with various cable coiling and separations. In no case, including with the power cabling of the motor and hydrophone cables coiled together was a difference in performance seen, indicating the cabling itself was performing properly and was sufficiently resistant to external influences.

Test results are grouped by the baud rate they test signals were transmitted at. Plotted results are shown in Figure 68. A tabulated version of these results is available in the appendix in Table 6. As discussed, a consistent hardware arrangement was kept between all tests, in this case with a range of approximately 10m. Of note in the plot is the use of a log scale on the y-axis. While useful for visualizing the bit error rate, it can also bias some perspectives on the data. The standard deviation and variance on this error over all cases is on the order of  $10^{-3}$  and  $10^{-6}$ , respectively, indicating that there is little variability between all test cases. Pairing this conclusion with the observation of the consistent signal amplitude results presented in the characterization section, it can be concluded that the speed of the thruster has a negligible impact on data link.

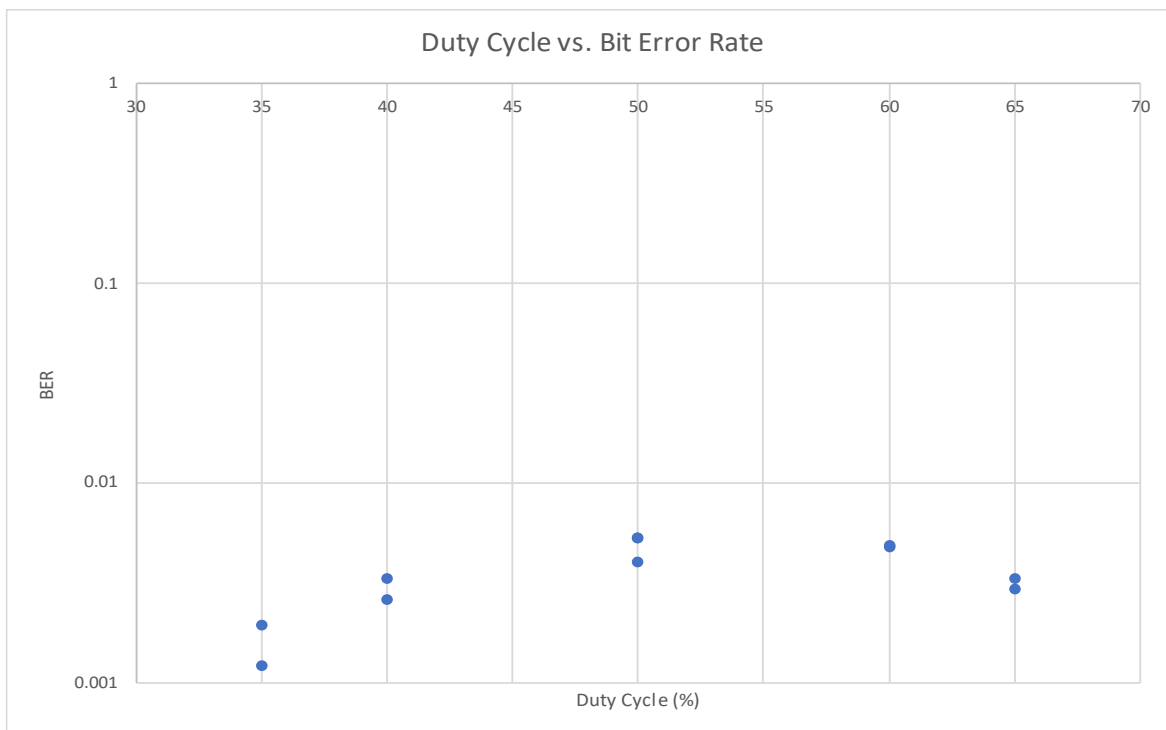


Figure 68: Duty Cycle vs. Bit Error Rate



## Image Transmission

Cameras are commonly used on submarine platforms, especially in cases sonar is either too expensive or unable to fit into a system. Image data provides a unique benchmark for transmission as it is a large amount of data per frame that needs to be transmitted in a long sequential manner. Sending this data requires consistent detection of messages to guarantee all pixels are obtained and correct reconstruction can take place. Although protocols can be used to reduce the impact of missed data on the reconstruction of the image, and compression techniques can be used to reduce the transmission requirements, each of these approaches bear a penalty in terms of transmission time and BER requirements, respectively. Of these approaches, compression will be evaluated as a proof on concept for higher speed transmission of video data. For all test cases presented, they were done in a small water tank at close range, less than a meter. This was necessitated as some of the larger data transmissions took a non-trivial amount of time, an hour in one case, and this test setup allowed for the environment to be guaranteed to be consistent throughout the time.

### Raw Image Transmission

The first test conducted was the transmission of a frame pixel by pixel. This was done by reading in the RGB value of each pixel in as a 32-bit floating-point value. This was then sent using the established protocol as two messages, the upper 16 bits then the lower 16. Figure 69 shows the original frame transmitted and frame reconstructed from the received data. As can be seen, the frames look nearly identical, with the only source of error being in the end of the frame, where data was seemingly lost. Figure 70 visualizes the correctness of the received frames, with every blue pixel representing a correctly received pixel. The error received at the end appeared to be in the logging of the data upon evaluation, where the log prematurely stopped recording, and was not a product of the data being incorrectly transmitted. Overall, this initial test validated that larger amounts of data related to each other could be successfully transmitted.



Figure 69: Raw frame transmission, original (left), received (right)

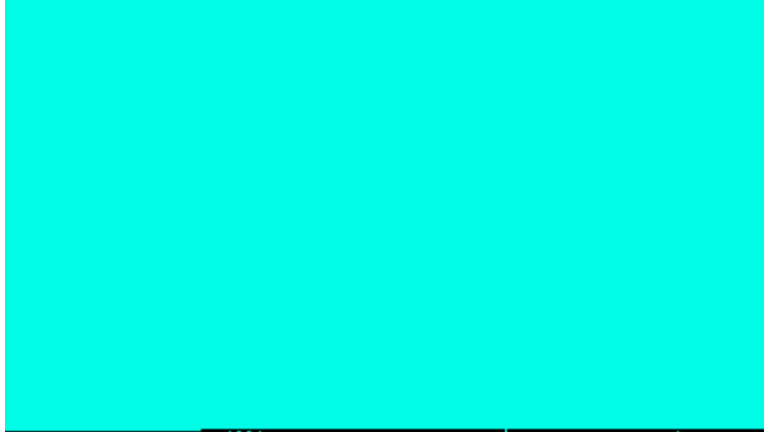


Figure 70: Raw image received frame difference

From this success, a few conclusions can be drawn. Firstly, the modem is capable of transmission for prolonged periods of time without fault. At the transmission rate of 1000 symbols/s and an image size of 384 x 216 pixels and 32 bits per pixel, transmitting this image takes nearly 25 minutes. In practice, this speed is clearly not ideal for the continuous transmission of images, however it does serve to give a baseline to demonstrate it is possible to transmit a mission critical image if needed. The other big takeaway from this transmission success is that it confirms at this transmission rate, the ESC is capable of properly serving the requested transmissions. As of now, this does not disprove any of the theoretical calculations on the theoretical limits of the ESC.

#### Harmonic Image Transmission

A topic that will be discussed in greater detail in the optimization section of the paper is the concept that data can be transmitted at higher data rates by leveraging the properties of the harmonics of the transmission band. The key principle of this concept is that at higher N odd harmonics, the symbol rate can be N times the speed it is in the original band, at the cost of power reductions. Using this principle, the same image can be transmitted at 3 times the speed, within the 3<sup>rd</sup> harmonic band of 60-90kHz. Of note for these tests, the Teledyne hydrophones were required to be used as the Sparton sensors have a frequency limitation that prevents them from hearing this frequency band. As such for this test case and the following video test case, the symbol rate of the link is 3000 symbols/s. The bandwidth allocation here allows will allow for video transmission, but initial validation is conducted on a single image being transmitted. This image, shown in Figure 71, is compressed using PNG compression over a canny edge filter. This allows individual frames to be approximately 6 kilobytes, or one frame every 2.5 seconds in transmission time. While in practice this means that you are unable to transmit a video feed live, this does allow for crucial information to be sent relatively continuously. In regard to the BER of the image transmission, this particular frame was successfully transmitted with zero error. Again, as in the case of the last image this is due to the short range of transmission available for testing. When sent as a full video, some errors do show up and will be discussed in the next section.

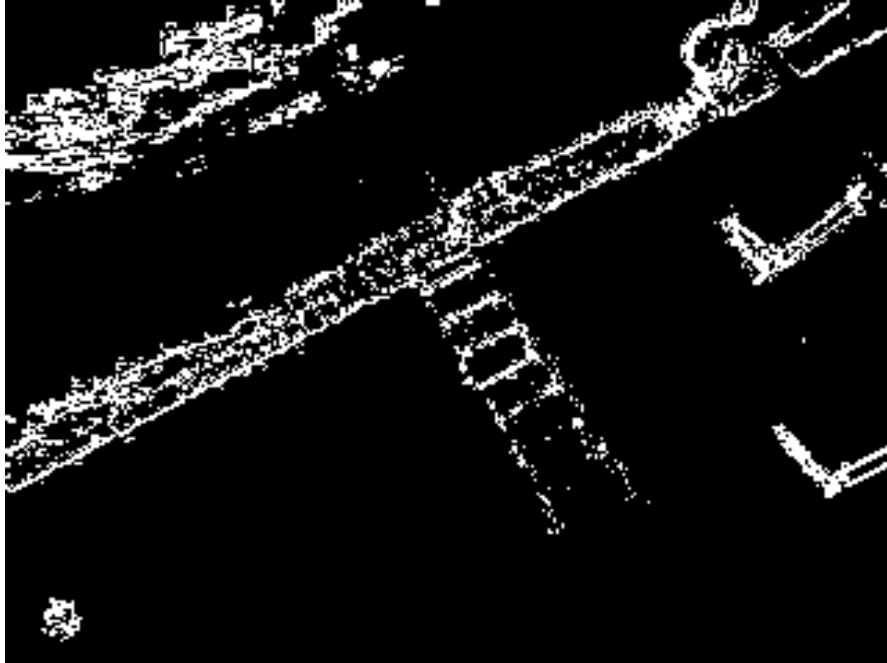


Figure 71: PNG compressed image transmitted on the third harmonic

### Video Transmission

To validate the performance of continuous data transmission over time, a video transmission was conducted to utilize a common underwater sensor that produces a large amount of data. In a practical sense, this modem implementation cannot manage video streaming without large amounts of compression. As a middle ground for testing, the video was transmitted with per frame compression, rather than full video compression. A comparative frame before and after this filtering and compression process is shown in Figure 72.

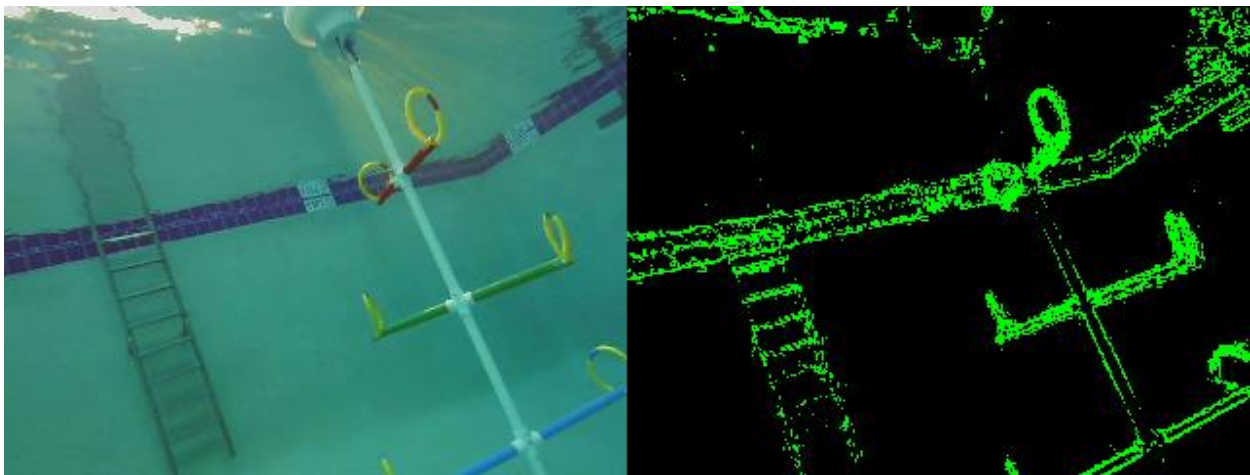


Figure 72: Video transmission, original (left), received (right)

A property of the .PNG file format is that it has a distinct 8-byte header, allowing for the frames to be separated without additional overhead. This approach also easily allows for each frame to be represented in a binary string form and to be compared to the originally transmitted frame. To compute the error rate of the transmission, Levenshtein distance was employed to compare the difference between the original and received data. Levenshtein distance is a metric describing the number of single character edits (substitution, deletion, or insertion) that is needed for two strings to be the same. From this calculation, it can be determined the number of byte errors present in the transmission. Although less desirable than bit error rate, when considering image compression, there is no direct way to distinguish between why an error occurred, with the two main possible sources including noise providing the wrong bit value or a message being missed. As the source of error cannot be separated, the Levenshtein distance provides a metric indicative of the accuracy of transmission while being able to account for both primary error sources simultaneously. Applying this methodology, the computed byte error rate was  $1.55 * 10^{-3}$ . This error is on the same order of magnitude as the LFSR testing, which is what would be expected. Although this error rate is in terms of bytes instead of bits, the most common error in transmission is that of a single bit within a message, so there is a relationship between the two metrics.

## Chapter 7: Optimization

From the characterization and experimental verification, it is shown that the thruster being used as a transducer behaves in the same manner as a purpose-built transmission device. This allows classical link analysis to be applied to the thruster. This analysis will allow for the determination of the limits of the system, further confirming the expected behavior, as well as showing how to maximize the link performance.

### Optimal Transmission Rate

Independent to the specific hardware of the system, the major factor limiting the transmission rate is the bandwidth of the system. This is a major factor in defining the maximum throughput of a channel. To understand this relationship, a single symbol in the time domain will first be considered. This symbol, shown in Figure 73, has period of transmission,  $\tau$  and as such the symbol rate,  $B$ . This relationship between bandwidth and period is shown in Equation 18.

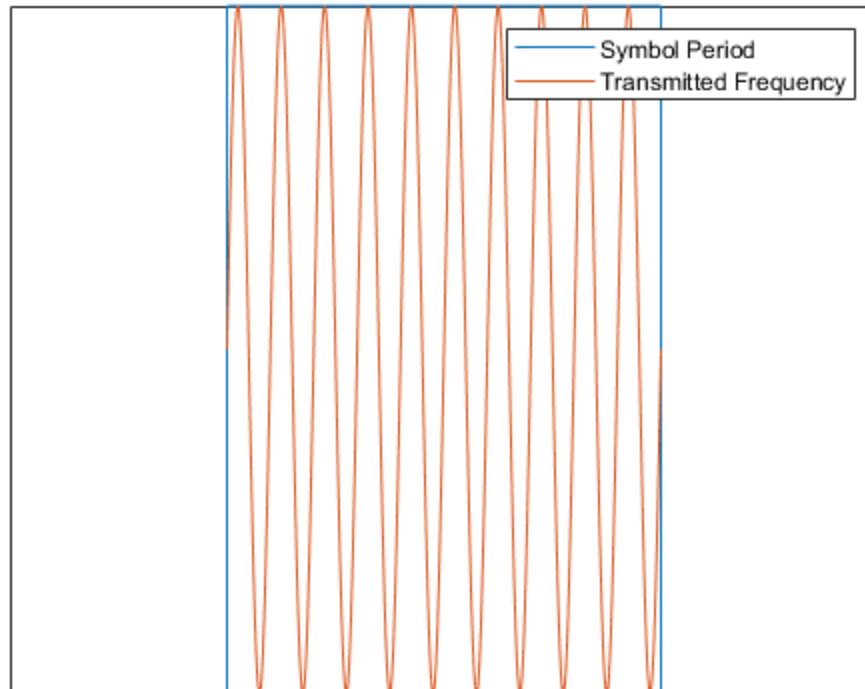


Figure 73: Symbol period visual

Equation 18: Symbol rate and symbol period relationship

$$B = \frac{1}{\tau}$$

Although up until this point, analysis has been primarily around transmissions in the time domain, to understand how they fill the band the frequency domain must be considered. Applying the Fourier transformation to this symbol, would result in a sinc function response about the symbol

frequency. For the purposes of analysis, the power being transmitted is the preferred metric, not the frequency response, which is described as the square of the sinc function. Figure 74 shows the response of a 21 kHz symbol being modulated at 1 kHz transmission rate. As can be seen, the main lobe forms centered around the symbol frequency and the spreading to the first nulls is at +/- 1 symbol rate. This main lobe represents the portion of the bandwidth intentionally allocated to a particular symbol. Beyond the main lobe, side lobes fall off with a width of one symbol rate in both directions of frequency. As the Fourier transform tells us, these side lobes continue off until infinity, however for purposes of an initial analysis of transmission power, the relative power strength of the main lobe compared to this spreading shall be determined.

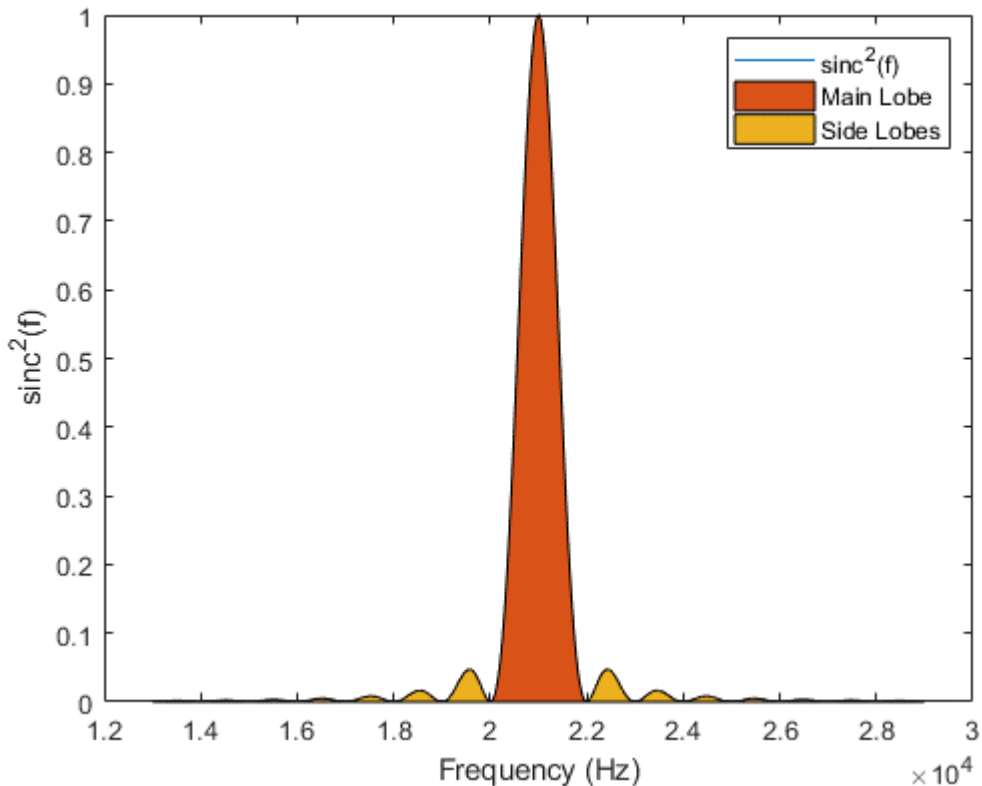


Figure 74: Symbol power response in frequency domain

Looking at the general form of the  $\text{sinc}^2$  function, it must be considered that the power nulls occur at  $\text{sinc}(\pi n)$ , where  $n$  is an integer. From this it can be stated that the area, and as such power, of the main lobe is described by Equation 19.

Equation 19: Main lobe power allocation

$$\int_{-\pi}^{\pi} \text{sinc}^2(t) dt = 2.8363$$

Expanding this integral to describe all transmitted power, is shown in Equation 20.

Equation 20: Full symbol power allocation

$$\int_{-\infty}^{\infty} \text{sinc}^2(t) dt = 3.14159$$

From this, the percentage of transmitted power contained within the main lobe by taking the ratio of these powers can be computed. As shown in Equation 21, approximately 90.3% of the power is contained in the main lobe.

Equation 21: Proportion of power in main lobe

$$\frac{2.8363}{3.14159} = 90.3\%$$

For an initial analysis, it shall be assumed that the main lobe contains all the power and the power outside of that lobe will be ignored. This will serve to compute an upper bound of the transmission rate and will ignore the noise induced from inter symbol interference. Inter symbol interference will be considered later in this section to account for this frequency spreading. With this assumption in mind, the band utilization as a function of number of transmitted symbols and the symbol rate can be calculated, as described by Equation 22.

Equation 22: Symbol bandwidth allocation

$$\text{Maximum Bandwidth}_{\text{symbol}} = 2 * \text{Symbol Rate}$$

Considering the parameters of the communication system used for the experimental testing, a bandwidth of 10 kHz with 5 symbols, bandwidth of the link can be determined. A visualization of this band is shown in Figure 75. Applying Equation 23, the expectation that packing the main lobes without interference would be proportional to the number of symbols is confirmed.

Equation 23: Symbol bandwidth for the experimental link

$$\text{Bandwidth}_{\text{symbol}} = \frac{\text{Channel Bandwidth}}{\# \text{ Symbols}} = \frac{10 \text{ kHz}}{5} = 2 \text{ kHz}$$

As discussed before, the symbol rate is half the bandwidth of a symbol, so in this case would be 1 kSymbol/s. The current transmission protocol uses 4 of the frequencies for data and one for a Null message header. From this the maximum baud rate for the parameters can be determined using Equation 24, or number of bits per second that could be transmitted on the link. Of note here, the overhead of the protocol is not being considered, this is the upper bound and in practice this will be reduced.

Equation 24: Baud rate computation

$$\text{Baud Rate} = \frac{\text{Symbols}}{\text{second}} * \frac{\text{Bits}}{\text{Symbol}} = \frac{1000 \text{ Symbols}}{\text{second}} * \frac{2 \text{ bits}}{\text{symbol}} = 2 \text{ kBits/s}$$

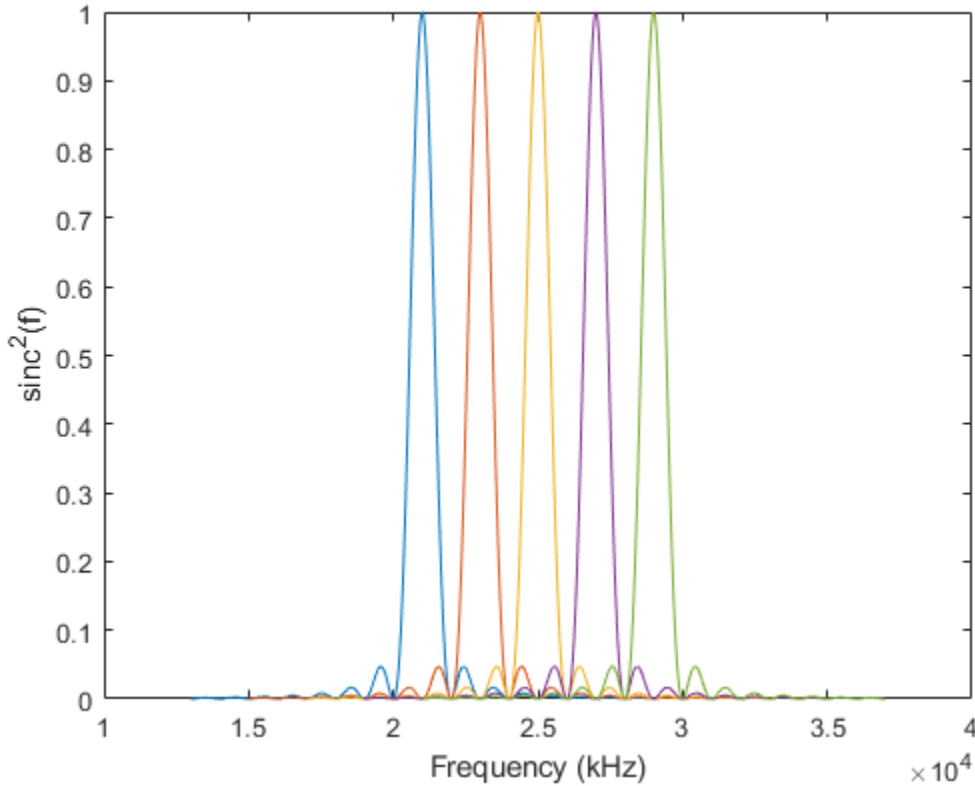


Figure 75: Symbol allocation within a band

When the protocol is considered, the relationship of bits that can be represented and symbol quantity must be adjusted. As the number of bits per symbol can be adjusted, the generalization of this relationship to an arbitrary number of symbols is presented in Equation 25, where N is the number of symbols. Considering Equation 24, the other term that must be described is the symbol rate, shown in Equation 26 where C is the channel bandwidth. Substituting Equation 25 and Equation 26 into Equation 24, the generalized relationship for the baud rate of the system with the given protocol can be determined. Equation 27 shows this relationship.

Equation 25: Protocol impact on symbols

$$\frac{\text{Bits}}{\text{Symbol}} = \log_2(N - 1)$$



Equation 26: Symbol rate relationship to bandwidth

$$\frac{\text{Symbols}}{\text{second}} = \frac{C}{2 * N}$$

Equation 27: Generalized baud rate for the protocol

$$\frac{\text{Bits}}{\text{second}} = \frac{\log_2(N - 1) * C}{2 * N}$$

From this relationship the maximum baud rate achievable baud rate versus number of symbols for a given bandwidth can be plotted. Figure 76 plots this relationship and for clarity Table 5 contains the baud rate at integer multiples of N. As can be seen in the table, the peak baud rate within the range takes place at N = 5, with a non-integer peak at approximately N = 4.6. This conclusion demonstrates that within the given bandwidth and protocol constraints, the use of 5 symbols allowed for the maximum data throughput. This conclusion expands upon what was found in the characterization section for the given protocol, confirming it in the case of symbol quantities that are not values of  $2^n+1$ , where n is the number of bits per symbol.

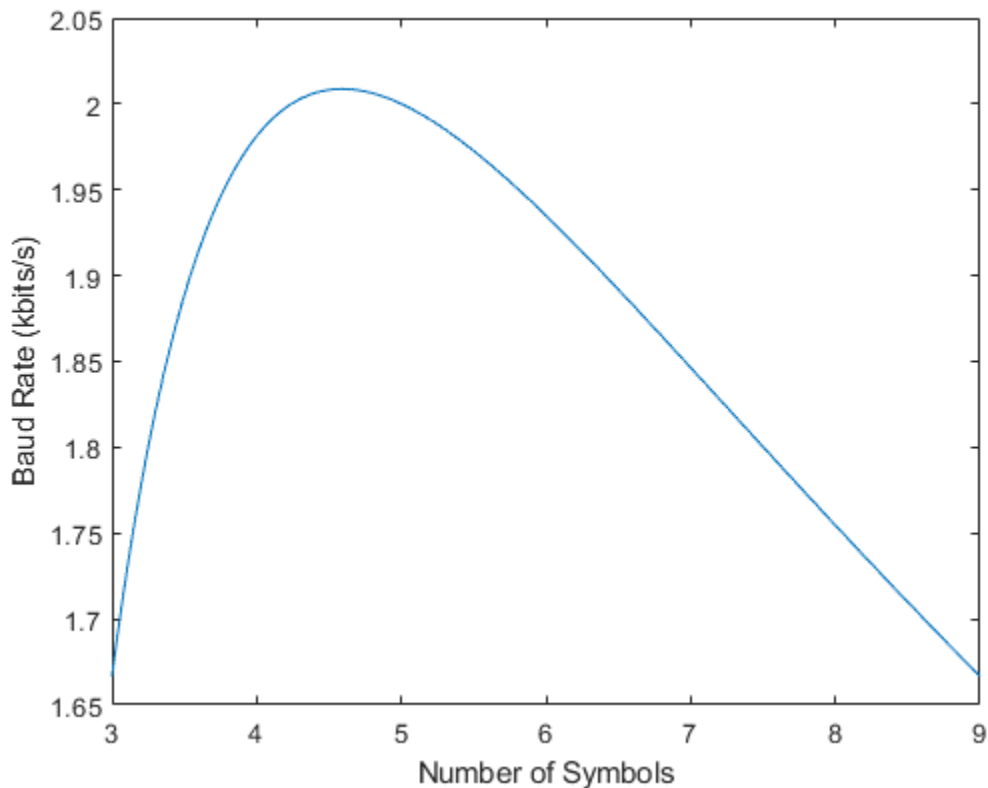


Figure 76: Number of symbols vs. baud rate

Table 5: Baud rate at various symbol numbers

<b>N</b>	<b>Baud Rate (kbit/s)</b>
2	2.5
3	1.67
4	1.98
5	2.0
6	1.93
9	1.67

This analysis does bring up the question of whether the protocol used is the correct choice. Table 5 also includes a value of  $N = 2$ , which would not work with our given protocol. The baud rate for this term was computed using the term  $\log_2(N)$  instead of  $\log_2(N - 1)$  and assumes that a protocol without a Null frequency identifying the start of message is not used. While the initial conclusion may be that the removal of a Null symbol yields a higher baud rate, the implications of decision need to be considered. Instead of the presence of a message being signified by a single symbol, a header must be used, comprised of a more than one symbol. It must be considered if the protocol overhead of creating a unique header is less than the reduction in data rate from using a Null symbol.

To investigate the difference in protocols, a comparison against an established 2-bit transmission protocol, RS232 is presented. This protocol uses a start bit and stop bit between 8 data bits to distinguish the message. However, as in the case of the characterization section, a generalized form of this protocol in which the payload size is adjustable will be considered. It will also be assumed that data is being constantly transmitted, something that in practice RS232 can struggle with, but will allow for peak performance to be evaluated. Applying the same methodology as before, the performance on for a given bandwidth can be characterized, 10 kHz in this case. Figure 77 shows the plotting of these behaviors for the new protocol as well as the two top performers from the current protocol. As can be seen, the use of only two symbols outperforms the five-symbol protocol in all payload sizes above three symbols. The theoretical peak performance difference between these two protocols is 20% more in the case of the two symbols.

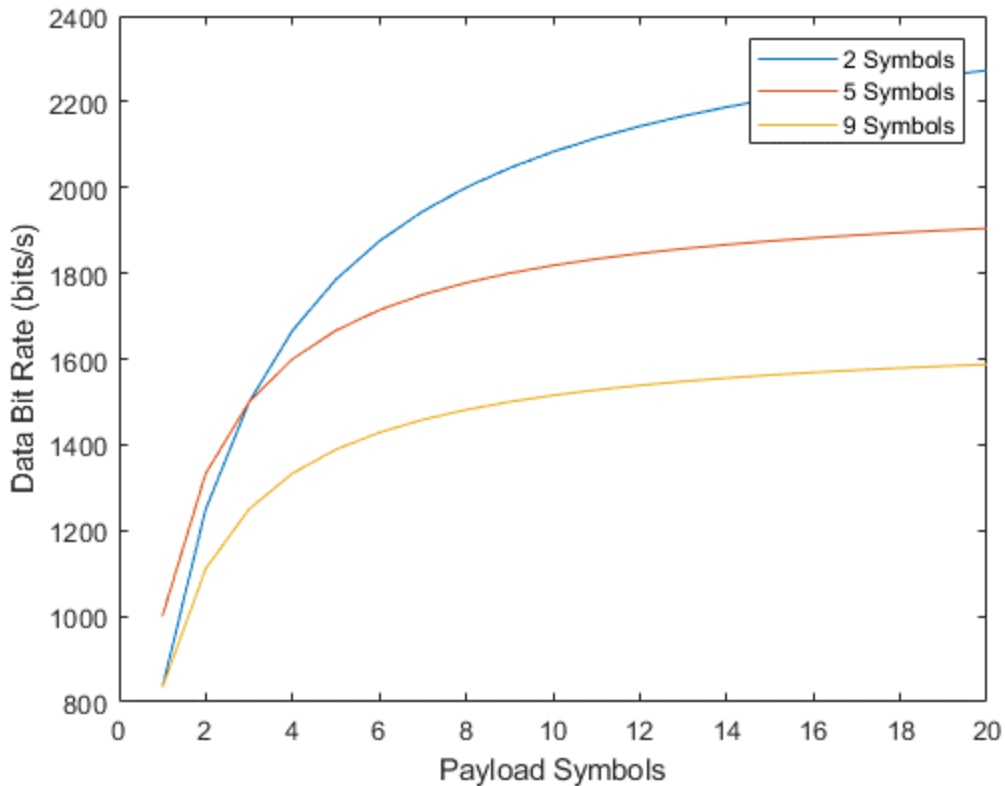


Figure 77: Symbol rate comparison between two protocols

The major takeaway from this protocol comparison is that there is optimization potential in the protocol used. In communication research overall there have been many strides into optimizing the data throughput of a channel, and as such specific optimizations will not be presented. As the thruster behaves as a transducer, this established body of work can be utilized. A consideration to factor into the selection of a protocol is its susceptibility to noise, especially in the target environments for this type of system.

### Inter-Symbol Interference Analysis

Inter-symbol interference refers to the portion of transmitted power that spills over from the other symbols being transmitted. As shown in Figure 75, a portion of each symbols power, approximately 9.7%, is not within the desired portion of the frequency band. This results in reducing the power of the other symbols and an overall decrease in the signal to noise ratio. A higher noise ratio does not necessarily mean that a system has reduced throughput, a tighter packing of symbols can be potentially advantageous when the signal to noise ratio is higher than the target bit error rate. In this case, there are two possible opportunities, to use less of the frequency band or to increase the symbol rate. Each approach has a unique value depending on the situation, and so the impact of increasing symbol overlap shall be considered.

The basis of this this analysis relies on Shannon’s Limit. This relationship, shown in Equation 28, describes the theoretical max transmission rate in bits/s of the channel,  $C$ , in terms of the bandwidth,  $B$ , and the signal to noise ratio,  $S/N$ .

Equation 28: Shannon-Hartley Theorem

$$C = B * \log_2 \left( 1 + \frac{S}{N} \right)$$

Beyond providing the theoretical limit for a channel, this theorem also describes the nature of how a changing signal to noise ratio impacts the channel capacity. Looking back at Figure 75, it can be seen that the other symbols are indeed sharing a portion of the power of the main lobe on each individual symbol. To consider the worst-case symbol, the center lobe of the frequency band is selected. This lobe, colored in yellow in Figure 75, minimizes the distance to all other symbols being the middle of an odd number of symbols, which our current protocol always produces. This should experience the largest impact of side lobes from all other side lobes, and therefore have the lowest signal to noise ratio. Of note, this analysis is just considering the transmission effects, environmental noise at a specific frequency may change this dynamic through effects such as attenuation. Of note, the worst case of signal to noise ratio as this will also define the performance of the link.

For clarity, a more zoomed in version of the side lobe interaction of Figure 75 is shown in Figure 78. The central main lobe, shown in yellow, is impacted by 8 side lobes, two from each other symbol. The orange symbol impacts it with the first and second side lobe, and blue its 3<sup>rd</sup> and 4<sup>th</sup>. As this diagram is symmetric about the central symbol, the symbols shown in purple in green impact it in the same way as the orange and blue, respectively.

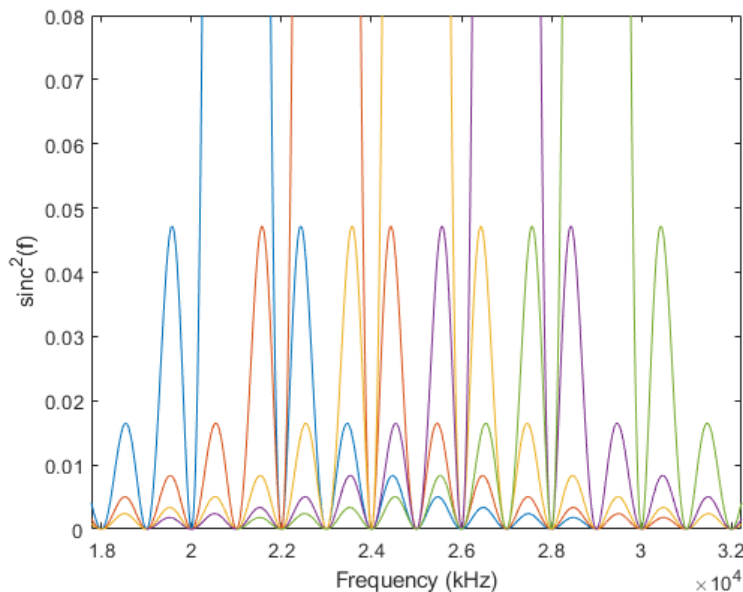


Figure 78: Inter Symbol Interference visualization

Utilizing the area math from prior in the chapter, the area of each of the side lobes impacting the central frequency can be computed. First at the contributions of the orange and blue symbols will be considered, shown in Equation 29 and Equation 30, respectively. From these, it can be determined the total power contribution of the other symbols through the application of symmetry, shown in Equation 31. With this power value determined, the impact that it has can be computed. The signal to noise, shown in Equation 32, is simply the ratio of the main lobe power over the power of all the side lobes. This signal to noise ratio would be the upper limit of what a protocol can achieve, as any other external factors would further reduce this value.

*Equation 29: Adjacent symbol power contribution*

$$A_{red} = \int_{\pi}^{2\pi} \text{sinc}^2(t)dt + \int_{2\pi}^{3\pi} \text{sinc}^2(t)dt = 0.09988$$

*Equation 30: Third and fourth side lobe power contributions*

$$A_{blue} = \int_{3\pi}^{4\pi} \text{sinc}^2(t)dt + \int_{4\pi}^{5\pi} \text{sinc}^2(t)dt = 0.020995$$

*Equation 31: Power of other symbol side lobes*

$$A_{interference} = 2 * (A_{red} + A_{blue}) = 0.24175$$

*Equation 32: Inter-symbol interference signal to noise ratio*

$$SNR = \frac{\text{Main Lobe Power}}{\text{Interfering Power}} = \frac{2.8363}{0.24175} = 11.732$$

Although the use of more symbols was deemed to be less efficient, it can be useful to visualize this math extended to a larger number of symbols. This can be used to determine the relationship between number of symbols and the SNR. Shown below in Figure 79, it can be seen that the SNR decreases with the number of symbols. However, as the number of symbols increases the additive impact of each additional symbol is decreased.

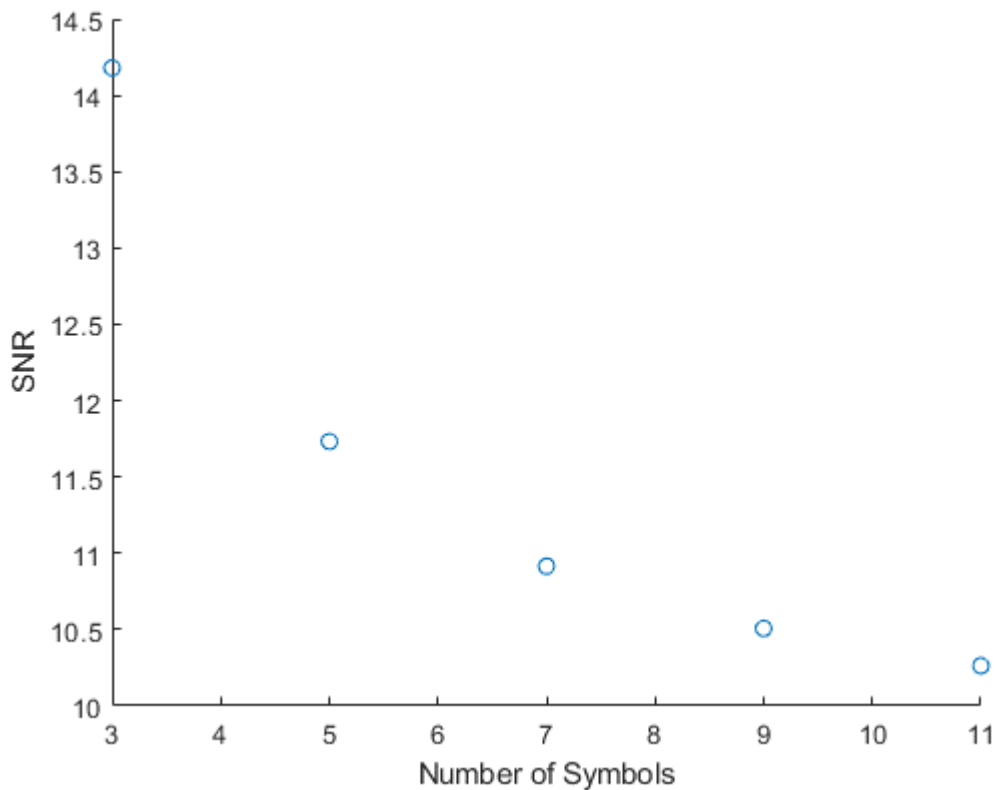


Figure 79: SNR at various symbol numbers

Considering Shannon's limit, this SNR relationship seems to disagree with the data rates computed. At the SNR value of 11.732 and the bandwidth of 10 kHz used in the example, the theoretical maximum performance is just over 36.7 kBit/s, significantly higher than the 2 kBits/s maximum rate calculated for the protocol. This is not a rebuke of Shannon's Limit, rather proof that the protocol can have a large impact on the data rate. This is not the only factor impacting this large difference in real world data rates. Physically, a limit of the technology is that only one frequency can be transmitted at one time, limiting the bandwidth utilization. However, this SNR analysis is not without use. From this SNR computation, a relationship to the expected BER of the link can be leveraged, a key metric communication links. For FSK, the relationship between the SNR and BER is shown in Equation 33, where M is the number of bits per symbol. Of note here, by accounting for the impact of the symbols on each other,  $E_b/N_o$  has been computed, or a normalized signal to noise ratio.

Equation 33: BER for M-FSK communication (Proakis & Salehi, 2007).

$$BER_{M-FSK} = \frac{1}{2} * erfc\left(\sqrt{\frac{E_b}{N_o}}\right) = \frac{1}{2} * erfc\left(\sqrt{\frac{SNR}{M}}\right)$$

Evaluating the equation with the computed SNR values, the relationship between number of symbols and BER can be seen in Figure 80. This plot illustrates the nature of the tradeoff between symbol packing and communication stability as well as provides a minimum theoretical BER that should be seen in testing,  $6.36 \times 10^{-7}$  in the case of five symbols. In practice error rate is much higher than this, on the order of  $10^{-3}$ , however this is accounting for all sources of noise rather than just the effects of transmitting the symbols. When analyzing these results, the goal of the system must be considered. The use of five symbols over three results up to 16.5% more data per second, however it comes at the cost of a BER increase of 11.6%. Depending on application, either option could be the right choice to meet target goals. At this juncture, optimality cannot be judged without additional criteria being provided.

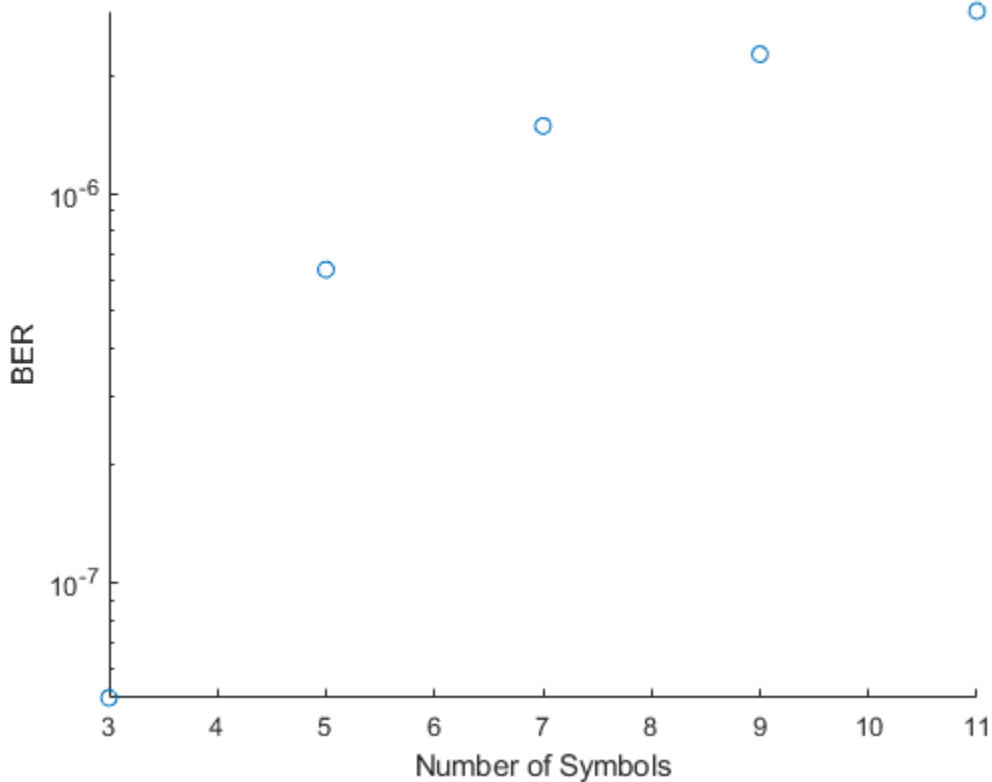


Figure 80: BER as a function of number of symbols

### Harmonic Optimizations

Another potential area of link optimization stems from the nature of power delivery to the thruster. Current is driven to the thruster in square waves. As power delivery relates to the underlying signals being transmitted, the signal behaviors can be passed along. Square waves inherently have odd harmonics, or frequency responses at multiples of a given value, albeit with a reduction in power. Figure 81 visualizes the frequency response of a given square wave. As can be seen, harmonics propagate out to infinity with a reduction in power. This effect allows for is

potential optimization in two different ways. The first approach would be in improvement of SNR, by performing demodulation on the harmonics of the transmitted frequency as well as the expected symbol frequency to improve decoding accuracy. The other main approach to be estimated is to leverage these harmonics instead as the primary transmission source, as the multiplicative nature of harmonics allow for baud rates to be multiplicative as well. Both approaches will be investigated.

## 1 Hz square wave

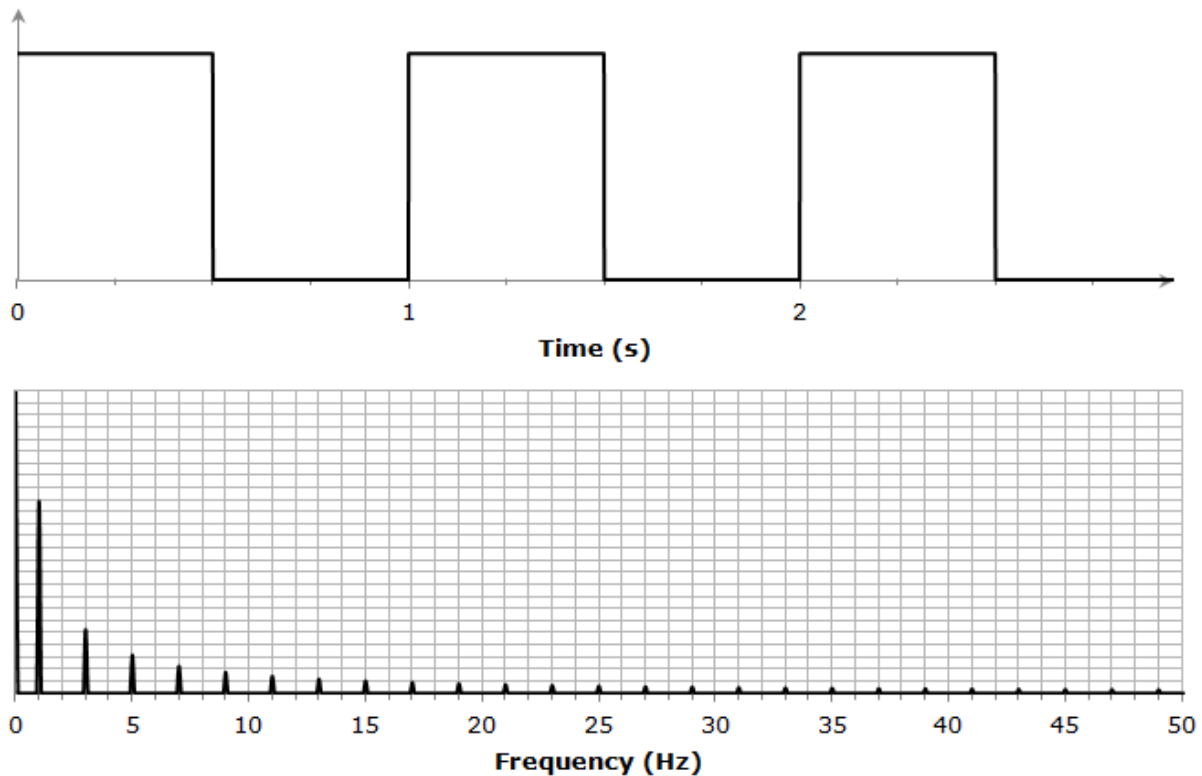


Figure 81: Spectrum response of harmonics (*The Pulsar, 2015*).

### Harmonic Combination

The basis of this investigation lies in the principle that harmonics are transmitting the same data, and as such can contribute to the signal portion of SNR by evaluating that frequency as well. In terms of leveraging this effect, the implications of a corresponding noise increase must be considered as to whether it will result in an overall higher SNR for the transmitted data. For purposes of this evaluation, it must be considered what the primary source of noise is. This varies given the operational environment dramatically, but for the targets of this technology, that being smaller vehicles operating in shallow water, the primary sources of noise come from environmental noise, specifically multipath and internal band effects of lobes interfering with each other. What this allows for is the evaluation of noise to be contained within the signals itself,



as opposed to having to account for external factors such as the typical ocean noise floor that exists for lower frequencies.

Among these possible sources of noise, a reduction in multipath noise can be eliminated as something that would benefit from the use of a harmonic. Reflections occur across the entirety of the frequency domain and are impact in the same manner, meaning it would contribute proportionally to signal and noise. The other two sources of noise, however, have more potential benefit. Considering the frequency response falloff, this directly correlates to a power reduction at each harmonic. For reference, the third harmonic provides has a power of  $1/6^{\text{th}}$  the first. While this may seem low, it is a non-trivial amount of power. In terms of inter-symbol interference, these representations of the symbols will be lessened as they are inherently spaced. This means that the impact of adding them is beneficial, and not simply contributing equally to the ratio of signal and noise strength. When considering environmental factors, the addition of a harmonics worth of power can increase the relative strength of a symbol to the noise floor. A consideration here that must be noted however is that the noise floor may also have noise at the harmonic frequencies, although typically there less at higher frequencies. The issue it does introduce is that it can make the analysis of a potential benefit from this highly variable across different operating cases, and as such is something to be considered but not relied upon.

#### Harmonic Transmission

Leveraging the property of harmonics, the additional bandwidth allotted by using the wider spectrum can be considered. It must be noted that the nature of harmonics does yield a reduction of power. For the third harmonic, the first harmonic present, there is a reduction in power of  $1/6^{\text{th}}$  the original frequency. As such, for purposes of this analysis it shall be considered that this will be used in the correct situation, where the SNR required for the purpose is lower, or the baud rate matters dramatically more than the BER. As shown in Figure 82, the third harmonic of the band has 3 times the bandwidth available, potentially a massive throughput improvement. From this, experimentation with a symbol rate three times higher can be conducted. This was demonstrated with an image and video transmission example, where the limit of transmission at 1 kSymbol/s or 2 kBits/s was increased to 6kBits/s, making the transmission of that data type more feasible.

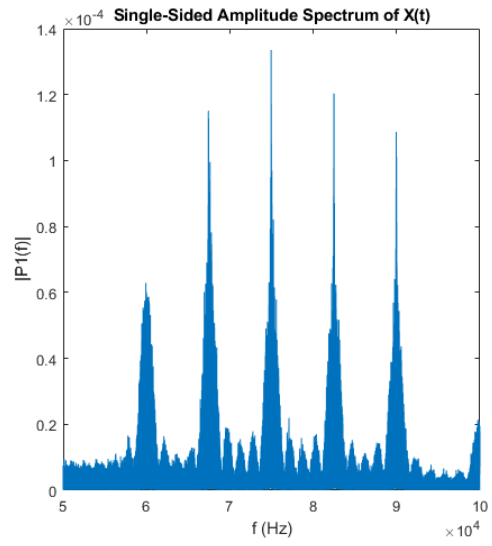
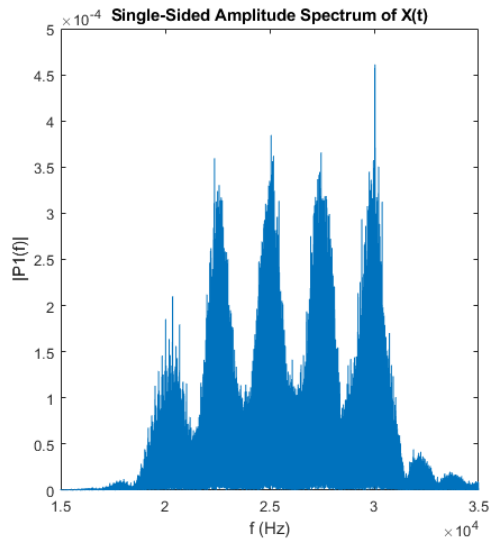


Figure 82: First Harmonic (Left), Third Harmonic (Right)

## Chapter 8: Conclusions

The overarching purpose behind this work was the design and development of a novel means of transmitting data underwater. This was accomplished leveraging the ambient acoustic noise produced by the pulse width modulation (PWM) switching noise on brushless electric thrusters. By modulating this noise, information can be transmitted. A prototype for system for wireless transmission was constructed and validated. From this implementation, core research questions could be proposed and answered. The primary among them being, how does the operation of the thruster as a propulsor effect the ability to transmit data? If this behavior could be understood, the technology could be validated, analyzed, and optimized.

To complete this work, the process took place in multiple steps to ensure success and allow for corrections as the understanding of the technology evolved over time and testing. A review of the relevant literature familiarized the author with the current state of the art in acoustic modem technology and testing, as well as the directions the technology is growing in. Taking cues from this, an initial system was prototyped and evaluated, both providing validation of the new technology as well as yielding insights into its behavior. From this prototype, a system characterization could be conducted and predictions about the behavior of the system could be validated. With the system understood, optimization leveraging the unique characteristics of the hardware could be explored.

### Research Outcomes

The research question driving this work was the determination of how the operation of a thruster as a propulsor would impact the transmission of data. Through characterization of the thruster and experimental testing to validate the findings, it was shown that there are minimal differences between the thruster and a discrete acoustic transmitter. The primary limitation found from the thruster was in the frequency range presented, in which the ESC limited the upper bound of the data transmission.

More specifically, the results of this characterization showed a flat frequency response for the thruster, an ideal characteristic as it allows for flexibility in the selection of an operating band. Furthermore, it found the theoretical limit of performance for the system at 3230 symbols/s. In experimentation, a transmission rate of 3000 symbols/s was demonstrated. The thruster was shown capable of transmitting image and video data representative of the target use case with performance levels on par with existing systems. A demonstrated data rate of 2000 bit/s and 6000 bit/s outperform existing commercial systems. Finally, although it was not able to be tested at much longer ranges, this technology showed no inherent limitation to transmitting further ranges, a promising result to ensure the technology is useful in implementation.

From this characterization, it was possible to analyze the link using established methodology. This served to identify areas of potential performance improvement, namely the protocol selection.

In practice, selection of a protocol should be taken on an application specific basis, as the correct option will change based on additional requirements, including the need for error correction or detection. With those requirements established, the selection of protocol parameters such as the number of bits per symbol can be determined. Although a specific conclusion of optimality was not presented, the methodology shown will allow proper analysis to be conducted for all implementations of the transmitter.

Regarding link optimization, leveraging harmonics proved to be a promising technology in the right circumstances, where transmissions would still have an acceptable SNR with the reduction in power experienced. Although not always useful, having this capability on an implemented communication system would provide meaningful value to the operation of the link.

Beyond the technical aspects of the link, this work demonstrated that this technology could be successfully implemented on commercial off the shelf (COTS) hardware, with only firmware changes required to be able to transmit information. This demonstrates that small or low-cost systems that could benefit from a wireless link can feasibly integrate or be designed with this capability. In the bigger picture, this has the potential to enable more capable operations in this class of vehicles, especially in environments where operations with high-cost systems were not desirable due to the risk.

### Future Work

The main area of extending this work would be in the implementation of this technology into an operational system. Although this work demonstrates applications such as the transmission of video through a thruster, an actual operational robot using this technology provides a more conclusive result as well as a case study to compare future work to. Beyond this, there are multiple possible extensions to this technology that can come through applying the technology to systems that have multiple discrete thrusters. Communication technologies like MIMO can be used to increase the bandwidth capabilities of a system with multiple transmission sources. An example system for this work would be a BlueRobotics Bluerov, a relatively low cost and small system that can have 6-8 thrusters in its control system. Multiple modems would also allow for the creation of systems capable of routing multiple vehicles transmissions simultaneously on multiple frequency bands. Beyond systems that have no modem already, systems that already employ their own can add an additional layer of reliability or bandwidth to their operations.

Furthering the work directly conducted in this research, more validation of the technology should be conducted. Testing a thruster throughout its entirety of speed ranges requires test equipment that must be purposely designed for the case, as the motor must be ideally held statically and away from the surface or solid that would produce boundary layer effects on the flow. While these effects may be minimal, they hamper equal comparisons and as such should be eliminated if possible. The other major test that should be considered is long term endurance testing on a motor to determine if using it as a transmitter has any impact on the longevity of the hardware.

There is no evidence that this will be the case, as it is a brushless system, however validation of this would yield useful information to those intending to use this solution in any long-term application.

This work also raises questions about the design of systems using this technology or variants of this work. An investigation of this technology integrated into systems may yield insights into how the design or placement of thrusters impacts the performance of the data link. The opposite application of this technology may also be considered, where the ability to control the frequency of a thruster is used to spread the spectral response, aiding in stealth operations. This would also warrant an investigation on thruster placement to yield the best results.

## References

- Allen, J. B., & Berkley, D. A. (1979). Image method for efficiently simulating small-room acoustics. *The Journal of the Acoustical Society of America*, 943-950.
- Basett, C., Thomson, J., & Polagye, B. (2010). Characteristics of Underwater Ambient Noise at a Proposed Tidal Energy Site in Puget Sound. *OCEANS 2010*. Seattle: IEEE.
- Basic ESC. (2021). Retrieved from Blue Robotics: <https://bluerobotics.com/store/thrusters/speed-controllers/besc30-r3/>
- Binojkumar, A. C., Saritha, B., & Narayann, G. (2015). Acoustic Noise Characterization of Space-Vector Modulated Induction Motor Drives - An Experimental Approach. *IEEE Transactions on Industrial Electronics*, 3362-3371.
- Bracewell, R. N. (1986). *The Fourier transform and its applications*. New York: McGraw-Hill.
- Butka, B., Cronin, S., & Romney, J. (2018). Using an Electric Thruster as an Acoustic Transducer. *IFAC* (pp. 372-377). Optija: Elsevier.
- Chitre, M., Shahabudeen, S., & Stojanovic, M. (2008). Underwater Acoustic Communications and Networking: Recent Advances and Future Challenges. *Marine Technology Society Journal*, 103-116.
- Clay, C. S., & Medwin, H. (1977). *Acoustical Oceanography*. Wiley.
- Costanzi, R., Monni, N., Ridolfi, A., Allotta, B., & Caiti, A. (2017). On field experience on underwater acoustic localization through USBL modems. *OCEANS 2017*.
- Cronin, S., & Romney, J. (2021). *Motor Comms VESC*. Retrieved from Github: <https://github.com/jeffromney/motor-comms-vesc>
- Flipsky. (2021). *FSESC 4.12 50A Based on VESC 4.12*. Retrieved from Flipsky: <https://flipsky.net/products/torque-esc-vesc-%C2%AE-bldc-electronic-speed-controller>
- Galvin, R., & Coates, R. (1995). Analysis of the Performance of an Underwater Acoustic Communications System and Comparison with a Stochastic Model.
- Gamazo-Real, J., Vázquez-Sánchez, E., & Gómez-Gil, J. (2010). Position and Speed Control of Brushless DC Motors Using Sensorless Techniques and Application Trends. *Sensors*, 6901-6947.
- Gebbie, J., Siderius, M., & Allen, J. (2015). *A Two-hydrophone Range and Bearing Localization with Performance Analysis*. Portland State University.
- GitHub. (2021). *VESC Firmware*. Retrieved from GitHub: <https://github.com/vedderb/bldc>
- Google. (2021). *Google Maps*. Retrieved from Google: [maps.google.com](https://maps.google.com)
- Grandmetric. (2021). *Multipath*. Retrieved from Grandmetric: <https://www.grandmetric.com/topic/10-multipath/>
- Healy, C., Jebur, B., Tsimenidis, C., Neasham, J., & Chambers, J. (2019). Full-Duplex Channel Analysis for Underwater Acoustic Communications. *Underwater Acoustics Conference and Exhibition*, (pp. 251-258). Herskelion.
- Holtz, J. (2002). Sensorless Control of Induction Motor Drives. *Proceedings of the IEEE*, 1359-1394.
- HyperPhysics. (2021). *Inverse Squared Law, General*. Retrieved from HyperPhysics: <http://hyperphysics.phy-astr.gsu.edu/hbase/Forces/isq.html>
- Jung, L., & Abdullah, A. (2010). Underwater Acoustic Communications: Relationship Between Data Packet Size, Throughput, BER, and Distance. *Global Conference on Power Control and Optimization*. Kuching.

- Kaur, J., Kaur, H., & Sandhu, M. (2016). Comparison of BER for Various Digital Modulation Schemes in OFDM System. *Advanced Research in Electronics and Communication Engineering*, 835-842.
- Knowledge Amplifier. (2021). *What Is Modulation ? Why modulation is required? Types Of modulation*. Retrieved from Knowledge Amplifier: <https://lazyengineer123.blogspot.com/2021/03/what-is-modulation-why-modulation-is.html>
- Mackenzie, K. V. (1981). Discussion of sea water sound-speed determinations. *The Journal of the Acoustical Society of America*, 801-806.
- MotionControlGuide. (2021). *Brush vs Brushless DC Motors*. Retrieved from MotionControlGuide: <http://www.motioncontrolguide.com/learn/tech-tips/motors/subcategory/dc-motors/brush-vs-brushless-dc-motors/>
- Naderi, Y. M., Rabiee, H. R., Khansari, M., & Salehi, M. (2012). Error control for multimedia communications in wireless sensor networks: A comparative performance analysis. *Ad Hoc Networks*, 1028-1042.
- National Instruments. (2021). *NI 9222 Datasheet*. Retrieved from National Instruments: [https://www.ni.com/pdf/manuals/374210a\\_02.pdf](https://www.ni.com/pdf/manuals/374210a_02.pdf)
- Neasham, J., & Sharpouse, R. (2015). Development of the "Seatrac" miniature acoustic modem and USBL positioning units for subsea robotics and diver applications. *OCEANS*. Genova: IEEE.
- Paull, L., Saeedi, S., Seto, M., & Li, H. (2014). AUV Navigation and Localization: A Review. *IEEE Journal of Oceanic Engineering*, 131-149.
- Proakis, J., & Salehi, M. (2007). *Digital Communications*. McGraw-Hill Education.
- Sendra, S., Lloret, J., Jimenez, J., & Parra, L. (2016). Underwater Acoustics Modems. *IEEE Sensors Journal*, 4063-4071.
- Shahabudeen, M., & Stojanovic, M. (2008). Underwater Acoustic Communications and Networking: Recent Advances and Future Challenges. *Narine Technology Society Journal*, 103-116.
- Sharif, B., Neasham, J., Hinton, O., & Adams, A. (2000). A Computationally Efficient Doppler Compensation System for Underwater Acoustic Communications. *Journal of Oceanic Engineering*, 52-61.
- Shen, L., Henson, B., & Mitchell, P. (2019). Robust Digital Self-Interference Cancellation for Full-Duplex UWA Systems: Lake Experiments. *Underwater Acoustic Conference and Exhibition*, (pp. 243-250). Herskelion.
- SPARTON. (2021). *PHOD-1 Hydrophone*. Retrieved from SPARTON: <https://www.spartonnavex.com/product/phod-1-hydrophone/>
- Stojanovic, M., & Preisig, J. (2009). Underwater Acoustic Communication Channels: Propagation Models and Statistical Characterization. *IEEE Communications Magazine*, 84-89.
- Stokes, G. G. (1845). On the theories of the internal friction in fluids in motion, and the equilibrium and motion of elastic solids. *Transactions of the Cambridge Philosophical Society*, 287-342.
- T200 Thruster. (2021). Retrieved from Blue Robotics: <https://bluerobotics.com/store/thrusters/t100-t200-thrusters/t200-thruster-r2-rp/>
- Tariq, M., Shafie Abd Latiff, M., & Ayaz, M. (2017). Beacon-based routing protocols for underwater acoustic sensor networks. *Int J Commun Syst.*, 10.
- Techy, L., Morgansen, K., & Woolsey, C. (2011). Long-Baseline Acoustic Localization of the Seaglider Underwater Glider. *American Control Conference*, (pp. 3990-3995). San Francisco.
- Teledyne Marine. (2021). *RESON TC4013 - hydrophone*. Retrieved from Teledyne Marine: <http://www.teledynemarine.com/reson-tc4013>

- Teledyne Marine. (2021). *TC1026*. Retrieved from Teledyne Marine:  
<http://www.teledynemarine.com/Lists/Downloads/RESON/Transducers/TC1026%20Product%20Leaflet.pdf>
- The Pulsar. (2015). *Generating Sine Waves from Square Waves*. Retrieved from The Pulsar:  
<http://www.thepulsar.be/article/generating-sine-wave-from-square-waves/>
- Underwater Acoustics*. (2020, December 2). Retrieved from Wikipedia:  
[https://en.wikipedia.org/wiki/Underwater\\_acoustics](https://en.wikipedia.org/wiki/Underwater_acoustics)
- Zhao, A., Ma, L., Hui, J., Zeng, C., & Bi, X. (2018). Open-Lake Experimental Investigation of Azimuth Angle Estimation Using a Single Acoustic Vector Sensor. *Journal of Sensors*.



## Appendix

### Experimental Testing Results

Table 6: 16-bit LFSR Testing Results

Range (m)	Duty Cycle	Baud	BER
10	65	1000	0.003361
10	65	1000	0.002977
10	35	1000	0.001227
10	35	1000	0.00194
10	40	1000	0.003321
10	40	1000	0.002642
10	60	1000	0.004786
10	60	1000	0.004898
10	50	1000	0.005385
10	50	1000	0.004065